Abstract

The ever-increasing demand for telecommunications is calling for higher transmission speeds and enhanced encryption techniques, including chaos secure communication. In contrast to the rising number of studies of chaos synchronization on different platforms, there is a lack of experimentally synchronizing modulation instability combs in microring resonators.

The chaotic behavior inside the resonators is studied by utilizing the Lugiato-Lefever equations to simulate the optical fields. Additionally, the synchronization of two cascaded microring resonator is analyzed by varying parameters such as the injection factor between the rings or introducing noise during transmission. To experimentally validate the simulation results, two microring-resonators fabricated on the same chip were used to lessen potential fabrication errors.

The simulation revealed not only a dependence of the degree of synchronization on multiple parameters but also a high robustness against noise in the transmission channel. In contrast to the simulation, the experimental results demonstrate the difficulty to synchronize chaotic microring-resonators as the correlation between both resonators remains low. A formula was introduced that revealed that synchronization between the resonators could not be achieved experimentally. This formula can serve future researchers as a lower bound indicator to measure whether a synchronization of two chaotic signals could have been achieved.

In summary, while chaos synchronization remains a challenge experimentally, this work offers valuable insights into the synchronization of microring resonators and paves the way for further advances in this line of research.

要旨

電気通信の需要が高まっている今日においては、通信速度の向上やカオスセキュア通信を含む暗号技術の発展がますます求められる。 しかし、マイクロチップレーザーや電子回路など、さまざまなプラットフォームを使ってカオスを同期させる研究成果が増加しているのとは対照的に、マイクロ共振器にある変調不安定光周波数コムを実験的に同期させる研究成果はほとんどないのが現状である。

ここではLugiato-Lefever方程式を利用した光場のシミュレーションを行うことで、共振器内部にあるカオスのふるまいを分析する。 また、2つのマイクロ共振器をカスケード接続することによって、通信ノイズや伝送係数のパラメーターがカオスの同期にどの程度影響を及ぼすのか解析する。 シミュレーション結果を実験的に検証するため、1つのチップの上に複数製造したマイクロ共振器を使うことで、製造過程のばらつきによる影響を減らすことを試みた。

結果として、シミュレーションでは混入した伝送路上のノイズが強い場合においても、カオスの同期ができることが明らかとなった。また、伝送係数などのパラメーターを変更することによってカオスの同期の程度が変わることが分かった。 その一方、実験では2つの共振器の相関係数が弱かったため、マイクロ共振器の同期が困難であることが示された。 しかしこれにより、マイクロ共振器の同期が実験的には達成できなかったことを示す公式が得られた。 この公式は、将来的に、マイクロ共振器の相関係数を測るうえで、カオスの同期が達成できたかどうかを示す下限指標となるだろう。

この研究を通して、マイクロ共振器におけるカオスの同期に関する貴重な知識を提供する。

List of Abbreviations

AC	Alternating Current
AOM	Acousto-Optic Modulator
ASE	Amplified Spontaneous Emission
BPF	Bandpass Filter
c.c.	Complex Conjugate
CMA	Chaos Masking
CMO	Chaos Modulation
CSK	Chaos Shift Keying
DC	Direct Current
DFB	Distributed Feedback
EDFA	Erbium-doped Fiber Amplifier
EO	Electro-Optical
ESA	Electrical Spectrum Analyzer
FBG	Fiber Bragg-grating
FSR	Free-Spectral Range
FWM	Four-Wave Mixing
IR	Infrared
LHS	Left-Hand Side
LiDAR	Light Detection and Ranging
LLE	Lugiato-Lefever Equation
LOS	Linear Optical Sampling
MI	Modulation Instability
Microcomb	Microresonator Optical Frequency Comb

MIXSEL	Mode-Locked Integrated External-Cavity Surface-Emitting Laser
MLL	Mode-Locked Laser
NA	Network Analyzer
OFC	Optical Frequency Comb
OSA	Optical Spectrum Analyzer
OSC	Oscilloscope
PC	Polarization Controller
PD	Photodiode
PIC	Photonic Integrated Circuit
PM	Polarization Maintaining
PMD	Phase Modulator
PWR	Power Meter
Q	Quality Factor
QCL	Quantum Cascade Laser
RF	Radio Frequency
RHS	Right-Hand Side
RSA	Rivest–Shamir–Adleman
SNR	Signal-to-Noise-Ratio
SPM	Self-Phase Modulation
TG	Tracking Generator
TSL	Tunable Semiconductor Laser
VOA	Variable Optical Attenuator
WDM	Wavelength Division Multiplexing
WGM	Whispering-Gallery Mode
XPM	Cross-Phase Modulation

Contents

1 Motivation

Demands on telecommunications are increasing. Alongside an increasing amount of users and devices using the internet arises a demand for higher transmission speeds. This requires a higher transmission bandwidth. In order to comply with this demand different techniques are used, but high energy costs and large footprints motivate a search for new approaches. It was found that optical frequency combs (OFCs) could also be used for large broadband high-speed transmission. OFCs are light sources which emit light waves at wavelengths which are equidistant to each other, enabling a cost-effective method to multiplex a signal and increase the effective transmission bandwidth. While they reduce the energy consumption they still have a large footprint and a small repetition rate. In 2007, generation of an optical frequency comb in a microresonator was demonstrated. These so-called microcombs enable wavelength division multiplexing on the integrated photonics chip. Because of their small size they are able to generate chaotic waveforms.

Chaos-Secure Communication

One of the comb stages of the optical frequency is called a modulation instability (MI) comb. This MI comb emits a chaotic signal. The chaotic nature of this signal makes it quasi-random and therefore suitable for applications that require randomly generated numbers. The quasi-randomness of chaotic signals makes them particularly interesting for secure communications in cryptography. While there is a rising amount of research on the usage of synchronized chaotic sources to encrypt and decrypt data, there is a lack of reports about experimentally synchronized MI combs in microresonators. Realizing synchronization would allow high-speed transmission with encryption and secure communications. This thesis provides valuable contributions to this goal. First, synchronization of microresonators has been simulated. Furthermore, the chaotic behavior has been analyzed. Lastly, experiments have been conducted that try to prove the simulation results.

2 Theory

To introduce the main ideas, concepts and contents of this thesis, this chapter provides the theory and serves as a review of recent development. First, optical frequency combs (OFC) in their generality are introduced. Then, the view is focused on microresonator optical frequency combs (microcombs), and how OFCs are generated in microresonators. Since one of the microcombs states exhibits chaotic behavior, an understanding of chaos is brought. Finally, chaos synchronization and its applications in secure communication are reviewed.

2.1 Optical Frequency Combs

A little over two decades ago, optical frequency combs (OFCs) were invented. Their orignal purpose was to count the cycles from optical atomic clocks, but as research progressed their applicability was increased.

With the begin of the 21st century, two groups independently demonstrated the actualization of OFCs. In 1999, Hänsch et al used a mode locked laser (MLL) as an OFC to conduct optical frequency measurements [1]. In the same year, the group around Hall measured an OFC, too [2]. This and their life-long contribution in the field of optical metrology resulted in them both receiving the nobel prize in physics in 2005 [3, 4].

The generation of OFCs is traditionally done by stabilizing the phase of an MLL as it was realized that MLLs are applicable in optical metrology [5]. The light pulses from MLLs are a coherent addition numerous longitudinal optical cavity modes, which lead to them being advantageous for two key reasons:

1. The optical modes are evenly spaced in frequency, thus harmonically related.

2. All optical modes share a common phase evolution, meaning they are phase-coherent.

Knowing only one mode by its absolute frequency allows to determine the absolute frequency of any other mode. This deterministic behavior is described by a carrier frequency $\nu_\mathrm{c} = \omega_\mathrm{c}/(2\pi)$ which is modulated by a periodic pulse envelope, $A(t)$. Because of the periodicity of the pulses, describing the light as a periodic Fourier series of the optical modes, $\nu_\mathrm{N} = \omega_\mathrm{N}/(2\pi)$, with Fourier amplitude, A_N, and mode number, N, is also possible.

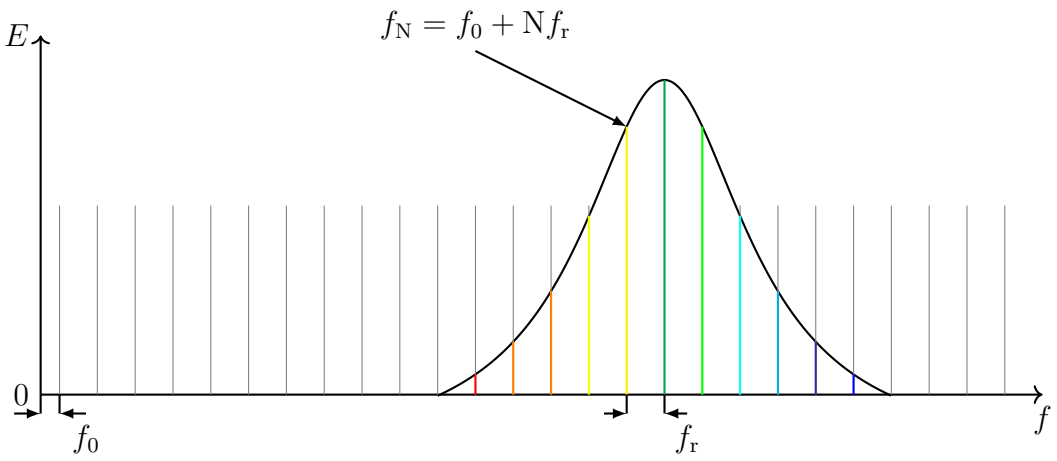

Figure 2.1: Spectrum of an Optical Frequency Comb

$$E(t) = A(t)e^{i\omega_c t} = \sum_{N=N_i}^{N_f} A_N e^{i\omega_N t} \tag{2.1}$$

But as the carrier frequency does not have to be a multiple of the mode spacing, f_r, the individual Fourier frequencies are shifted. They are shifted by an offset, $f_0 \leq f_r$, from a multiple of f_r, resulting in the so called comb equation:

$$f_N = f_0 + Nf_r \tag{2.2}$$

The comb equation 2.2 states that even though numerous optical modes are present in an OFC, they are all determined by just two degrees of freedom, which are the repetition rate, f_r, and the offset frequency, f_0. The repetition rate (f_r) is the inverse of the time period between two pulses, T_r. As pulses are emitted from the cavity once per round trip the pulse repetition period equals to $T_r = 2L/v_g$. Where v_g is the group velocity of the light inside the cavity and L the cavity length. By changing the cavity length, the pulse-repetition rate, T_r, is adjusted. The offset frequency (f_0) is the difference between the carrier wave and the envelope of the pulse. It also represents the harmonic and coherent connection between laser modes as every longitudinal laser mode shares a common phase. With other words, the offset frequency is a measure of coherence. Therefore, it is also related to the derivative of the optical carrier phase relative to the pulse envelope, $\phi_{CEO}(t)$.

$$f_0 = \frac{1}{2\pi}\frac{d\phi_{CEO}}{dt} \tag{2.3}$$

It is important to note, that in order to obtain precise results in optical metrology or spectrology, both parameters have to be determined. Without knowing the offset

frequency, the measured frequency is only determined with a precision of $\pm f_{\mathrm{r}}$.

Applications of the OFC go already beyond the originally intended utility of improving atomic clocks. Utilizing fiber networks, atomic clocks can be compared with high precision [6] and shows the advantages of OFCs. Employing OFCs over fiber networks also enabled to remotely control lab-equipment with a facility-wide timing better than 30 fs [7]. Besides timing, synchronization and comparison applications, simply using them as an oscillator is also feasible. Especially when using an OFC to divide the optical frequency to the microwave regime showed the ability to generate them with low-noise [8]. Moreover, OFCs are used to improve the frequency calibration of astronomical spectrographs and are currently in multiple telescopes around the world employed [9, 10]. These spectrographs measure Doppler shifts of steller spectra to determine the composition of solar atmospheres and radial velocities of celestial bodies. Using OFCs as so called "astrocombs" enables improvement of the calibrations so that the telescopes are able discern cm/s level drifts in the measured Doppler shifts. Furthermore, utilizing optical frequency combs in light detection and ranging (LiDAR) applications was demonstrated quickly after the first OFCs were realized [11]. When using an OFC for LiDAR, employing not one but two OFCs in a dual-comb setup is beneficial for reducing the resolution from millimeter-range down to even nanometer-ranges [12]. Dual-comb setups can also be used for spectrography applications with linear optical sampling (LOS) measurements [13]. Utilizing LOS of the two combs with slightly offset repetition rates enable the down-conversion terahertz in the optical bandwidth down to megahertz in the RF domain, which makes it possible to reconstruct optical molecular absorption spectra.

As time progresses and research is done, the OFC-system tend to shrink in size, making them compacter and more viable, aiming to photonically integrate OFC sources [14, 15]. There are different ways to generate OFCs, but when it comes to semiconductor lasers, different platforms have been investigated, including mode-locked integrated external-cavity surface-emitting lasers (MIXSELs) [16, 17] and quantum cascade lasers (QCLs) [18, 19]. When MIXSELs are optimally pumped, they can provide femtosecond-pulses with an output power grater than 1 W. They can be engineered to work between 800 nm and near-infrared (IR) wavelengths. QCLs on the other hand offer the generation of mid-IR to terahertz radiation with variable mode-spacings. Their special feature is that QCL-combs do not produce optical pulses and are currently the only platform with direct electrical pumping. Furthermore, Electro-optic (EO) comb generators are employed to create OFCs [20]. They are currently the only source with wide-band and fast tuning of the mode spacing. There are also high-speed EO-modulators with pump wavelengths between 780 nm and 2 µm. One of the EO-combs was even used to calibrate an astronomical spectrograph [21]. Another way to generate optical frequency

combs, is to use microresonators. The generated OFCs, or also microcombs, differ in their operation from MLLs because they are not lasers, but only optical resonators. Microcombs were first demonstrated based on suspended silica micro-toroids [22, 23] and later in fused-quarz micro-rods [24], and . In the context of microcombs, microresonators act as build up cavities with high photon lifetimes, enabling high-nonlinearity through long-interaction lengths. Using four-wave mixing. a comb is generated by a single-frequency pump source that is resonantly coupled. Most of the research regarding microcombs was dedicated to understand the dynamics of generation a soliton source. This process of producing optical solitons is now fairly well understood and can by realized by systematic and careful control of the pump laser detuning [25, 15].

First, the optical frequency comb was created in order to increase the accuracy of atomic clocks, but over the time a great amount of additional applications was found, as the OFC becomes smaller, compacter and better understood. The microcomb is progressively getting more attention and is especially of great interest for this thesis.

2.2 Microresonator Optical Frequency Combs

As highlighted in the previous chapter, generation of optical frequency combs in microresonators, microcombs, have become more popular over the past two decades. Their small scale and with that the compactness makes viable for implementation into chip-scale photonic systems. Being made on a small-scale means also that the light is confined in a small physical volume, resulting in strong confinement of light, where the nonlinear effects are enhanced, aiding the broadening of the comb spectrum. Furthermore, they can achieve comb generation for relatively low input powers.

In other words, microcombs stand out because of their small size, compatibility with CMOS and integrability onto photonic circuits, enhanced confinemnet of light and less energy consumption.

This section is dedicated to microcombs. First, microresonators in general are reviewed, with a focus on whispering-gallery mode (WGM) microresonators. That focus is then further specified on microring resonators which are subject to this thesis, reviewing its characteristics and fabrication technique. Then, the theory behind the processes needed for comb generation inside of microresonators is shown, namely the effect of the third nonlinearity, the Kerr effect and the dispersion, which enable four-wave mixing (FWM) and generating microcombs. After introducing the different generatable comb stages, a closer look into the chaotic modulation instability (MI) combs and their applications is taken.

2.2.1 Microresonators

Microresonators gained interest since the previous century, leading to numerous different forms and shapes of microresonators [26, 27]. Systems based on optical microcavities were already substantial for applications like frequency stabilization, optical filtering and switching, cavity-quantum-electro-dynamic experiments, biosensing, light generation, and nonlinear optics. These resonators fabricated in a wide range of materials have radii from 1 to 100 µm. They trap light in their small physical volumes by processes such as almost total internal reflextion or distributed Bragg reflection. This confined light enables light amplification, and selection of specific frequencies of light that can be emitted or coupled into optical waveguides. Since microring resonators are subject to this study, whispering-gallery mode (WGM) resonators are presented in the following part.

WGM resonators, ring, rod, sphere

In 1909, RWTH Aachen University graduate and Nobel prize winner, Peter Debye, laid out the groundwork for an understanding of how electromagnetic waves respond to small spheres, especially those smaller than the wavelength of the light [28]. While he was not aware of whispering-gallery modes (WGM) at that time, his paper contributed to a better understanding on how resonances and thus WGM modes propagate in microresonators. But it was not until a year later, when Lord Rayleigh coined the concept of whispering-gallery modes, when he investigated acoustic whispering galleries [29, 30]. He studied how sound waves travel along the walls and ceilings in places like St. Paul's Cathedral, where whispers from the other side of the cathedral can be heard if one puts one ear close to the wall.

The concept of WGMs was brought to optical waves with contributions from Marcatili, who investigated bends in optical dielectric guides and how they behave in a closed loop [35]. Until the end of the 20th century different forms and shapes of WGM resonators were demonstrated, with a choice of resonators shown in Fig. 2.2. In table

Resonator	Microsphere	Microtorus	Microdisk	Racetrack
Q-factor	$10^7 - 9 \times 10^9$	5×10^8	$10^4 - 10^5$	850-1000

Table 2.1: Q-factors for the different types of microresonators as of 2006 [26]

2.1, the respective approximate Q-factor value can be seen. Starting with microspheres 2.2a, they exhibited the highest Q-factors $10^7 - 9 \times 10^9$, but are difficult to integrate on a chip because of their shape. Then, the microtorus 2.2b, it stood out because of its similar high Q-factors around 5×10^8, while being suitable for integration on a chip. Moreover, microdisks 2.2c showed still high Q-factors, $10^4 - 10^5$, while being smaller

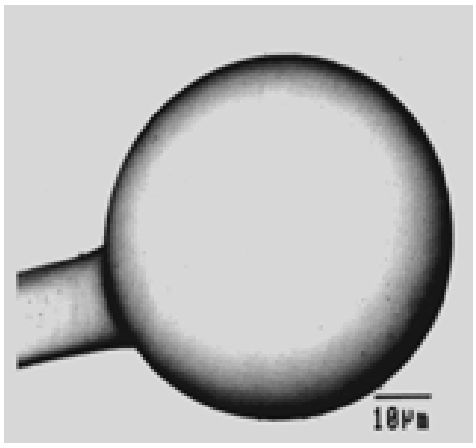

(a) Microsphere [31]

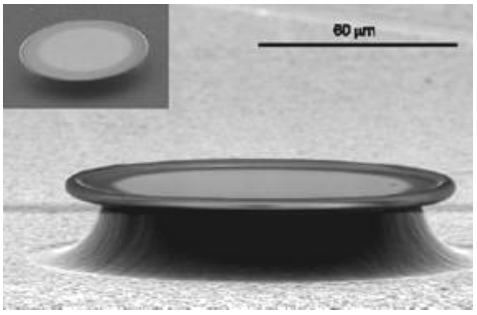

(b) Microtorus [32]

(c) Microdisk (microring) [33]

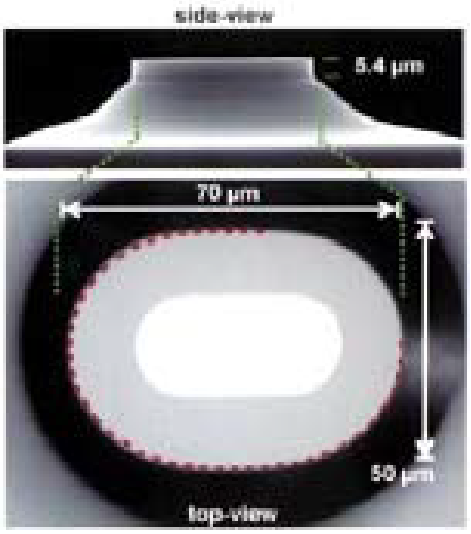

(d) Quadrupolar (racetrack) microresonator [34]

Figure 2.2: A choice of different WGM microresonators developed around 2000

than microtorii, their mode volume is also smaller and they are suitable for planar integration. Finally, quadrupolar (racetrack) microresonators 2.2d are able to efficiently couple to planar waveguides, but their Q-factors are even lower, 850-1000. This is also due to the fact, that the racetrack resonators are not pure WGM resonators but are also supporting bow-tie modes.

Resonance Frequencies, Roundtrip Time, Electrical Field

In the previous section a comparison of different types based on their Q-factors took place, without motivating what the Q-factor is. Therefore, the Q-factor along other characteristic values of the microresonator, specifically the microring resonator, are

introduced in the following sections. Since microring resonators have been studied for multiple decades, a lot of information can be acquired from textbooks, e.g. [36].

Typically, a microring resonator consists out of a looped waveguide along with a coupling mechanism enabling the access to it. As the waves propagate within the microring resonator and accumulate a phase shift equivalent to an integer multiple of 2π, constructive interference occurs, leading to resonance within the cavity. To put this into an equation, let ω_m be equivalently spaced resonance frequencies given by:

$$\omega_m = \frac{mc}{n_{\text{eff}}R} \tag{2.4}$$

$$m\lambda_m = 2\pi n_{\text{eff}}R, \tag{2.5}$$

where ω_m is the angular frequency of the m-th longitudinal mode, while λ_m is the corresponding wavelength, n_{eff} is the effective index of the mode, and R is the radius of the ring. As the phase shift of the resonant modes equals an integer multiple of 2π after each round-trip, the round-trip time T_{R} is multiplied by the angular resonance frequency,

$$\omega_m T_{\text{R}} = m2\pi. \tag{2.6}$$

To get an ample equation for the round-trip, insert 2.5 into 2.6,

$$T_{\text{R}} = \frac{m2\pi}{\omega_m} \tag{2.7}$$

$$= \frac{m2\pi}{\frac{mc}{n_{\text{eff}}R}} \tag{2.8}$$

$$= \frac{2\pi n_{\text{eff}}R}{c} \tag{2.9}$$

$$= \frac{n_{\text{eff}}L}{c} \tag{2.10}$$

where $L = 2\pi R$ is the circumference of the microresonator, the length the light travels in one round-trip. Furthermore, the free-spectral range (FSR) can be introduced, also illustrated in Fig.2.3. The FSR is the separation of successive resonances, so it is directly obtained by the difference of two successive resonances:

$$\text{FSR}_{\text{frequency}} = \omega_{m+1} - \omega_m = \frac{2\pi}{T_{\text{R}}} \tag{2.11}$$

$$= \frac{2\pi c}{Ln_{\text{eff}}} \tag{2.12}$$

Or when translated into wavelength,

$$\text{FSR}_{\text{wavelength}} = \frac{\lambda_0^2}{n_{\text{eff}}L} \tag{2.13}$$

where λ_0 is the free-space wavelength, is obtained. Furthermore, when looking at figure 2.3, the resonance width $\Delta\omega$ is visible, which is just the full-width at the half maximum of the resonance.

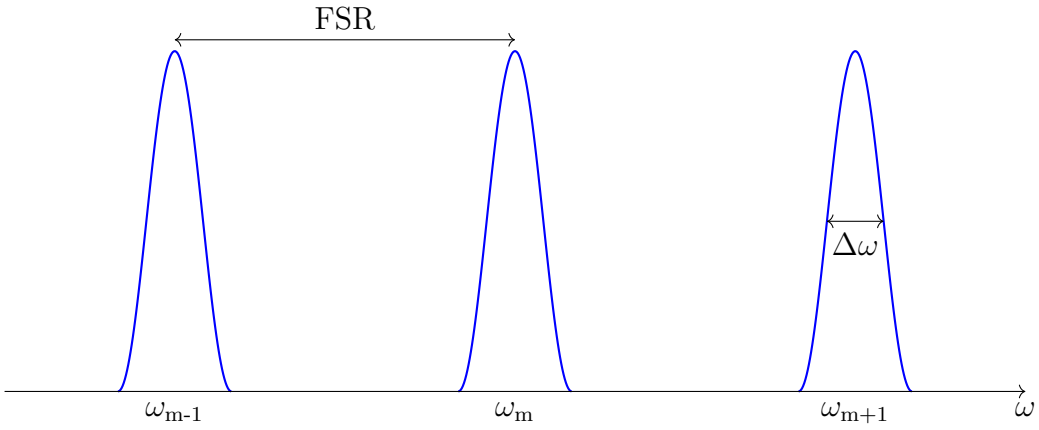

Figure 2.3: Resonances of a Microresonator

Finally, the internal optical field $A(z,t)$ can be written as

$$A(z,t) = A_0 \exp(\mathrm{i}(kz - \omega_m t)), \tag{2.14}$$

where A_0 is the amplitude and $k = 2\pi m/L$ is the propagation constant.

Quality Factor and Finesse

A popular way to compare different microring resonators is by looking at their quality factor (Q) next to other values [37]. The following derivation is based on [36]. To define the Q-factor, one has to know that it is a measure of the sharpness of the resonance with respect to its central frequency. When putting this into an equation, it can be seen that it is the ratio of the stored energy in the resonator to the energy lost per round trip:

$$Q = \omega_0 \frac{\text{Stored energy}}{\text{Power loss}}. \tag{2.15}$$

The stored energy is given by the squared amplitude of the previously defined optical intrinsical field A_0, $|A_0|^2$. But, since the power loss depends on the time, the transient process is evaluated. Let a resonator be loaded with an intensity of $|A_0|^2$, after the charging process the pump is turned off, so that the resonator loses its energy. To derive a differentiable function for the energy, consider the intensity after the n-th round-trip:

$$|A_n|^2 = \exp(-\alpha_{\text{dis}} L)|A_{n-1}|^2 \tag{2.16}$$

$$= \exp(-n\alpha_{\text{dis}} L)|A_0|^2 \tag{2.17}$$

where α_{dis} is the distributed loss in the resonator. After each round-trip the intensity of the previous round-trip is attenuated by a factor $\exp(-\alpha_{\text{dis}}L)$. Let n be large enough to declare this relation a continuous variable and it can be derived with respect to n, which is indirectly a measure of time, because each round-trip takes T_R. The power loss can be directly evaluated to:

$$\frac{\mathrm{d}|A_n|^2}{\mathrm{d}n} = -\alpha_{\text{dis}}L|A_n|^2 \tag{2.18}$$

$$\frac{\mathrm{d}|A_n|^2}{\mathrm{d}t} = \frac{1}{T_R}\frac{\mathrm{d}|A_n|^2}{\mathrm{d}n} = -\frac{\alpha_{\text{dis}}L}{T_R}|A_n|^2 \tag{2.19}$$

Since the power loss has to be positive value by definition, the derived term has to be negated before inserted into 2.15. Finally,

$$Q = \omega_0 \frac{|A_0|^2}{-\frac{\mathrm{d}|A_n|^2}{\mathrm{d}t}} \tag{2.20}$$

$$= \frac{\omega_0 T_R}{\alpha_{\text{dis}}L} \tag{2.21}$$

With the resonance width of ω_0, which can be defined as:

$$\Delta\omega = \frac{\alpha_{\text{dis}}L}{T_R}, \tag{2.22}$$

the common formal form of the Q-factor is usually defined as

$$Q = \frac{\omega_0}{\Delta\omega} = \frac{\lambda_0}{\Delta\lambda}. \tag{2.23}$$

A similar measure is the finesse, which is defined as the ratio of FSR and resonance width,

$$\text{Finesse} = \frac{\text{FSR}}{\Delta\omega}. \tag{2.24}$$

Therefore, the Finesse is the measure of the sharpness of resonances relative to their spacing. Both, the finesse and Q-factor have a physical meaning, namely they are proportial to the number of round-trips that can be made with the energy stored in the resonator. In detail, their meanings differ by a bit. The finesse is approximately the number of round-trips the light inside the cavity can make until its energy is depleted to $1/e$ of its initial value. In contrast to that, the Q-factor represents the number of oscillations the field inside the resonator can make until its energy is reduced to $1/e$.

Since there are different definitions of the Q-factor [38, 39, 40, 41], and they are usually defined for the uncoupled case, consider the following as the definition used in

this thesis:

$$Q_{\text{load}}^{-1} = Q_{\text{rad}}^{-1} + Q_{\text{scatter}}^{-1} + Q_{\text{cont}}^{-1} + Q_{\text{mat}}^{-1} + Q_{\text{coup}}^{-1} \tag{2.25}$$

$$= Q_{\text{int}}^{-1} + Q_{\text{coup}}^{-1}, \tag{2.26}$$

where Q_{rad}^{-1} are the radiative losses; Q_{scatter}^{-1} the scattering losses due to surface inhomogeneities; Q_{cont}^{-1} losses due to contaminants on the surface of the resonator; Q_{mat}^{-1} the material losses and Q_{coup}^{-1} the losses because of coupling. The unloaded Q-factor is here called intrinsic Q-factor Q_{int}^{-1}. When talking about the loaded Q-factor, the coupled resonator is meant, and also the Q-factor that is measured in the experiment, when measuring the resonances center wavelengths and the resonance width.

Similarly to the Q-factor, the different losses in the resonator can be summarized to:

$$\gamma = \gamma_{\text{rad}} + \gamma_{\text{scatter}} + \gamma_{\text{cont}} + \gamma_{\text{mat}} + \gamma_{\text{coup}} \tag{2.27}$$

$$= \gamma_{\text{int}} + \gamma_{\text{coup}}. \tag{2.28}$$

Coupling Mode Theory applied to Waveguide and Resonator

Utilizing the coupling mode theory [42, 43, 36], the coupling between waveguide and resonator can be shown [44, 45]. Assuming waveguide and the microring resonator are physically close enough, meaning the gap between the edge of the resonator and the waveguide is short enough, coupling between supported modes is feasible.

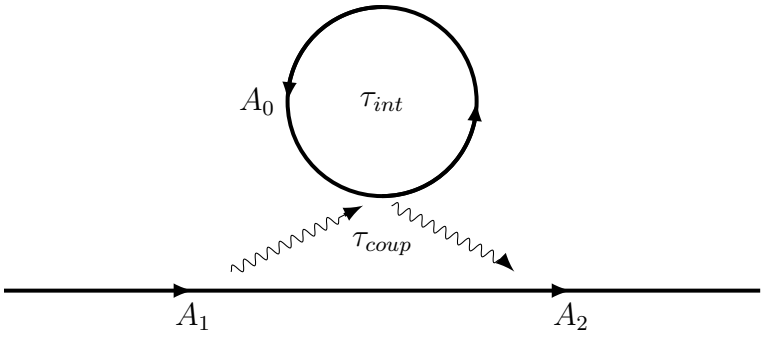

Figure 2.4: Coupling between ring and waveguide

Consider the schematic shown in 2.4, which shows the basic coupling relation between microring resonator and a waveguide. The incident field A_1, the transmitted field A_2 and the circulating field inside the resonator A_0 are related with the intrinsic decay rate, τ_{int}^{-1}, and the coupling rate, τ_{coup}^{-1} by the following equations. First, let the time variation of the circulating mode, A_0, be as follows [43]:

$$\frac{\mathrm{d}A_0(t)}{\mathrm{d}t} = -\left(\frac{1}{2\tau} + i\omega_0\right) A_0(t) + \frac{1}{\sqrt{\tau_{coup}}} A_1(t) \exp(-i\omega_1 t) \tag{2.29}$$

where ω_1 is the frequency of the incident light and $\tau^{-1} = \tau_{int}^{-1} + \tau_{coup}^{-1}$ is the total loss rate in the cavity. To determine the detuning between incident light and the resonating mode in the resonator, a phase transformation is applied, namely $\overline{A}_0(t) = A_0(t)\exp(i\omega_1 t)$. And the previous equation is reformulated as,

$$\frac{\mathrm{d}\overline{A}_0(t)}{\mathrm{d}t} = \left(i(\omega_1 - \omega_0) - \frac{1}{2\tau}\right)\overline{A}_0(t) + \frac{1}{\sqrt{\tau_{coup}}}A_1(t). \tag{2.30}$$

In this formulation the detuning, $\omega_1 - \omega_0$, can directly be evaluated. Furthermore, let the transmitted field $A_2(t)$ be defined as,

$$A_2(t) = \frac{1}{\sqrt{\tau_{coup}}}\overline{A}_0(t) - A_1(t). \tag{2.31}$$

The transmission factor is now derived by analyzing the steady-state, when the time variation of the intracavity field disappears, $\frac{\mathrm{d}\overline{A}_0(t)}{\mathrm{d}t} = 0$:

$$\overline{A}_0 = \frac{1}{\sqrt{\tau_{coup}}}\frac{1}{i(\omega_1 - \omega_0) - \frac{1}{2\tau}}A_1 \tag{2.32}$$

$$|\overline{A}_0|^2 = \frac{1}{\tau_{coup}}\frac{1}{(\omega_1 - \omega_0)^2 + \frac{1}{4\tau^2}}|A_1|^2 \tag{2.33}$$

Now, to evaluate the transmission factor, consider the ratio from output to input is calculated in the case of no detuning, $\omega_1 = \omega_0$,

$$T = \frac{P_{\text{out}}}{P_{\text{in}}} = \left|\frac{A_2}{A_1}\right|^2 = \left(\frac{\tau_{int} - \tau_{coup}}{\tau_{int} + \tau_{coup}}\right)^2 \tag{2.34}$$

According to equations from Bogaerts [41] and Spillane [44], a derivation of the coupling factor K is presented. They show that the transmission in the steady state can be expressed as

$$T = \left(\frac{1 - K}{1 + K}\right)^2 \tag{2.35}$$

where K is the coupling parameter, which can be defined as

$$K = \frac{1 \pm \sqrt{T}}{1 \mp \sqrt{T}}. \tag{2.36}$$

The upper signs are taken, when the resonator is over-coupled and the lower signs are taken when the resonator is under-coupled. In the critically coupled case, the transmission vanishes, $K = 1$. As the transmission T is defined as the transmission when the detuning equals 0, this equation can also be used to determine the coupling factor in the experiment. Furthermore, when comparing equations 2.34 and 2.35 , the

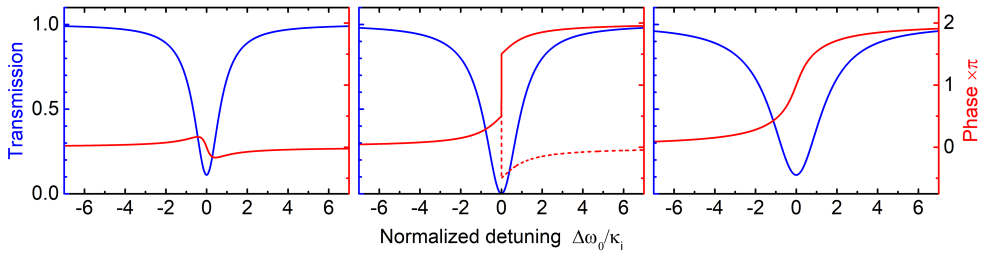

Figure 2.5: Resonances for different coupling factors

coupling factor can also be defined as,

$$K = \frac{\tau_{coup}}{\tau_{int}}. \tag{2.37}$$

In figure 2.5, the three different cases of coupling are presented. From left to right, the under coupled, critically coupled and over coupled cases are shown, which depend on the previously defined coupling factor K.

- Under coupling $Q_{int} < Q_{\text{coup}}$, $K < 1$ ($\tau_{int}^{-1} > \tau_{\text{coup}}^{-1}$): When the coupling rate is smaller than the intrinsic decay rate, less light is coupled in and as a result there is more transmitted light than light from the cavity at the output.
- Critcal coupling $Q_{int} = Q_{\text{coup}}$, $K = 1$ ($\tau_{int}^{-1} = \tau_{\text{coup}}^{-1}$): When the coupling rate equals the intrinsic decay rate, there is no transmitted light behind the resonator, since all the light is coupled into the resonator. While the amplitude of the transmitted field is the same as the amplitude as the field that came back from the resonator, a resonance shift of π between both occurs.
- Over coupling $Q_{int} > Q_{\text{coup}}$, $K > 1$ ($\tau_{int}^{-1} < \tau_{\text{coup}}^{-1}$): As the coupling rate is higher than the intrinsic decay rate, more light is coupled into the cavity than before, resulting in a majority of the output signal being from the cavity and not directly transmitted from the incident source.

Fabrication of Silicon Nitride Ring resonators

To fabricate the microresonators are technique called the photonic Damascene process is used [46]. In Fig. 2.6, the fabricated chip can be seen. On the left 2.6a, the structures on the chip are visible in a close-up. On the right 2.6b, the packaged chip is depicted which makes adressing the waveguides leading to the resonators easier.

2.2.2 Comb Generation

It was found out that microresonators are also feasible for optical frequency comb generation, leading to multiple groups investigating the so-called microcomb generation[23,

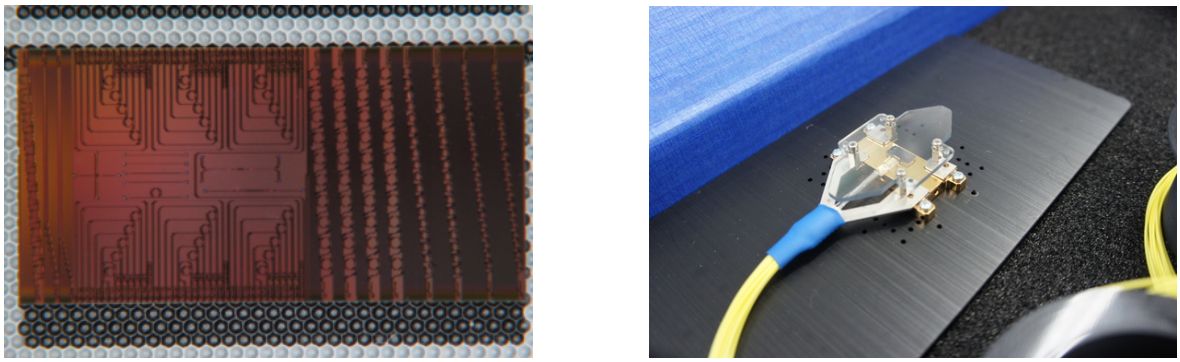

(a) Fabricated Chip (b) Packaging around the chip

Figure 2.6: Used chip in the experiments

22, 47]. A conclusive paper about microcombs and the dynamics of temporal solitons in microresonators was published in 2014 by Herr et al [25]. The fundamentals to understand why this microcomb generation is even feasible have to be motivated before. For the following explanations the textbook titled "Nonlinear Fiber Optics" by Govind P. Agrawal is used [48]. Microcombs are also called Kerr frequency combs, because one of the effects that is necessary for microcomb generation is the inherent Kerr effect in the microcavities. With the Kerr nonlinearity and the dispersion of the microresonator, the optical field inside the cavity can be described by the Lugiato-Lefever equation which is exemplified later in the simulation chapter 3. The actual comb generation happens then because of an effect called four-wave mixing (FWM). At last the Thermo-Optic effect is shortly introduced because of its importance in the experimental part.

Optical Kerr Effect

While the principle of Kerr frequency combs is applicable to any type of optical resonator, the requirement for Kerr frequency comb generation is the pump laser field intensity is above the parametric threshold of the nonlinear process. Which is easier to fulfill inside a microresonator because of the low losses inside microresonators (and corresponding high quality factors) and because of the microresonators' small mode volumes. The optical nonlinearities refered to become visible when the polarization of a dielectric material scales nonlinearly. Induced by the electrical field, here, electromagnetic waves, the polarization changes dependent on the intensity of the input light. Usually, the polarization is linear as the electrical, or rather the optical field, $E(z,t)$, is too small to generate a significant nonlinear effect. Therefore, a common way to characterize the polarization, $P(z,t)$, is by neglecting the nonlinearities altogether,

$$P = \epsilon_0 \chi E, \tag{2.38}$$

where ϵ_0 is the vacuum permittivity and χ the electrical susceptibility. A general definition, that includes all terms, is given by

$$P = \epsilon_0(\chi E + \chi^{(2)}E^2 + \chi^{(3)}E^3 + \dots), \tag{2.39}$$

where the terms $\chi^{(2)}$ and $\chi^{(3)}$ denote the second- and third-order susceptibility, respectively. Since fibers are usually made from silica and the resonators used in this thesis are made from silicon nitride, Si_3N_4, the second-order nonlinearity vanishes because of their centrosymmetry [49]. That leaves the nonlinearity to the third-order susceptibility. Higher-order susceptibilities are neglected, because their effect is marginal compared to the third-order nonlinearity. The lowest-order nonlinear effects in silica glass and silicon nitride originate from this third-order susceptibility $\chi^{(3)}$ which is also responsible for phenomena such as the optical Kerr effect and four-wave mixing. Thus, the nonlinear polarization is described as,

$$P_{\mathrm{NL}} = \epsilon_0\chi^{(3)}E^3. \tag{2.40}$$

Most above mentioned nonlinear effects originate from nonlinear refraction, the phenomenon that the refractive index is intensity dependent. Written in its simplest form, the refractive index looks like this:

$$\tilde{n}(\omega, |E|^2) = n(\omega) + n_2|E|^2, \tag{2.41}$$

where $n(\omega)$ is the linear part, which is commonly known and $|E|^2$ is the optical intensity. n_2 is the second-order nonlinear-index coefficient that is proportional to $\chi^{(3)}$.

$$\frac{3\chi^{(3)}}{4\epsilon_0 c n_0^2} \tag{2.42}$$

The two most widely studied nonlinear effects due to the intensity change of the refractive index are called self-phase modulation (SPM) and cross-phase modulation (XPM). SPM describes the phase shift which is self-induced after propagating through an optical fiber of a length L.

$$\phi = \tilde{n}k_0L = (n + n_2|E|^2)k_0L, \tag{2.43}$$

where $k_0 = 2\pi\lambda$. The second addend describes the intensity-dependent nonlinear phase-shift which is due to the SPM:

$$\phi_{NL} = n_2k_0L|E|^2. \tag{2.44}$$

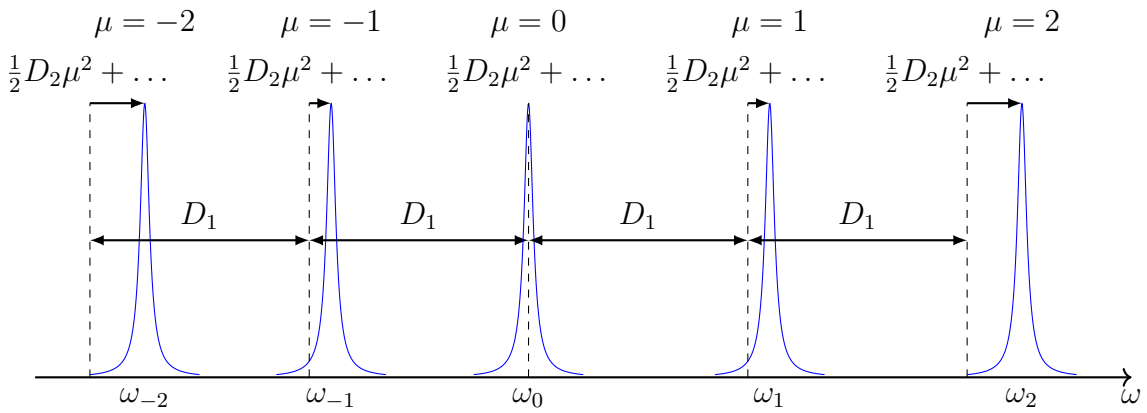

Figure 2.7: Dispersion in a microresonator

In contrast to SPM, XPM refers to the nonlinear phase shift of an optical field due to another optical field with a different wavelength, direction, or state of polarization. Consider the total electric field for two optical fields with different frequencies ω_1 and ω_2, polarized along the z axis, propagate at the same time,

$$E = \frac{1}{2}\hat{z}[E_1 \exp(-i\omega_1 t) + E_2 \exp(-i\omega_2 t) + \text{c.c.}]. \tag{2.45}$$

Then, the nonlinear phase shift for the optical field with the frequency ω_1 is expressed by:

$$\phi_{\text{NL}} = n_2 k_0 L(|E_1|^2 + 2|E_2|^2), \tag{2.46}$$

where other frequencies than ω_1 and ω_2 are neglected. On the right-hand side (RHS) of Eq. 2.46, the terms are a result of SPM and XPM, respectively. Important to note, the effect of XPM is twice the effect of SPM when both fields of different frequencies are of similar intensity.

Dispersion

Another important characteristic of the microresonator which enables microcomb generation is the dispersion, which consists out of two contributions, the material dispersion and the geometry dispersion. The material dispersion can be calculated when approximating the refractive index with the Sellmeier equation. But the geometry dispersion has a stronger effect in waveguides and microring resonators.

In contrast to the material dispersion which depends on the refractive index, the geometry dispersion originates from the propagation constant in the resonator which is wavelength-dependent. The resonance frequencies for an arbitrary mode μ are given

in a Taylor-expanded form as:

$$\omega_\mu = \omega_0 + D_1\mu + \frac{1}{2}D_2\mu^2 + \frac{1}{6}D_3\mu^3 + \dots \tag{2.47}$$

where ω_μ is the frequency of the resonance mode, ω_0 is the frequency of the center mode, D_i are the dispersion coefficients and μ the mode number. D_1 is a directly related to the physical dimensions of the resonators, as it is the FSR multiplied by 2π, $\mathrm{FSR} = \frac{D_1}{2\pi}$, or in terms of the round-trip time, $T_R = \left(\frac{D_1}{2\pi}\right)^{-1}$. Figure 2.7 exemplifies the above Eq. 2.47. Higher-order dispersion coefficients are usually neglected because of the exponential decrease of their influence, $D_2 \gg D_3 \gg \dots$. D_2 is next to D_1 a coefficient of relevance, because the sign determines the kind of dispersion.

- $D > 0$ means anomalous dispersion
- $D < 0$ denotes normal dispersion

Furthermore, it is common to express the dispersion with the group velocity dispersion β_2:

$$\beta_2 = -\frac{nD_1}{cD_1^2}. \tag{2.48}$$

Thus, the dispersion inside microresonators is an important parameter that can to be tuned in order to adjust the behavior or the shape of the microcomb.

Thermo-Optic Effect

Not only the dispersion, but also the temperature can shift the resonances [50, 51]. While the dispersion depends mainly on the resonators geometry, which usually does not change a lot during use, the temperature does change dramatically depending on the input pump power.

The resonance wavelength can be analyzed with respect to the temperature and an equation can be extracted[51]:

$$\lambda_r(\Delta T) = \lambda_0 \left[1 + \left(\epsilon + \frac{\frac{\mathrm{d}n}{\mathrm{d}T}}{n_0}\right)\Delta T\right] \tag{2.49}$$

$$= \lambda_0(1 + a\Delta T). \tag{2.50}$$

λ_0 is the cold cavity resonance-wavelength, ϵ is the expansion coefficient of the cavity, $\frac{\mathrm{d}n}{\mathrm{d}T}$ is the refractive index temperature coefficient and ΔT is the temperature difference between the mode volume and the surrounding. Furthermore a factor a is introduced for simplicity. This factor a can then be calculated for different materials, where $a > 0$ for many optical materials including silica and Si_3N_4. Because of the positive sign of

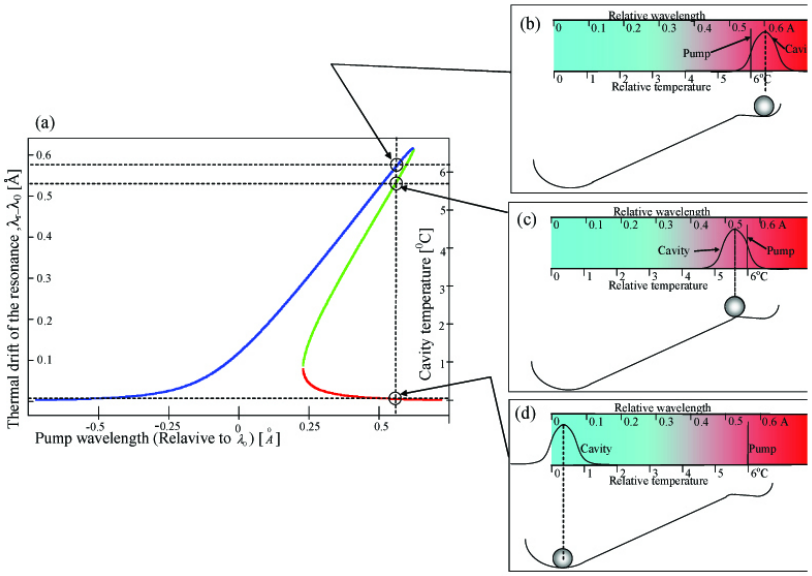

Figure 2.8: (a) Thermal Drift of the resonance wavelength, (b),(c) and (d) three different equilibrium states

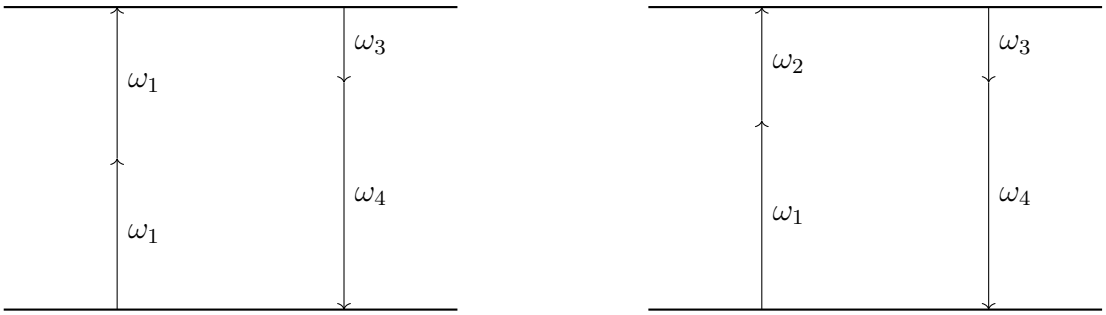

(a) Degenerate FWM

(b) Non-degenerate FWM

Figure 2.9: Energy diagrams Four-Wave Mixing

the coefficient a the resonance wavelength is shifted to a higher wavelength when the temperature inside the cavity rises because of the increased coupling the nearer the pump wavelength comes to the resonance wavelength, depicted in Fig. 2.8. Due to this shifting of the resonance wavelength to higher values, when the pump wavelength is also increased, the resonator is passively stabilizing itself, when the pump wavelength is smaller than the resonance wavelength (blue-detuned), b) in Fig. 2.8. In the other case, when the pump wavelength is already longer than the resonance wavelength (red-detuned), the field inside of the cavity is prone to thermal instability, c) in Fig. 2.8.

Four-Wave Mixing

Four-wave mixing (FWM) can be understood as one of the key mechanism to generate a microcomb as its important for creating the first stage of the comb [52, 53]. In FWM two photons are annihilated and again created, where it is differentiated between

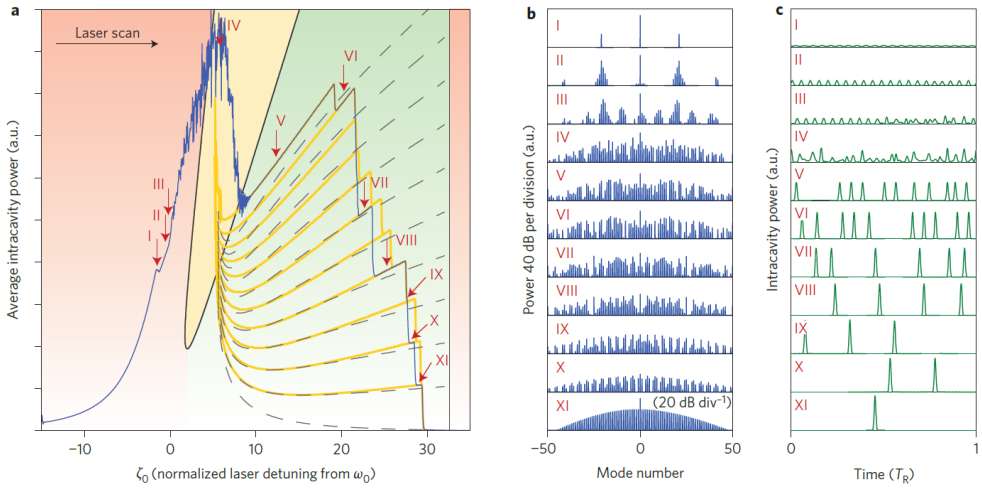

Figure 2.10: Numerical simulations of soliton formation in a microresonator from [25]

two main concepts, degenerate and non-degenerate FWM. In the following equations the energy-equilibriums of the degenerate and the non-degenerate FWM processes are described,

$$2\hbar\omega_1 = \hbar\omega_3 + \hbar\omega_4 \text{ (degenerate)} \tag{2.51}$$

$$\hbar\omega_1 + \hbar\omega_2 = \hbar\omega_3 + \hbar\omega_4 \text{ (non-degenerate)} \tag{2.52}$$

where ω_i are the different frequencies the photons are created and annihilated, $\hbar$ is Planck's constant. The processes are also depicted in Fig. 2.9. On the left 2.9a, two photons with the same frequency, ω_1, are annihilated and two photons with different frequencies, $\omega 3$ and ω_4, are generated, which is called degenerate FWM. On the right 2.9b, two photons with different frequencies, ω_1 and ω_2, are annihilated and two photons with different frequencies, ω_3 and ω_4, are generated, which is called non-degenerate FWM. It is important to note that the phases need to be matched.

2.2.3 Modulation Instability Comb

The dynamics of the generation of microcombs was first extensively studied by Herr et al. in 2014 [25]. In Fig. 2.10, the results of a numerical analysis of the generation of microcombs in microresonators is depicted. There are different stages, which all occur during the sweep of the pump wavelength. Shown in figure (a) is the average intracavity power with respect to the laser detuning. As the pump wavelength is swept from smaller to longer wavelengths, the intracavity power also changes. First, in the red-detuned regime, when the pump wavelength is smaller than the effective resonance wavelength, the power rises until the pump wavelength matches the effective resonance wavelength. In figure (b) and figure (c) the corresponding optical spectra and temporal

waveforms are shown for the respective points marked in figure (a). It starts with a Turing pattern comb which gets more chaotic and evolves into an MI comb in point (IV). Beyond this point, the microresonator moves into the blue-detuned regime, where first a multi-soliton comb can be seen, which reduces to a single-soliton comb, by further tuning of the pump wavelength.

Out of all the different stages, the one of interest for this thesis is the MI comb, as it shows chaotic behavior and can thus be used for multiple applications. Especially from last year, the interest in modulation instability microcombs seems to be increased in the photonic community. First, Lukashchuk et al. and Chen et al. idependently from each other were able to implement LiDAR systems based on MI microcombs, which outperform traditional ones [54, 55]. Using MI microcombs and their quasi-random signals opens the door to randomly generate bits and use the randomness for computing, e.g., decision making, Monte-Carlo simulations, etc.. Shen et al. were able to achieve a random bit generation rate of $3.84\,\mathrm{Tbit\,s^{-1}}$ and solved up to 256-armed bandit problems with one MI microcomb [56]. The random bit generation rate can further be increased, when using a microresonator with an even smaller FSR, e.g., to approximately $10\,\mathrm{Tbit\,s^{-1}}$ [57].

One of the unrealized applications the authors of the above mentioned papers started talking about, is the synchronization of two chaotic microcombs and the consequently chaos secure communication.

2.3 Chaos

One might already have heard of the so-called "butterfly-effect", which is a term that was coined in chaos theory but finds itself in common media because of its simple interpretation. One of the most famous talks by Lorenz about the unpredictability of complex systems, or more specifically when trying to predict the weather, is probably "Predictability: Does the Flap of a Butterfly's Wings in Brazil Set off a Tornado in Texas?" [58]. The butterfly in the "butterfly-effect" plays the metaphorical role of the initial conditions of a complex system and states that even the smallest and seemingly most insignificant changes in the initial conditions can change the outcome of an chaotic system. Research efforts are summarized in textbooks [59], there are even books for non-mathematical people [60].

2.3.1 Fundamentals

As already motivated by the "butterfly-effect" chaos is very sensitive to its initial conditions and might seem random, even though chaos is a deterministic phenomenon.

Therefore, it is a hot research topic since the last century, where significant progress has been made regarding the theory of chaos, which is summarized in multiple textbooks. Chaos can be described by the Lorenz equations:

$$\dot{x} = \sigma(y - x) \tag{2.53}$$

$$\dot{y} = rx - y - xz \tag{2.54}$$

$$\dot{z} = xy - bz, \tag{2.55}$$

where σ, r, $b > 0$ are parameters. This three-dimensional system was derived by Edward Lorenz in 1963 [61], when he studied to predict the weather. Even though, he derived these equations for the nonlinear flow of convection rolls, the same model can also be applied to lasers or dynamos. While it looks like a simple deterministic system, it can have tremendously peculiar dynamics, where the system oscillates irregularly, which never repeats exactly, but always remains within boundaries. There are two important concepts when it comes to chaos

- Stretching
- Folding,

which both describe the chaotic system. Stretching is responsible for the sensibility to initial conditions, meaning successive points are moving apart from each other. The folding process is responsible for keeping the boundaries of the complex set, where a point that was stretched before is folded back to a different part of the complex set. These two processes can be compared two kneading a dough, where one also usually stretches and folds the dough until its kneaded thoroughly enough. In this example, the dough-particles are thus behaving chaotically.

Strange Attractor

When plotting the trajectories of the Lorenz equations in three dimensions, these points resolve into a complex set, that is now called a strange attractor. When analyzing the chaos of a system this strange attractor might give feedback on the degree of chaos of the system. Staying with Lorenz for this, the famous Lorenz attractor is depicted in Fig. 2.11a, which coincidentally looks like a butterfly. Another example of the motion of the three-dimensional plotted in 3 dimensions for another set of equations is shown in Fig. 2.11b. The equations which this system is based upon are named after Rössler who derived them in 1976 [62]. The Rössler attractor shows clearly how the folding process can be understood, because in the strange attractor a flap in z-direction (upwards) can be seen that is folded upon the other parts of the strange attractor.

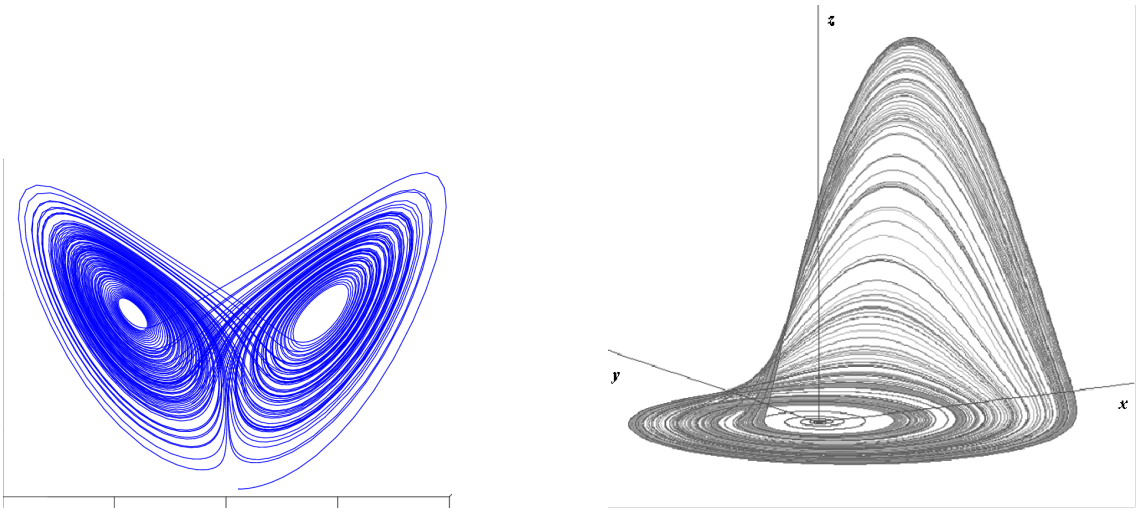

(a) Lorenz Attractor from [63] (b) Rössler Attractor from [64]

Figure 2.11: Example Strange Attractors

There is a number of different strange attractors which differ from the Lorenz and Rössler attractors, but they have all in common, that quasi-random points settle onto a complex set, which is evolving to a strange attractor over time. It is important to note, that measuring a chaotic system and plotting it in three dimensions might not yield a strange attractor because the systems is observed from the outside without knowing the exact model inside.

Lyapunov Exponent

A more quantitative way of analyzing the chaos in a system is to characterize it by the Lyapunov exponent. It is also a measure for the earlier mentioned stretching process. In other words, it measures the speed of growth of the infinitesimally close distance between two initially close states:

$$F^t(x_0 + \epsilon) - F^t(x_0) \approx \epsilon e^{\lambda t} \tag{2.56}$$

The left-hand side (LHS) of the equation is describing the distance between two initially close points x_0 and $x_0 + \epsilon$ at time step t. The RHS is assuming exponential growth of the distance between both points, where λ is the Lyapunov exponent when measured for a long time, which is ideally $t \to \infty$. Now, based on this Lyapunov exponent the stretching of a system can be determined, because depending on the sign in from of the exponent, the behavior of the system is described to:

- $\lambda < 0$: Small changes are not growing indefinitely, meaning the system will eventually become periodic.

- $\lambda > 0$: Small changes are growing indefinitely over time, which means that the points are stretched apart from each other.

Important to note, the Lyapunov effect only gives information about the stretching of a system but not its folding.

To bring Eq. 2.56 into a computable form, solve for λ:

$$e^{\lambda t} \approx \frac{|F^t(x_0+\epsilon) - F^t(x_0)|}{\epsilon} \tag{2.57}$$

$$\lambda = \lim_{t\to\infty,\epsilon\to 0} \frac{1}{t} \log \frac{|F^t(x_0+\epsilon) - F^t(x_0)|}{\epsilon} \tag{2.58}$$

$$= \lim_{t\to\infty,\epsilon\to 0} \frac{1}{t} \log \left| \frac{\mathrm{d}F}{\mathrm{d}x} \right|_{x=x_0} . \tag{2.59}$$

In order to calculate the Lyapunov exponent for discrete time systems $x_{t+1} = F^t(x_t)$, when the time-discrete system started with x_0,

$$\lambda(x_0) = \lim_{t\to\infty} \frac{1}{t} \sum_{i=0}^{t-1} \log \left| \frac{\mathrm{d}F}{\mathrm{d}x} \right|_{x=x_i} , \tag{2.60}$$

can be used. Which is quite simple to implement into a simulation but might by hard to evalualate in an experiment, because of derivative of the function $F(x)$ is needed, which is not exactly measurable.

Bifurcation Diagram

Another way of visualizing chaos of a complex system is by utilizing a bifurcation diagram. An example is shown in Fig. 2.12, where a simple nonlinear equation, the logistic map is shown [65].

$$x_{n+1} = r x_n (1 - x_n) \tag{2.61}$$

On the horizontal axis, the bifurcation parameter r is shown. The bifurcation diagram depicts the forking of the periods of stable points, where this doubles with each bifurcation. When investigating the intervals of successive intervals between bifurcations, the ratio of the distances converges to the Feigenbaum constant [66], which is defined as:

$$\delta = \lim_{n\to\infty} \frac{r_{n-1} - r_{n-2}}{r_n - r_{n-1}} = 4.669\ldots . \tag{2.62}$$

It was generally shown that all chaotic systems which correspond to a one-dimensional map with a single quadratic maximum, bifurcate at that bifurcation speed. Thus, calculating the Feigenbaum can yield insights on the chaotic behavior of a system.

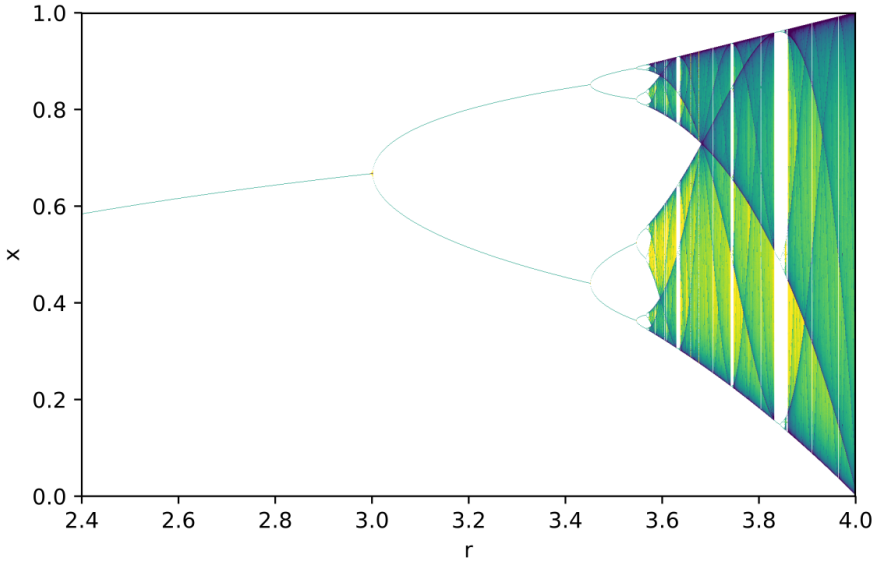

Figure 2.12: Bifurcation Diagram of the Logistic Map

2.3.2 Synchronization

Chaos synchronization goes back to the 17th century when Huygens found out, that two chaotic oscillators could be synchronized by coupling them, which coincides with the maths behind it. As seen above, a chaotic system possesses a positive Lyapunov exponent, meaning that the distance between two initially close points will always be stretched out. While it might be possible to set the initial conditions to be exactly the same in a computer simulation, in reality this will never be possible, because as motivated earlier, even an infinitesimal change in the initial conditions yields completely different trajectories. Therefore, a form of coupling is crucial, when synchronizing chaos. This was shown when chaos synchronization was first really understood in 1990 by Pecora and Carroll [67], where they showed the synchronization of two three-dimensional chaotic systems, when the second one is coupled to the first on. In particular, they showed how it is feasible to drive the second source only be one variable of the leader system and the other two variables would start to follow the untransmitted variables of the first chaotic source. Despite chaos synchronization being achieved, full theoretical understanding has not been established yet.

Instead, the focus lies on the synchronization of chaotic systems and applications, therefore the concept of synchronizing two chaotic sources is reviewed [68]. In Fig. 2.13, the general idea of chaos synchronization is presented. A leader-follower configuration

Figure 2.13: General Idea of Chaos Synchronization

is utilized, where the chaotic signal from the transmitter is input into the receiver. But utilizing the whole chaotic signal is uninteresting as one also wants to transmit an encrypted signal. Luckily, as Pecora and Caroll showed before, it is not needed to use the complete chaotic signal to achieve chaos synchronization between the leader and follower system. So, only a part of the chaotic signal is transmitted, and the follower system is adjusting itself to the leader system.

Consider a chaotic transmitter system, which is described by the vector variables $\boldsymbol{u}$ and $\boldsymbol{v}$. This chaotic system is then split into two subsystems, which are then defined as $f(\boldsymbol{u}, \boldsymbol{v})$ and $g(\boldsymbol{u}, \boldsymbol{v})$ to describe the nonlinearities in the system.

$$\frac{\mathrm{d}\boldsymbol{u}}{\mathrm{d}t} = f(\boldsymbol{u}, \boldsymbol{v}) \tag{2.63}$$

$$\frac{\mathrm{d}\boldsymbol{v}}{\mathrm{d}t} = g(\boldsymbol{u}, \boldsymbol{v}) \tag{2.64}$$

As both subsystems depend on each other, they are mutually coupled. Furthermore, it is assumed that the output of the chaotic system, $\boldsymbol{u}$ and $\boldsymbol{v}$, is chaotic. The receiver system on the other hand consists only of one of the subsystems:

$$\frac{\mathrm{d}\boldsymbol{w}}{\mathrm{d}t} = f(\boldsymbol{w}, \boldsymbol{v}). \tag{2.65}$$

Before the transmitter is sending a signal to the receiver, the vector variable $\boldsymbol{v}$ is treated as a constant vector. Although the subsystem is described as a nonlinear function, it does not require the output of the receiver system to be oscillating chaotically, meaning before the transmitters signal is received the receiver might as well behave like a periodic oscillator. Even if the receiver is behaving chaotically and the output $\boldsymbol{w}$ is oscillating chaotically, it will never follow the same chaotic signal of $\boldsymbol{u}$, without a signal from the transmitter. However, when a portion of the output from the transmitter, here $\boldsymbol{v}$, is sent to the receiver, both, the transmitter and receiver are synchronizing, so that the $\boldsymbol{u}$ and $\boldsymbol{w}$ show the same signals. But they are only synchronizing under the correct circumstances, meaning the right choice of subsystems and the correct setting of parameters, like the power to drive the receiver system, etc. To prove synchronization, one can compute the Lyapunov exponent for the difference of the outputs $\boldsymbol{u}$ and $\boldsymbol{w}$. When the maximum of this conditional Lyapunov exponent is negative, both signals are moving closer to each other and are eventually going to travel on exactly the same

trajectory[69].

Common Approaches to Prove Chaos Synchronization

Synchronization of chaos in laser systems is increasingly shown since the year 2000. Especially the synchronization of chaos in semiconductor lasers has seen a lot of publications over the years, since it was one of the first systems to be synchronized [70]. The synchronization distance and the chaos bandwidth are both increased. Last year, 2023, the synchronization of semiconductor laser over a distance of 1040 km was shown utilizing fiber relays with hybrid amplification [71].

There are also reports about the synchronization of chip-scale microchip lasers [72]. Uchida et al. showed the synchronization in microchip lasers and proposed a few different schemes to secure data transmission with chaos synchronization.

When validating chaos synchronization, two concepts are usually used, chaos attractors and simply the correlation between both chaotic sources. Chaos attractors can show synchronization when being similar, but in some cases, the chaos attractor analysis might be inconclusive. The most common way to show chaos synchronization is by calculating the cross correlating between both chaotic sources, and a usual minimum threshold value is 90% which is said to be sufficient for chaos secure communication applications. Furthermore, the temporal chaotic waveforms can be plotted with respect to each other, so that the degree of synchronization is not only quantitatively but also qualitatively shown, where a perfect synchronization would mean all data points align perfectly diagonally. While the use of the Lypunov exponent and bifurcation diagram was motivated above, the publications which actually investigate these parameters are scarce.

The most common systems to synchronize laser chaos in, are based on semiconductor laser, microchip lasers, and also on photonic integrated circuits (PIC).

2.4 Chaos Secure Communication

As the demand for high-speed and broadband data transmissions increases and more efficient technologies are developed, great difficulties arise. One of them is the problem of security. Usually, the clear data is encoded by computer software, e.g. the RSA (Rivest–Shamir–Adleman) algorithm, which security is determined by the difficulty of calculations necessary to crack the encoded message. While the RSA algorithm for example is sufficiently secure for today's computer standards, the rapid development in computer technology is said to soon be able to produce machines which are capable of decoding such digitally encoded messages. One could increase the complexity of

the calculations needed for normal encoding and decoding, so that the complexity to decipher the message without the key is also complicated, but this would have a negative impact on real-time data transmission as the time to process the data is increased. In order to make the encoding more complex, quantum communication protocols are being developed, e.g. Quantum key distribution. However, they are still facing a lot of challenges. Another candidate to increase the complexity for the increasing amount of data being transferred is chaotic communication.

2.4.1 Approaches and State of the Art

Chaotic communication techniques can be divided into two kinds, digital and analogue encryption. The digital encryption technique is a software-based encryption technique, but the keys used to encrypt the signals are generated by chaotic sources. When both transmitter and receiver possess a similar chaotic source and are synchronized, so that the generated chaos is the same in both locations, a key can be generated from the chaotic sequence. To make the key more difficult to guess for a third party, further improvements can be made, e.g. by using random bit generators and both sides to randomly modulate the generated chaotic waveforms [73, 74]. The randomly generated bits to modulate the chaos signal can then be sent over the public channel.

On the other hand, analogue techniques present themselves as a method which could possibly achieve higher encryption and decryption speeds, because there is no limiting digital component. The three basic analogue encryption techniques are called chaos masking (CMA), chaos modulation (CMO), and chaos shift keying (CSK), and are explained in the following sections. While each technique can be verified by laser rate equations, these sections will highlight the general idea about each approach.

Chaos Masking

Chaos masking (CMA) is an approach where the clear signal is hidden in the chaotic signal, or rather it is masked. As seen in Fig. 2.14, a chaotic source is generating a signal $x(t)$, in which a message signal $c(t)$ is embedded, by adding the message to the chaotic signal. The encoded signal, $x(t) + c(t)$ is transmitted to the receiver side, where it is injected into a second chaotic source, which is controlled exactly the same parameters as the first chaotic source. By synchronization, the second chaotic source is generating the same chaotic signal as the source on the transmitter side $x(t)$. Simply subtracting the generated signal from the transmitted signal, results in obtaining the sent message $c(t)$. The expression for the transmitted signal clearly shows that there is a constraint for the message in terms of its intensity. Is the message signal too intense, or rather has a higher amplitude than the chaotic signal, the message signal is not hidden in the

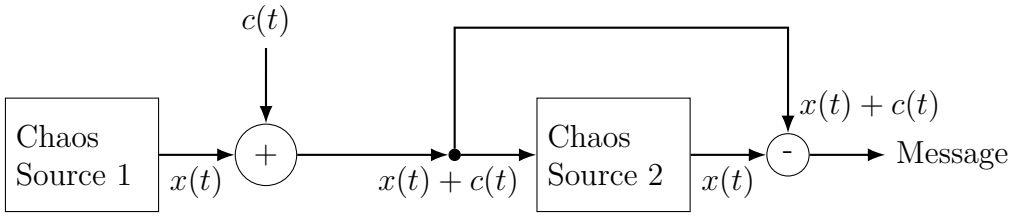

Figure 2.14: General Concept of Chaos Masking

chaos. Therefore, for secure data communication, the power of the message signal is usually chosen to be smaller than 1% of the power of the chaotic signal. To reduce the amount of misidentified bits, the synchronization has to be sufficiently high, where a common minimum threshold is set at a synchronization coefficient, or cross correlation, of at least 90%.

While utilizing the CMA approach for chaos communication is now common, it has not started until after the year 2000, [75]. One of the most famous and most often cited papers regarding CMA, was published by Argyris et al. in Nature, in 2005 [76]. They were able to utilize distributed feedback (DFB) lasers to synchronize chaos and transmit data securely using a CMA scheme at 5 GHz.

Chaos Modulation

Chaos modulation (CMO) might be similar to CMA, but it is different in a way that the message which should be encoded, is used to modulate the chaotic source. So, both the chaotic carrier and the message are forming a new chaotic oscillation. The process is roughly described in the schematic in Fig. 2.15, where the chaotic carriers are produced by nonlinear feedback. When the message $c(t)$ is injected, the chaotic carrier output at that is fed back nonlinearily to the Oscillator, where it gains a delay of τ over the distance of the feedback loop. The new chaotic signal is then given by $x(t+\tau) = f(x(t) + c(t))$, which is together with the message signal $x(t+\tau) + c(t)$ sent to the receiver. Because the receiver chaotic system has the same parameters as the transmitter system, the chaotic source is also generating the chaotic carrier as the transmitter side, $x(t+\tau)$. Hence, this generated chaotic carrier is similarly to the CMA method simply subtracted from the transmitted signal, resulting in the clear message signal. Therefore, when utilizing the CMO method the message signal is not allowed to exceed a certain threshold to make the communication secure.

One of the first proofs of chaos synchronization in laser systems was also accompanied by CMO, [77]. Van Wiggeren and Roy synchronized two erbium-doped fiber lasers, and used a CMO scheme to encrypt, transmit and decrypt a data stream at 126 MBit/s in 1998.

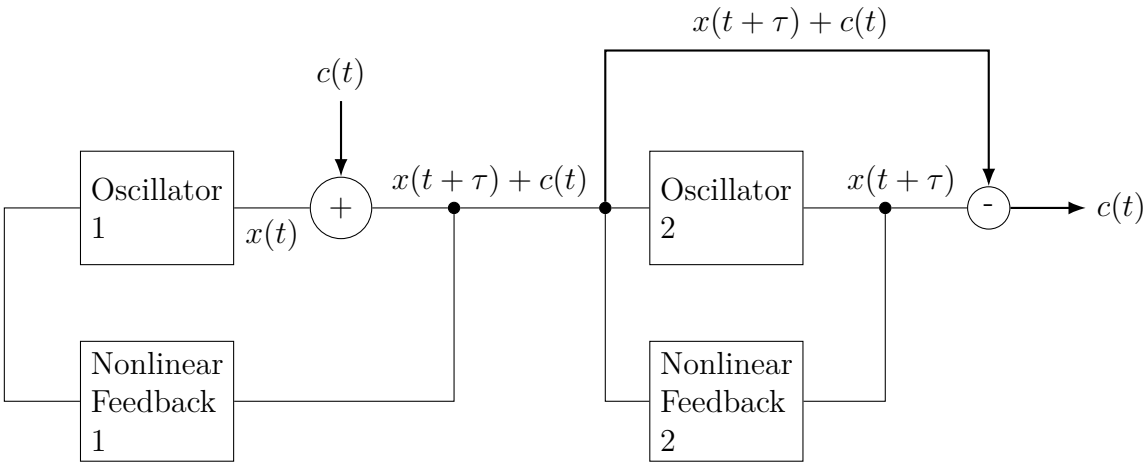

Figure 2.15: General Concept of Chaos Modulation

Chaos Shift Keying

Finally, the third main approach for chaos secure communication is chaos shift keying (CSK). CSK is utilizing multiple chaotic sources on both sides, but by selective switching between the sources, only the signal of one source is sent over to the receiver per time slot. In Fig. 2.16 the general concept of CSK is depicted, with two chaotic sources on each side. The message $c(t)$ is here switching between both available chaotic sources, e.g., a zero bit is translated to switching to the signal $x_1(t)$ and a one bit is translated to switching to the signal $x_2(t)$. Depending on the message, other signals are sent to the receiver. On the receiver side, the sent signal is injected in both chaotic sources, but only one of both is synchronizing with the sent signal, so that the sent signal can be detected. Important with this approach is to take the transient times into account the systems need to synchronize. The bit rate should not be as fast as the reciprocal of the synchronization time, but significantly slower. Furthermore, both chaotic signals $x_1(t)$ and $x_2(t)$ should not differ too much, or it might be possible to analyze the different chaotic attractors and find the two different states.

The CSK scheme does not have to be comprised of two sets of different chaotic sources. It is also possible to employ a method called chaos on-off keying, where the chaotic signal is modulated by an acousto-optic modulator (AOM) with a small modulation depth of even less than 0.2% [78]. In this study they used microchip lasers. Because the degree of synchronization is degraded in presence of external modulation of the chaotic signal, they encoded messages into the signal, by turning the modulation on and off at a rate of 100 kHz.

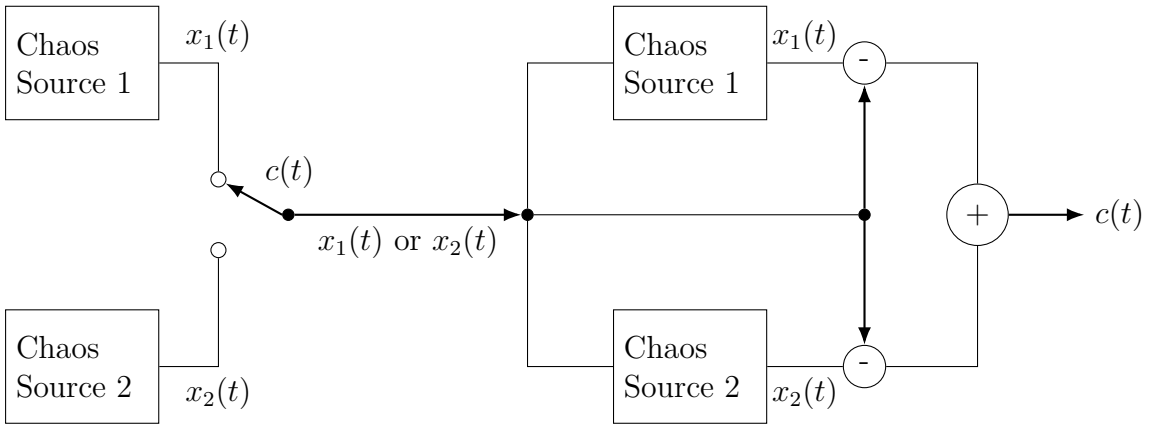

Figure 2.16: General Concept of Chaos Shift Keying

State of the Art

The most common approach to realize chaos secure communication was to employ semiconductor lasers, which are unfortunately limited to about $2.5\,\mathrm{Gbit\,s^{-1}}$. Thus, in 2010, Lavrov et al. were able to prove electro-optic (EO) feedback systems as a viable options for broadband chaos communication [79]. They demonstrated the transmission of $10\,\mathrm{Gbit\,s^{-1}}$ over a distance of more than 100 km, utilizing CMA.

Higher speeds were achieved by Ke et al. in 2018 [80], where they demonstrated a transmission of $30\,\mathrm{Gbit\,s^{-1}}$ over an installed fiber network of a length of 100 km. In their study, they used a duobinary enconding scheme, which enables the transfer of $30\,\mathrm{Gbit\,s^{-1}}$ in a 10 GHz optical channel.

Currently, the highest speeds were demonstrated by Zhao et al. by employing an optical encryption scheme for wavelength division multiplexing (WDM), where they securely transmitted $4 \times 12.5\,\mathrm{Gbit\,s^{-1}}$ over 50 km of single mode fiber [81].

Looking at the synchronization distance, the current record holder are Wang et al. who demonstrated a synchronization of two semiconductor lasers of a transmission line of 1040 km [71]. They used multiple amplification relays, with normal single mode fibers, dispersion compensation fibers and erbium-doped fiber amplifiers (EDFAs).

Moreover, there is a report from last year, showing the chaos synchronization of two lasers over a free-space link [82] Furthermore, they showed the secure transmission of an image over the free-space distance of 10 m by chaos masking.

While all these approach strive to achieve synchronization over longer distances, higher speeds or increase the number of applications, by synchronizing chaos over free-space, there is no report of synchronizing microring resonators in their chaotic state. Microring resonator have the potential to increase the transmission bandwidth, since the spectrum of the MI microcomb is broader than most current optical chaos sources. Furthermore, the small footprint and the possibility to fabricate them with CMOS

processes picture them as an attractive future.

In our group, we were able to show the synchronization of two microring resonators in the simulation [83], using a cascaded setup of two microring resonators. The synchronization has also been proved to be viable when part of the first resonator is filtered, meaning only part of the spectrum is injected into the follower ring [84]. First investigations regarding the encryption of data and the quality of chaos were presented [85].

2.4.2 Proposed Technique

As Zhao et al. already showed the possibility to utilize WDM for chaos secure communication [81], the goal for this study is to utilize the full width of the MI comb as a chaotic carrier. Employing a greater number of different modes of the microresonator, can yield to even greater bandwidth. Upon synchronization of two microresonator systems a number of different chaos encryption methods can be utilized to encrypt and decrypt the data.

Thus, the key for the communication is the synchronization and the parameters which are needed for the synchronization. Here, the assumption which is made and has to be true for a secure communication scheme, is that both microring resonators are not able to synchronize without being regulated by the same parameters. The parameters include for example the pump power, the pump wavelength, the pump power, the temperature of the resonator, and probably parameters, which we have not thought of as parameters yet. Furthermore, both rings have to be the same, produced with the same process, having the same dimensions, dispersion and nonlinear effects. Even when an eavesdropper possesses the same microring, they would have to perfectly guess the parameters used by the legitimate users. In theory, a minuscule parameter change should be enough to disable the synchronizability.

Once synchronization is realized, different methods can be utilized to transmit data, e.g. chaos masking or chaos shift keying, even the generation of random bits and then digitally encrypting and decrypting could be possible, but the focus lies here on analogue techniques. As we have already shown the feasibility to synchronize two microring resonators, by only injecting a part of the comb into the follower resonator [84], this has the power to ease the synchronization. Using a few channels of the MI comb for synchronization, makes the other channels available to transmit data hidden or encrypted with chaos and not being needed on the receiver side to synchronize the follower resonator with the leader resonator.

Considering a simple chaos masking technique, shown in Fig. 2.17, where part of the channels is filtered out and in each filtered channel has a different message hidden

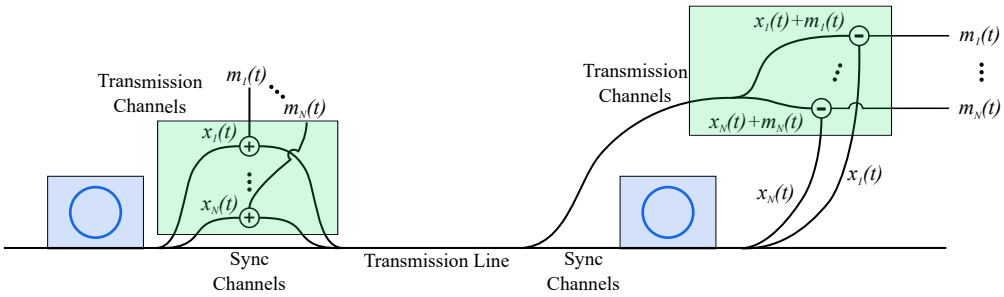

Figure 2.17: Microresonator chaos masking

by chaos masking, define these channels as message channels. The unfiltered channels are left as they are and are called synchronization channels. All channels are put back into one fiber and transmitted to the receiver side. On the receiver side, the message channels are filtered out and the synchronization channels are injected into the follower resonator. The follower resonator is now synchronizing with the leader resonator, imitating the channels which were filtered out. At the output of the follower ring, each channel is again filtered out one by one, and compared to the corresponding message channels which were sent by the transmitter. By subtracting the generated signal on the receiver side from the message signals, the message can be reconstructed for all the different message channels at the same time.

A similar concept could be realized with chaos shift keying, presuming our assumption is correct, that only minuscule changes in the parameters regulating the resonators is already disabling the synchronizability. With this two slightly different powered microresonators could be used on each side again with transmission channels and message channels. The transmission channels are solely there to keep both microresonator pairs synchronized. The message channels are slightly different, so that the same channels on each side are not correlated with each other, but only with the corresponding microresonator on the other side. Therefore, the same message channels are filtered out on one side, where the chaos shift keying technique is applied to that channel pair, so that each outgoing mode on the transmitter side is comprised either of the the modes signal from the first resonator or from the second resonator on the transmitter side. On the receiver side, each mode is compared with the corresponding mode in both resonators. By determining the correlation between the sent signal and the generated signal on the receiver side, it can be also determined, whether in that time slot the mode of the first or the second resonator on the transmitter side was used. But the chaos shift keying method could be much harder to implement.

3 Simulation

Before moving to an experiment, the simulation of two cascaded microring resonators and their synchronization is essential. First, the methodology is introduced, where the the concept of the simulation is presented. The simulated rings will be synchronized and analyzed on its own using different techniques. The results of that with a following discussion are provided upon the introduction to the setup.

3.1 Methodology

Simulations and further calculations are done in the latest release of MATLAB, 2022b, as of end of 2022. Utilizing the previously reviewed coupled-mode theory, Chap. 2 2.2.1, the equations are adjusted to fit the model, which is shown in the first section. To simulate the equations, the analytical forms have to be brought into numerically computable forms, which are here the Lugiato-Lefever-Equations (LLEs). Furthermore, different approaches to analysis the chaos in this thesis are presented.

3.1.1 Concept

The simulation process is split into two stages, depicted in Fig. 3.1. The first stage is to generate MI combs in each resonator on its own, and then if both MI combs are generated, in the second stage, the output of the first resonator is injected into the second one, letting both cavities synchronize. The synchronization process is controlled by the variable attenuators. Moreover, a stop-band filter can be inserted between leader and follower to filter parts of the comb out as shown in Chap. 2.3 by Moreno et al (our group) [84].

The general idea of this concept can be seen in Fig. 3.2. Both rings are driven by their own pump laser, A_{pump_1} and A_{pump_2}, with the respective pump frequencies ω_{pump_1}

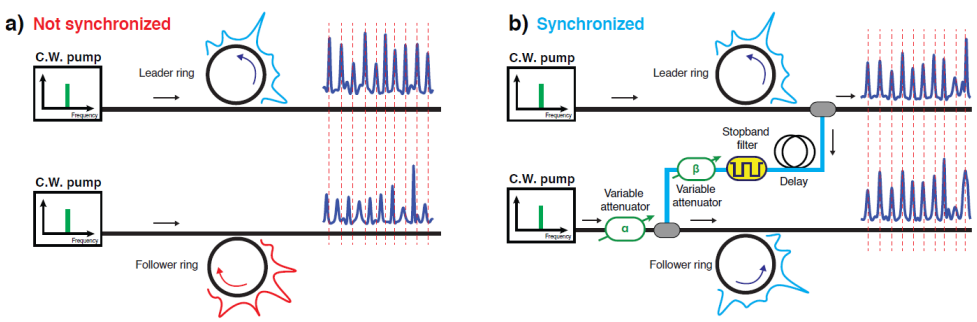

Figure 3.1: Concept of Simulation Stages from [84]

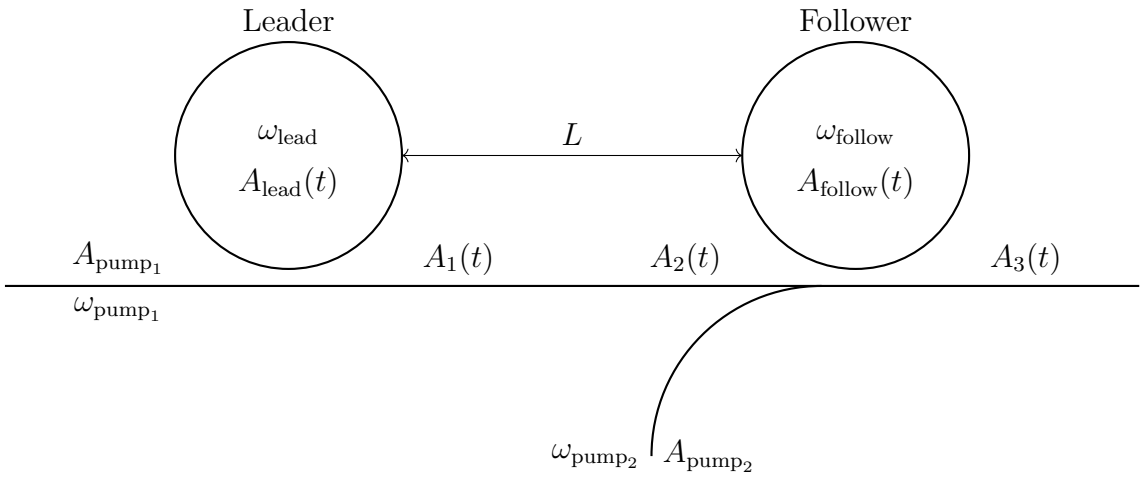

Figure 3.2: Concept of Two Cascaded Microrings

and ω_{pump_2}. Furthermore, let the resonance frequency inside the resonators be ω_{lead} and ω_{follow}, with the intracavity fields, $A_{\text{lead}}(t)$ and $A_{\text{follow}}(t)$, for leader and follower, respectively. The output of the first ring is denoted by $A_1(t)$ which transforms over the length L between the resonators to the input of the follower resonator, $A_2(t)$. Finally, the output of the follower is given by $A_3(t)$.

In a similar fashion to Chap. 2 2.2.1, the field equations are derived. Consider the leader cavity $A_{\text{lead}}(t)$, when the pump laser A_{pump_1} is active:

$$\frac{\mathrm{d}A_{\text{lead}}(t)}{\mathrm{d}t} = -\left(\frac{1}{2\tau_{\text{lead}}} + i\omega_{\text{lead}}\right) A_{\text{lead}}(t) + \frac{1}{\sqrt{\tau_{\text{coup}}}} A_{\text{pump}_1}(t) \exp(-i\omega_{\text{pump}_1} t) \tag{3.1}$$

Instead of using the reciprocal of the coupling decay, utilizing the coupling rate, κ_{coup}, directly simplifies the equation. The attenuation rate changes to $\tau_{\text{lead}}^{-1} = \tau_{\text{int}}^{-1} + \kappa_{\text{coup}}$. Moreover, the optical field inside the cavity is transformed to

$$\overline{A}_{\text{lead}}(t) = A_{\text{lead}}(t) \exp(\mathrm{i}\omega_{\text{pump}_1} t), \tag{3.2}$$

so that the overall time variation of the cavity is given by:

$$\frac{\mathrm{d}\overline{A}_{\text{lead}}(t)}{\mathrm{d}t} = \left(i(\omega_{\text{pump}_1} - \omega_{\text{lead}}) - \frac{1}{2\tau_{\text{lead}}}\right) \overline{A}_{\text{lead}}(t) + \sqrt{\kappa_{\text{coup}_1}} A_{\text{pump}_1}(t) \tag{3.3}$$

Defining the beating, or rather the detuning, between leader and first pump laser:

$$\delta_1 = \omega_{\text{pump}_1} - \omega_{\text{lead}}, \tag{3.4}$$

makes the previous equation more readable, which results in

$$\frac{\mathrm{d}\overline{A}_{\mathrm{lead}}(t)}{\mathrm{d}t} = \left(i\delta_1 - \frac{1}{2\tau_{\mathrm{lead}}}\right)\overline{A}_{\mathrm{lead}}(t) + \sqrt{\kappa_{\mathrm{coup}_1}}A_{\mathrm{pump}_1}(t). \tag{3.5}$$

Similarly, when the ring is only driven by the pump laser and nothing else, the differential equation for the follower ring can be expressed as:

$$\frac{\mathrm{d}\overline{A}_{\mathrm{follower}}(t)}{\mathrm{d}t} = \left(i\delta_2 - \frac{1}{2\tau_{\mathrm{follow}}}\right)\overline{A}_{\mathrm{follow}}(t) + \sqrt{\kappa_{\mathrm{coup}_2}}A_{\mathrm{pump}_2}(t), \tag{3.6}$$

where all the variables are defined in a similar fashion as before. Having both resonators connected to a pump laser and being able to generate MI combs in both, sets the stone for the next step, connecting both cavities.

When the output of the first ring travels over the distance L until it is coupled into the second ring, the phase and the amplitude is prone to change. Consider the complex propagation constant in the fiber $\underline{k} = k_r + \mathrm{i}k_i$, and the incoming optical field at the second resonator is given by:

$$A_2(t) = \exp(-\mathrm{i}kL)A_1(t). \tag{3.7}$$

To determine the output of the leader cavity Eq. 2.31 is used, so that $A_1(t)$ and $A_2(t)$ can be written in terms of the pump laser and the transformed intracavity field of the first ring, A_{pump_1} and $\overline{A}_{\mathrm{lead}}(t)$:

$$A_1(t) = \sqrt{\kappa_{\mathrm{coup}_1}}\overline{A}_{\mathrm{lead}}(t) - A_{\mathrm{pump}_1}(t) \tag{3.8}$$

$$A_2(t) = \exp(-\mathrm{i}kL)\left(\sqrt{\kappa_{\mathrm{coup}_1}}\overline{A}_{\mathrm{lead}}(t) - A_{\mathrm{pump}_1}(t)\right) \tag{3.9}$$

The output field from the first cavity, $A_2(t)$, can be added to Eq. 3.6, so that:

$$\begin{aligned}\frac{\mathrm{d}\overline{A}_{\mathrm{follow}}(t)}{\mathrm{d}t} &= \left(\mathrm{i}\delta_2 - \frac{1}{2\tau_{\mathrm{follow}}}\right)\overline{A}_{\mathrm{follow}}(t) + \sqrt{\kappa_{\mathrm{coup}_2}}A_{\mathrm{pump}_2}(t) + \dots \\ &\quad \sqrt{\kappa_{\mathrm{coup}_2}}\exp(\mathrm{i}(\omega_{\mathrm{pump}_2} - \omega_{\mathrm{leader}}))A_2(t) \qquad (3.10) \\ &= \left(i\delta_2 - \frac{1}{2\tau_{\mathrm{follow}}}\right)\overline{A}_{\mathrm{follow}}(t) + \sqrt{\kappa_{\mathrm{coup}_2}}A_{\mathrm{pump}_2}(t) + \dots \\ &\quad \sqrt{\kappa_{\mathrm{coup}_2}}\exp(\mathrm{i}(\omega_{\mathrm{pump}_2} - \omega_{\mathrm{lead}}))A_1(t)\exp(-\mathrm{i}kL) \qquad (3.11)\end{aligned}$$

Since the output field $A_1(t)$ is oscillating with the frequency ω_{lead}, a beating between this frequency the second pump laser can be seen, $(\omega_{\mathrm{pump}_2} - \omega_{\mathrm{leader}})$. Furthermore, the

output field of the second cavity can be defined as:

$$A_3(t) = \sqrt{\kappa_{\text{coup}_2}}\overline{A}_{\text{follow}}(t) - A_1(t)\exp(-\mathrm{i}kL) - A_{\text{pump}_2}(t) \tag{3.12}$$

3.1.2 Lugiato-Lefever Equations

Lugiato and Lefever derived with their equations a way to describe light propagation in non-linear optical resonators [86]. The Lugiato-Lefever Equations (LLEs) were first introduced as a equation that is independent of the longitudinal variable z, which could be given by:

$$\frac{\partial E}{\partial \overline{t}} = E_{\text{in}} - E - i\theta E + i\nabla_{\perp}^2 E + i|E|^2 E, \tag{3.13}$$

and the transverse Laplacian operator,

$$\nabla_{\perp}^2 = \frac{\partial^2}{\partial \overline{x}^2} + \frac{\partial^2}{\partial \overline{y}^2}, \tag{3.14}$$

where $\overline{t}$, $\overline{x}$ and $\overline{y}$ are normalized variables for time and space. They are normalized as $\overline{t} = \kappa t$, $\overline{x} = \frac{x}{l_{\text{d}}}$ and $\overline{y} = \frac{y}{l_{\text{d}}}$, where κ is the cavity decay rate and l_{d} the diffraction length. Furthermore, the cavity detuning is given by $\theta = (\omega_r - \omega_0)/\kappa$, where ω_r is the closest frequency of the resonator to ω_0. On the RHS of Eq. 3.13, each addend has its physical meaning. E_{in} is the normalized amplitude of the input field, the second addend is the decay term, the third one is the detuning term, then there is the transverse Laplacian which expresses the diffraction, finally there is the cubic nonlinear term that describes the Kerr effect.

A few years later the longitudinal LLE was formulated [87, 88]. It is independent of the transverse variables, namely the coordinates x and y, and only dependent on the longitudinal variable z.

$$\frac{\partial E}{\partial \overline{t}} = E_{\text{in}} - E - i\theta E + i\frac{\partial^2 E}{\partial \overline{z}^2} + i|E|^2 E, \tag{3.15}$$

where $\overline{z}$ is normalized by $\overline{z} = z/a$ and a depends on the second order dispersion of the medium. In contrast to the transverse LLE, the longitudinal LLE changes diffraction to dispersion, which is beneficial for microring resonators. Therefore, the longitudinal LLE is used to describe the behavior in the cascaded microresonators.

The here used LLE is a generalized variant, which derivation is quickly reviewed [89]. Consider a typical ring-resonator waveguide configuration, similar to Fig. 2.4 in Chap. 2.2.1, where the resonator is pumped by a continuous-wave laser with a driving field E_{in}. Power is coherently added to the optical field propagating inside the resonator, through a coupler with coupling coefficient κ. To describe this process mathematically,

the coupling region can be investigated during the transition of two round-trips.

$$E^{m+1}(0,\tau) = \sqrt{\kappa}E_{\text{in}} + \sqrt{1-\kappa}e^{(m)}(L,\tau)\mathrm{e}^{\mathrm{i}\phi_0}, \tag{3.16}$$

where L is the round-trip length, τ the time, and ϕ_0 the accumulated phase of the intracavity field over one round trip.

With the assumption that light propagates in a single spatial mode, the temporal evolution can by described by the nonlinear Schrödinger (NLS) equation.

$$\frac{\partial E(z,\tau)}{\partial z} = -\frac{\alpha_i}{2}E + \mathrm{i}\sum_{k\geq 2}\frac{\beta_k}{k!}\left(\frac{\partial}{\partial\tau}\right)^k E + \mathrm{i}\gamma|E|^2E. \tag{3.17}$$

α_i is the linear absorption coefficient inside the resonator, the dispersion coefficients as a Taylor series expansion are $\beta_k = \mathrm{d}^k\beta/\mathrm{d}\omega^k|_{\omega=\omega_0}$. And $\gamma = n_2\omega_0/(cA_{\text{eff}})$ is the nonlinearity coefficient, where n_2 is the nonlinear refractive index and A_{eff} is the effective area of the resonator.

Eg. 3.16 and Eq. 3.17 can be averaged and merged together, so that an externally driven NLS, or rather the generalized LLE, is revealed,

$$t_R\frac{\partial E(t,\tau)}{\partial t} = \left[-\alpha - \mathrm{i}\delta_0 + \mathrm{i}L\sum_{k\geq 2}\frac{\beta_k}{k!}\left(\mathrm{i}\frac{\partial}{\partial\tau}\right)^k + \mathrm{i}\gamma L|E|^2E\right] + \sqrt{\kappa}E_{\text{in}}, \tag{3.18}$$

where t_R is the round-trip time, α denotes the total cavity losses as $\alpha = (\alpha_i + \kappa)/2$, and δ_0 is the detuning between the l'th orders cavity resonance and ϕ_0, $\delta_0 = 2\pi - \phi_0$. Furthermore, there is t, a continuous variable, which measures the *slow time* of the cavity. It can also be expressed in from of round-trips:

$$E(t = mt_R, \tau) = E^{(m)}(0,\tau). \tag{3.19}$$

Application to model

While Fig. 3.2 showed the coupled-mode equations for the simple case of two resonators, without any possibility to set different parameters, this functionality is included in the actual concept, as seen in Fig. 3.3. In this model, the names for the optical fields are changed to increase readability, and attenuator are added. Utilizing α_{pump} and β_{inj}, the amplitude of the pump for the follower ring and the amplitude of the leader's output can be adjusted, so that the synchronization between both output signals of the cavities can be optimized. Synchronization is calculated by taking the cross-correlation coefficient between leader output and follower output, which will explained after the LLEs for the simulation concept have been presented.

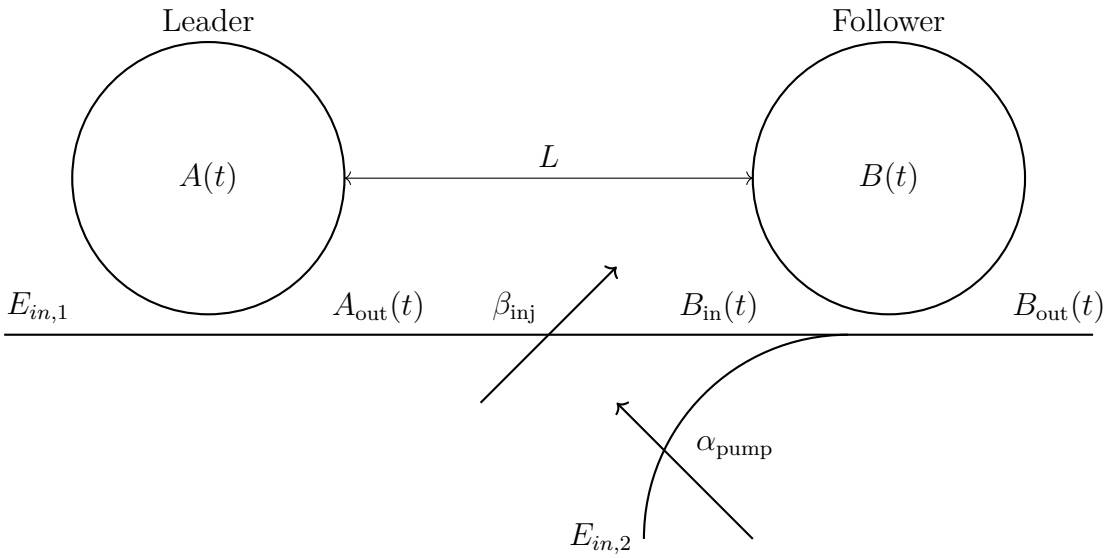

Figure 3.3: Concept of Cascading two microresonators with additional parameters

Following the example of the generalized LLE, the values for the setup on hand can be inserted into the equations. Starting with the leader ring, $A(t)$, the LLE is directly given by,

$$t_R \frac{\partial A}{\partial t} = \left(-\frac{\alpha_i L + \kappa}{2} - \mathrm{i}\delta_0 + \frac{\mathrm{i}L}{2}\beta_2 \frac{\partial^2}{\partial \tau^2} + \mathrm{i}\gamma L |A|^2 \right) A + \sqrt{\kappa} E_{\mathrm{in},1}, \tag{3.20}$$

where the variables are similar to Eq. 3.18. The only difference can be found in the dispersion term, since all higher-order dispersion coefficients are neglected and only the second-order term is taken into account. As motivated in the theory part 2.2.1, the higher-order dispersion coefficients are exponentially shrinking, third-order coefficients and above have a marginal effect on the dispersion, so that they can be neglected.

Since the follower cavity shall be controlled by the leader's output, that output has to be defined. The output of the leader in terms of input field and intracavity field is given as:

$$A_{\mathrm{out}} = E_{\mathrm{in},1} - \sqrt{\kappa} A \tag{3.21}$$

This output travels the distance L between leader and follower, where its amplitude and phase are changing due to the complex wave propagation constant $\underline{k} = k_r + \mathrm{i}k_i$, but in the current simulation results the complex part is set to zero. Nevertheless, for the input into the second cavity holds the following equation:

$$B_{\mathrm{in}} = \beta_{\mathrm{inj}} A_{\mathrm{out}} \exp(-\mathrm{i}\underline{k} L), \tag{3.22}$$

where β_{inj} the attenuation factor is from the variable attenuator. To simulate the chaos synchronization between distant systems, an additional noise component can be added

to the input field of the follower resonator:

$$B_{\text{in}} = \beta_{\text{inj}}(A_{\text{out}} \exp(-\mathrm{i}\underline{k}L) + A_{\text{noise}}), \tag{3.23}$$

where A_{noise} is the additionally added noise.

Moving to the second cavity, the difference compared to the leader cavity is the number of inputs. Next to the attenuated pump for the follower ring, also the attenuated output of the leader cavity is coupled into the follower cavity. This simple weighted addition is visible in the next equation for the follower ring:

$$\begin{aligned} t_R \frac{\partial B}{\partial t} = &\left(-\frac{\alpha_i L + \kappa}{2} - \mathrm{i}\delta_0 + \frac{\mathrm{i}L}{2}\beta_2 \frac{\partial^2}{\partial \tau^2} + \mathrm{i}\gamma L |B|^2 \right) B + \dots \\ &\sqrt{\kappa}[\beta_{\text{inj}} A_{\text{out}} \exp(-\mathrm{i}\underline{k}L) + \alpha_{\text{pump}} E_{\text{in},2}]. \end{aligned} \tag{3.24}$$

Finally, the output of the follower ring, can by defined as:

$$B_{\text{out}} = \beta_{\text{inj}} A_{\text{out}} \exp(-\mathrm{i}\underline{k}L) + \alpha_{\text{pump}} E_{\text{in},2} - \sqrt{\kappa} B \tag{3.25}$$

To analyse the degree of synchronization the correlation between both outputs, A_{out} and B_{out} is calculated. But as it stands out, in the output signal of the follower cavity is still a small portion of the output from the leader resonator, which will lead to a correlation between both cavities at any time when they are connected vie the transmission line. Their correlation is always present, even if it is just a small percentage. Luckily, in the simulation the intracavity instantaneous fields can be calculated, which can proof synchronization. However, in the experiment this problem might occur, that the signal from the first cavity is just passing the second cavity without coupling into it.

3.1.3 Chaos Analysis

To make sure the chaos is chaotic enough for securing communication, meaning there is no periodicity in the signal, different approaches to analyze the chaos are explored in this section. As in the theory chapter investigated, there are different ways to characterize chaos. One of the most vivid representations of chaos is plotting the strange attractor. To achieve a accurate strange attractor of a chaotic system one has to setup the coupled chaotic differential equations. However, there are also ways to visualize a chaotic signal in an attractor portrait without having the differential equations but only measured data. Plotting one-dimensional data to visualize it in a possible attractor portrait, one plots the measured data points against the same data points but shifted by a ΔT, so that one data point is paired up with another one

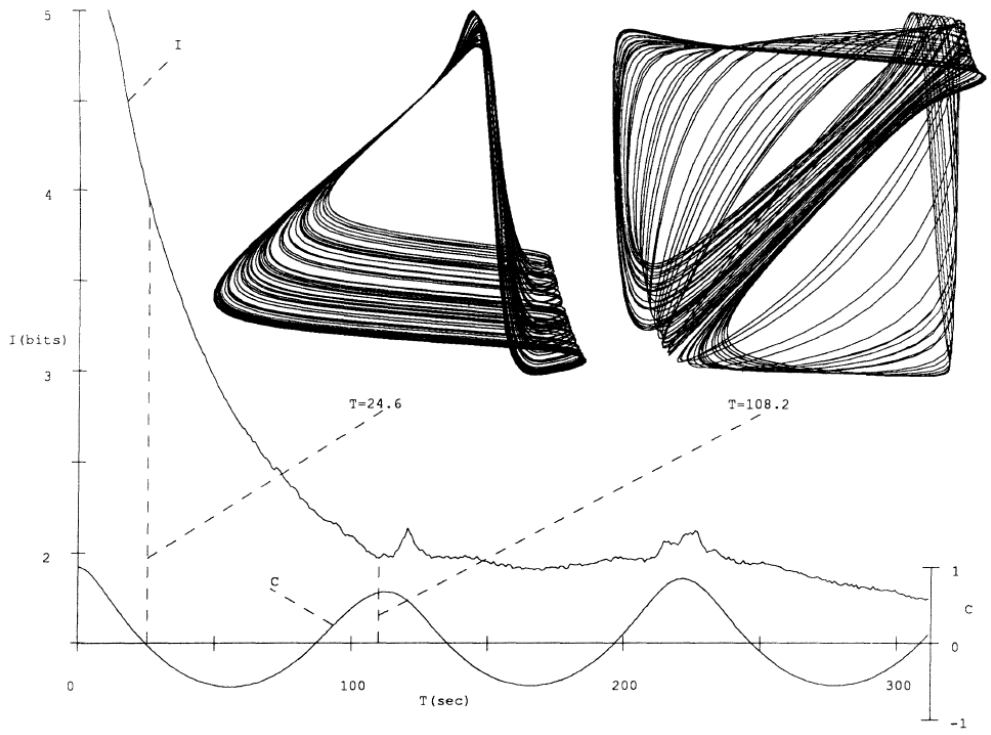

Figure 3.4: Mutual Information(I) and Autocorrelation(C) with Strange attractors [90]

that was measured ΔT later. This can already result in visible attractors or a vivid confirmation on, whether the system is periodic, quasi-periodic, or chaotic. But, there is a way to optimize finding a value for ΔT, that was found out by Fraser et al in 1986 [90]. They showed in their paper, how the attractor portrait is changing for different ΔT. In Fig. 3.4, the same dataset shows two completely different attractor portraits for different approaches to determine the optimal ΔT. A common way was to look at the autocorrelation function of the dataset and find the first zero-crossing. When using the same Δt for the strange attractor, the strange attractor is constructed by linearly independent coordinates. On the other, when they calculated the mutual information, after assuming a histogram distribution to use for calculating the information content with respect to the time delay. When constructing the strange attractor with the time delay of the first minimum of the mutual information table, they found out that the strange attractor is generally more linearly independent.

Let X and Y be two random variables. To review the information content per time delay, each time the signal is shifted, joint 2D histograms are constructed, the joint possibility distribution, $P_{X,Y}(x, y)$. Using the joint probability, the marginal probabilities can be calculated, which are given as $P_X(x)$ and $P_Y(y)$, respectively. The

mutual information is given as:

$$I(X;Y) = \int\int P_{X,Y}(x,y) \log_2 \left(\frac{P_{X,Y}(x,y)}{P_X(x) P_Y(y)} \right) \mathrm{d}x \, \mathrm{d}y \tag{3.26}$$

But since measured values are not continuous, the discrete form of the mutual information function is needed in this case, which is given by:

$$I_{\text{discrete}}(X;Y) = \sum_{x^k \in X} \sum_{y^k \in Y} P_{X,Y}(x^k, y^k) \log_2 \left(\frac{P_{X,Y}(x^k, y^k)}{P_X(x^k) \cdot P_Y(y^k))} \right). \tag{3.27}$$

Furthermore, the bifurcation diagram can be constructed, which is, e.g. simply done by recording 100 local maxima or minima for one detuning step of the cavity. The maxima or minima are then displayed with respect to detuning, which results in a bifurcation diagram.

3.2 Results

To realize the previously defined model in a MATLAB simulation the Lugiato-Lefever equations are used with the parameters shown in Tab. 3.1. The FSR with its corresponding cavity length L, and the high Q-factor match available resonators. The coupling factor κ is chosen in a way that the waveguides and microresonators are critically coupled. The pump power is held constant during the simulation, but the parameter $\alpha_{\text{pump},2}$ can be changed, so that only part of the initial pump power is injected into the second microresonator. To generate the MI microcombs, the pump wavelength is increased by 5 am per iteration.

Parameter	Value
FSR	200 GHz
Cavity length L	757.1 µm
Intrinsic Quality factor Q_i	2×10^6
Coupling factor κ	0.003
Second-order dispersion β_2	$100\,\mathrm{ps^2\,km^{-1}}$
Nonlinear coefficient γ	$0.645\,\mathrm{W^{-1}\,m^{-1}}$
Pump power $\lvert E^2_{\text{in},1}\rvert = \lvert E^2_{\text{in},2}\rvert$	85 mW
Pump wavelength	1558 µm

Table 3.1: Simulation parameters

This result section is divided into four parts. First, only a single ring is considered, where its chaotic attractor is analysed, to compare it with the experimental results later. Then, the MI comb generation in two microresonators is investigated, following

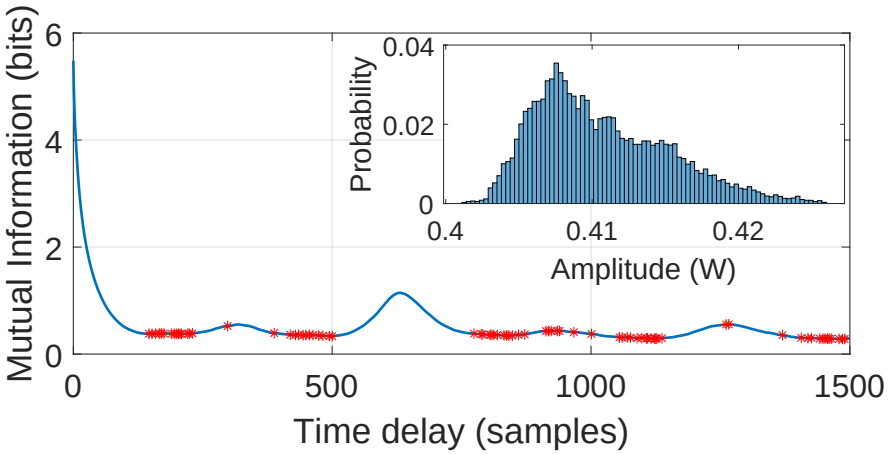

Figure 3.5: Optimization by mutual information technique [90]

the synchronization of both in the optimum case. Finally, parameters like β_{inj} or $\alpha_{\text{pump},2}$ are changed and additional noise in the transmission channel is introduced, to investigate their influence on the synchronization.

3.2.1 Single Ring Analysis

In this part the chaos attractor will be shown based on the mutual information, according to the technique by Fraser et al. [90]. In order to do this, the mutual information depending on a time delay has to be calculated. The calculated mutual information function with respect to the time delay is depicted in Fig. 3.5. Each sample corresponds to a time duration of the reciprocal of the repetition frequency, namely the round trip time of 5 ps. The inset shows the amplitude distribution of the recorded signal, which is averaged per round trip and has therefore a relatively small deviation. In total 100000 round trips were recorded, averaged per round trip, sorted into bins to generate a histogram, which is then used to determine the mutual information function. In the mutual information function, the first minimum, namely the point where the signal is shifted to a point were the original signal and shifted signal have the smallest association with each other, is located at 146 round trips, which equals to 0.73 ns.

Employing the found delay of smallest mutual information as the delay for plotting chaos attractors, these portraits are printed in Fig. 3.6, where a 2D and a 3D diagram are explored. While not as neat and pretty as the chaos attractors known from the Lorenz attractor or the Rössler attractor, a chaotic attractor can be found. In the 2D version, Fig. 3.6a, the trajectories are shown and how they are following a ring-like way around a diagonal line. If the recorded data would belong to a periodic system, a clean ring should be visible. And if it was complete random time series, no attractor can be seen, because true randomness, would result in a cloud of random points. Thus, this attractor is validating the presence of a quasi-random, or chaotic,

times series. Similarly, same conclusions can be drawn from the 3D version of the attractor portrait, in Fig. 3.6b. In comparison to the 2D version, more hints about the attractor are visible. The view-angle is slightly changed, so that a tube-like with variable circumference can be seen.

Important to note, these results are only approximations, as the chaotic differential equations have not been derived.

3.2.2 Dual MI Comb Generation

After proving the presence of chaos using the attractor portraits, this section dedicates itself to the generation of two MI combs at the same time. In order to synchronize two microrings in the end, first two MI combs in said microrings should be generated, before the leader comb is injected into the follower comb. Fig. 3.7 shows the generation of the MI combs in each resonator, the leader comb is plotted in blue and the follower comb in red. The two graphs on the left show the average power in the cavity with respect to the normalized detuning. The two graphs in the middle show the effective detuning with respect to the normalized detuning. The difference between the effective detuning and the normalized detuning is that the effective detuning is also taking the resonance shift due to the kerr nonlinearity into account.

As the wavelength is increased the effective detuning is decreased and the pump wavelength is approaching the effective resonance wavelength. And as the pump wavelength is approaching the effective resonance wavelength, the Turing pattern of the microcomb changes into an MI comb, which is visible in the graphs on the left, because the the average power is changing chaotically. The power is continuously increasing as the pump wavelength approaches the effective resonance wavelength, and the strongly oscillating power shows the chaotic regime of the resonator. On the right, both combs can be seen as they look like in the end of the MI comb generation.

To investigate the generated MI combs, consider the temporal waveforms in Fig. 3.8. The two graphs on the left show the temporal waveforms for the same calculated round trip each, where the intracavity power is shown over the round trip period of 5 ps. As they seem not correlated when looking at it, the correlation is indeed very low at around 6.44%. A more vivid way of comparing both temporal waveforms might be the direct comparison between follower and leader fields. The right side shows the square-root of the power in the follower ring directly compared with the square-root of the power in the leader ring. Each data point corresponds to the same time sample, and if a perfect correlation would be present, these data points would align on a diagonal line. However, as expected, the data points are distributed over the whole range, but with more values being low than high.

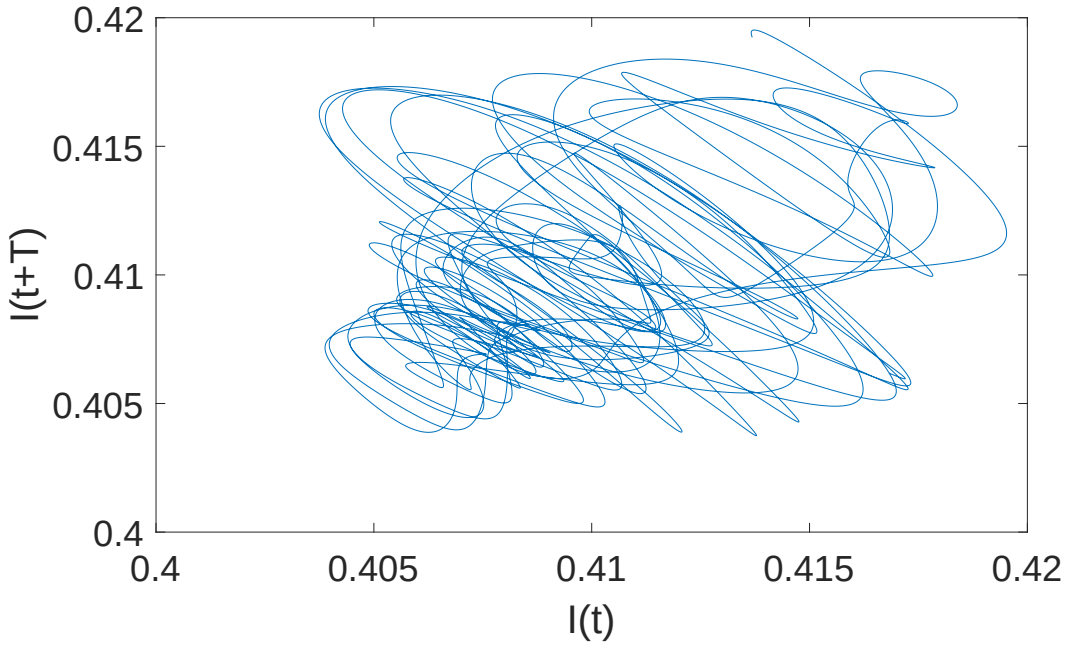

(a) 2D

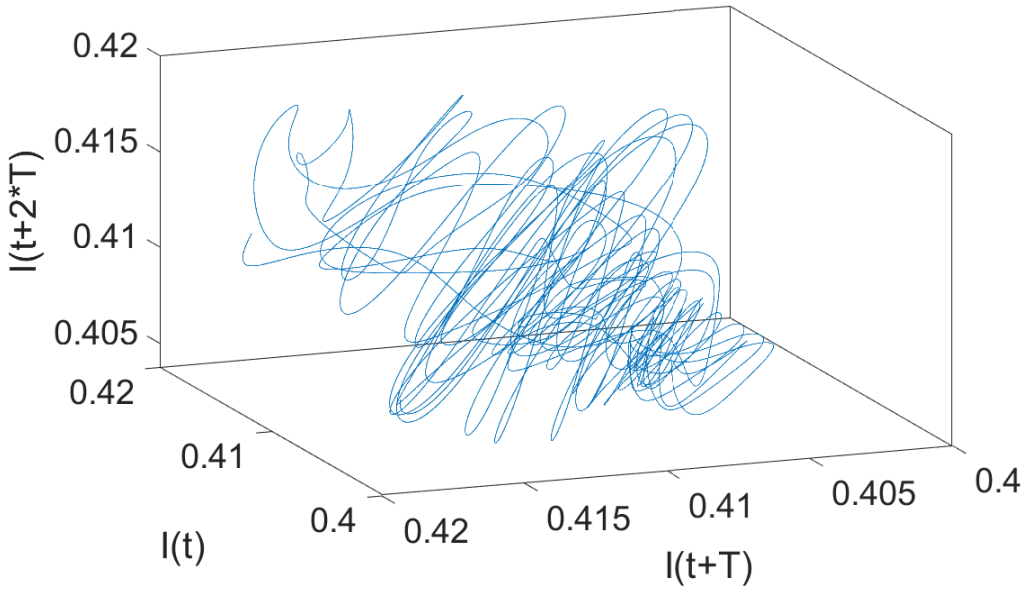

(b) 3D

Figure 3.6: With optimized $\Delta T = 0.73\,\text{ns}$

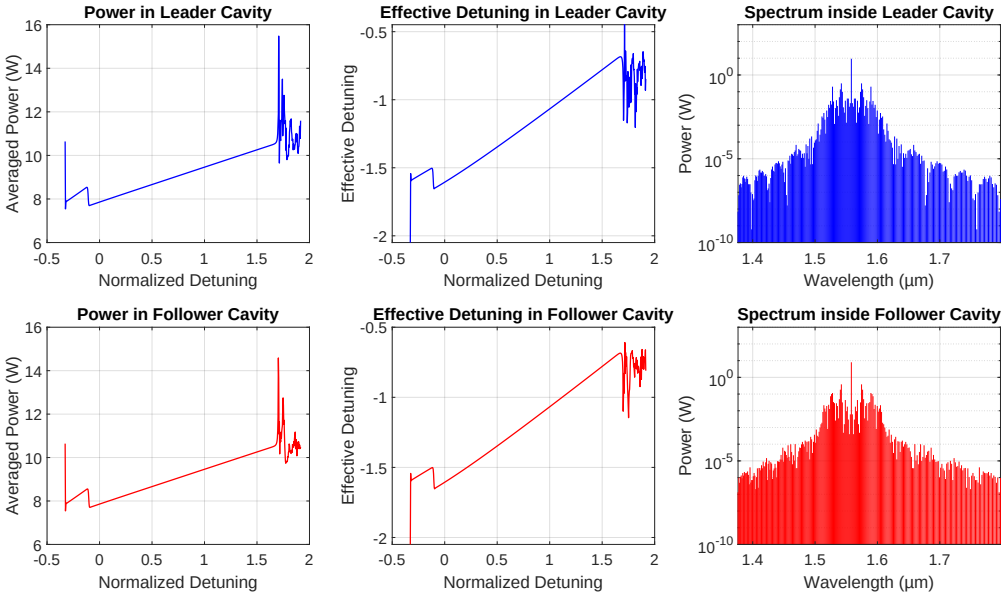

Figure 3.7: Generation of the MI combs in each resonator

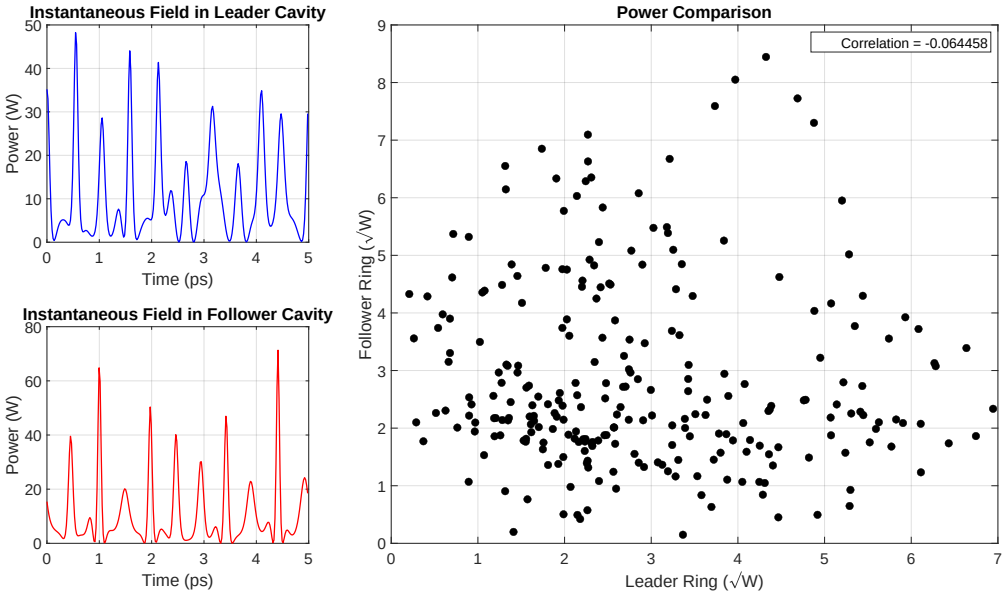

Figure 3.8: Temporal Waveforms of the different resonators

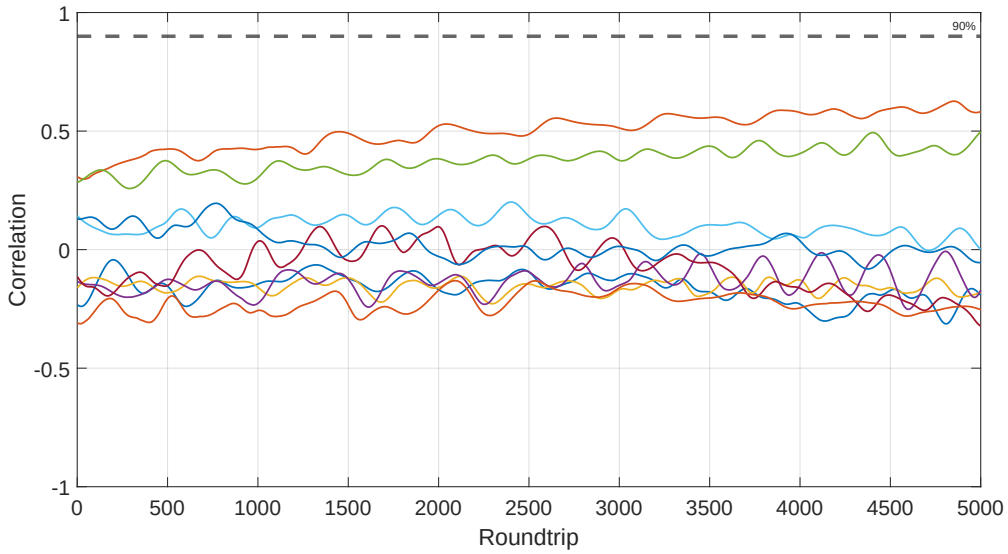

Figure 3.9: Correlation between both resonators for 9 different runs, with the same starting parameters, where the resonators were left unconnected after comb generation

The arising question is whether the correlation between both unconnected cavities changes over time, when simulating both over the period of 5000 round trips or not. Fig. 3.9 visualizes the correlation evolution of both cavities, simulations with the same settings are repeated multiple times. The y-axis shows the cross correlation between both rings per simulated round trip, shown on the x-axis. Parameters as the pump wavelength and pump power are all fixed during the simulation, the only changing parameter is the noise in the temporal waveform of the pump laser in each round trip. Since the injection coefficient between them is $\beta_{\text{inj}} = 0$, so in the real world they should be completely uncorrelated.

However, since the simulation is rather visualizing an ideal case, where no other effects influence the waveforms, the cross correlation does not seem to change over time. In the beginning of the simulation each waveform seems to be set on one form, which does not change much over time. Thus, the correlation between both cavities does not appear to change over time. When averaging over all different runs, over the whole time of 5000 round trips, the cross correlation should approach zero with an increasing number of simulation runs.

After generating MI combs in two different unconnected microresonators and determining the cross correlation between them, shows that while there is no sign of synchronization, their cross correlation also does not change much.

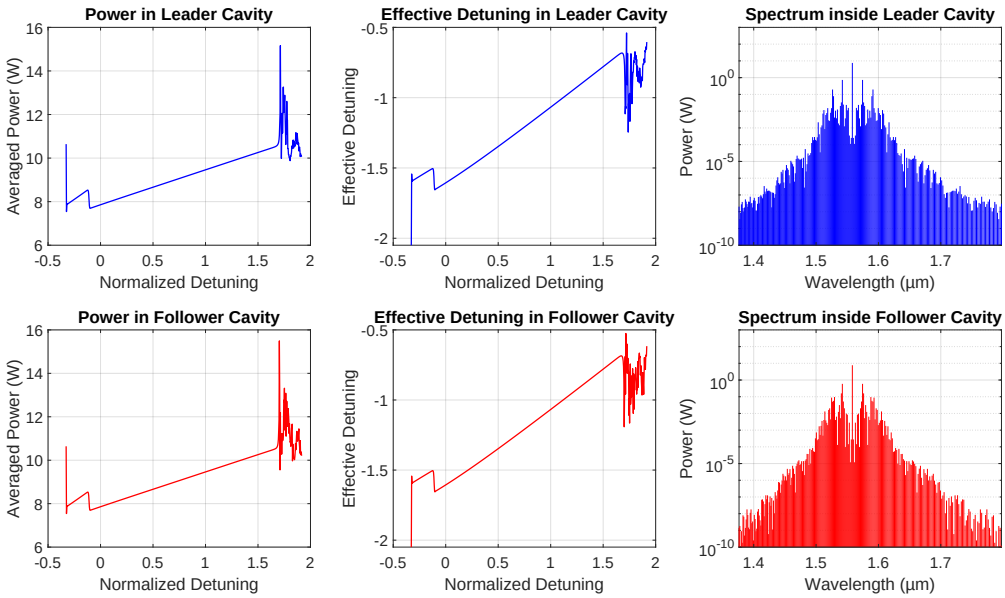

Figure 3.10: Generation of the MI combs in each resonator

3.2.3 Synchronization of Two MI combs

The next step is to analyze the synchronization of two MI combs. First, similarly to the previous case, the MI combs are generated in both resonators. Results of this generation are shown in Fig. 3.10. Again, the blue plots show the leader cavity and the red plots the follower cavity. On the left, both plots show the average power per round trip in each cavity with respect to the normalized detuning. The process of generating the MI combs is completed when the pump wavelength moved to longer wavelengths until the normalized detuning reaches 1.9. In the figures in the middle, the corresponding effective detuning is presented, and evaluates to around -0.6 when both MI combs are generated. This means, that both combs are blue detuned. On the right side, the respective frequency spectra are depicted.

After the generation of both MI combs, both resonators are cascaded. To cascade it is important to set the correct parameters, between the leader and follower resonator, β_{inj}, and between the second pump and the follower resonator α_{alpha_2}. The used parameters are shown in Tab. 3.2.

Parameter	α_{alpha_2}	β_{inj}
Value	0.03	0.55

Table 3.2: Synchronization Parameter

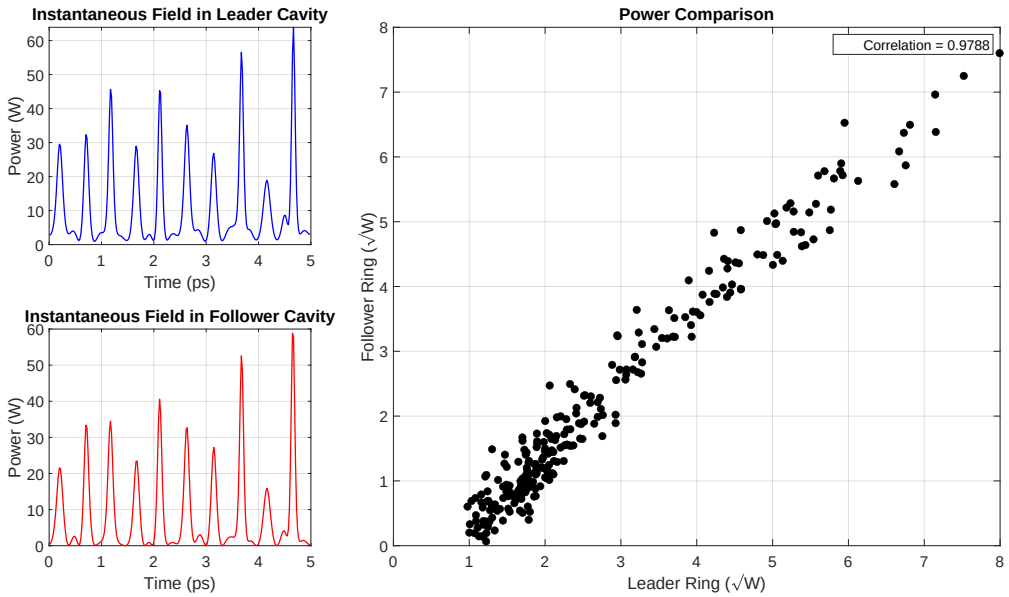

Figure 3.11: Temporal Waveforms of the different resonators

Utilizing these parameters, the output of the leader cavity is injected into the follower cavity, and 5000 round trips are calculated. At the end of these calculations the correlation between both fields inside the cavities is determined. An example is shown again in Fig. 3.11. On the left, the leaders and followers temporal waveforms for one round trip are shown. Comparing them with the bare eye, one notices already a high correlation. Indeed, the here depicted waveforms exhibit a correlation of 97.85%. On the right side of the figure, the direct comparison between both signals is visualized, where the amplitude of the instantaneous intracavity field of the leader cavity is plotted with respect to the instantaneous intracavity field of the follower field.

The graph validates the calculation of the correlation between both signals, as all the data points are aligning neatly along the diagonal of the graph.

How the correlation behaves over time is depicted in Fig. 3.12. Employing the parameters from above, the simulation is conducted 10 times, the correlation between each resonator per round trip is calculated and plotted with respect to the round trip number. In the beginning of the graph, a similar phenomenon as above in Fig. 3.9 can be seen, namely that the starting correlation differs for each run, because the resonators are not connected during MI comb generation. The moment the leader comb is injected into the follower comb, the follower comb is changing in order to adjust itself to the signal of the leader comb. Over the period of the first 1000 round trips, the waveform of the instantaneous field of the follower ring is increasingly copying the waveform of the instantaneous field of the leader ring. When averaging the correlation of the different simulation runs, the total correlation results to over 90%, meaning the synchronization is high enough for chaos secure communication applications.

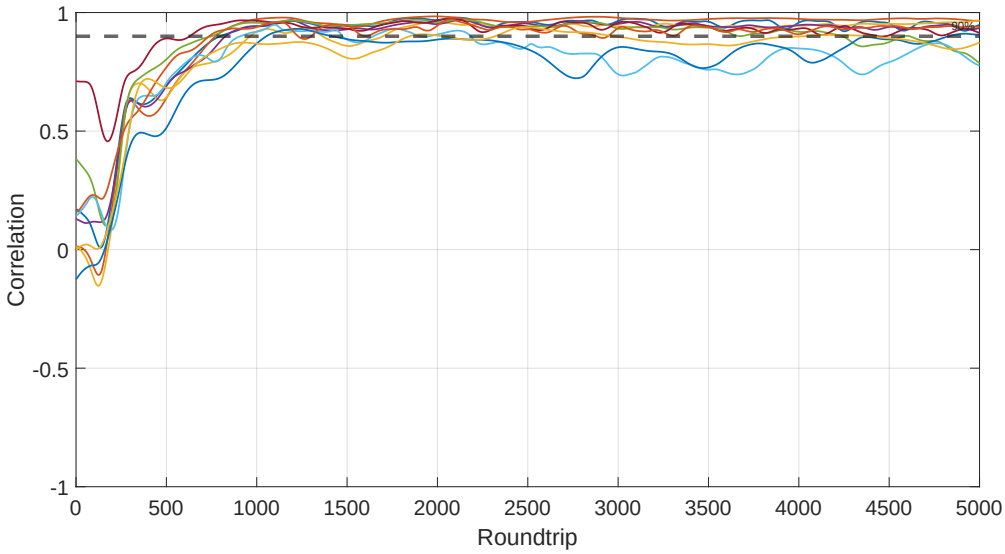

Figure 3.12: Correlation between both resonators for 10 different runs

In order to increase the correlation on average, a question remains. It still has to be found whether there is a parameter which is not fixed, that the synchronization depends on. Comparing the temporal waveforms for different correlation values might give insights in this matter.

Regarding the Reproducibility of Synchronization

Already perceptibly present in Fig. 3.12 is the inconsistency of synchronization, when repeating the simulation where all controllable parameters are kept the same. The only variable in the repetitions of the simulation is the added noise to the input CW laser. In this section the reason for the differences in synchronizability is investigated.

First, the crosscorrelation seen in Fig. 3.12 is averaged for every run over the last 2500 simulated round trips. The same is done for the effective detuning of each resonator for each run. Then, a representative temporal waveform is picked to compare the different correlations. In figure 3.13, 6 runs are represented by one round trip in each ring, and compared by their achieved correlation. The first row depicts a simulation run, where the highest correlation was achieved, the runs in the next rows are lined up in a decreasing order regarding their achieved cross correlation, XC. On the left side, one representative waveform of the leader ring can be seen for each case, which is juxtaposed on the right side with the corresponding temporal waveform of the follower ring. Furthermore, the averaged detuning, $\Delta\delta_{\text{eff}}$, is added to each case.

While this approach is not quantitatively but rather qualitatively investigating the relationship between correlation and temporal waveform, the leader ring shows a strong effect that the form of the temporal signal has on the correlation. When considering the simulation runs with decreasing correlation, it seems as if the chaoticness of the

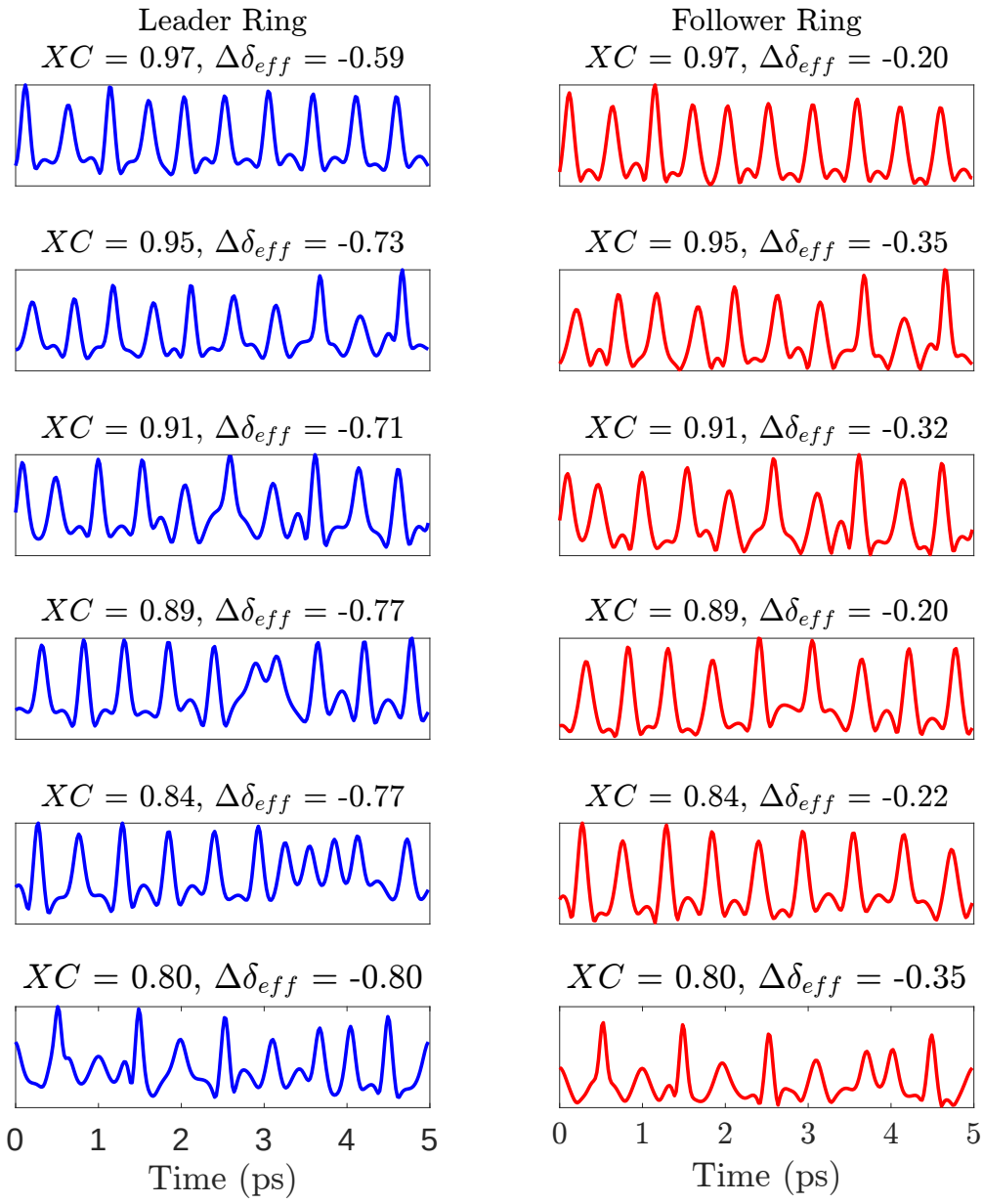

Figure 3.13: Temporal waveforms for differences in correlation and effective detuning

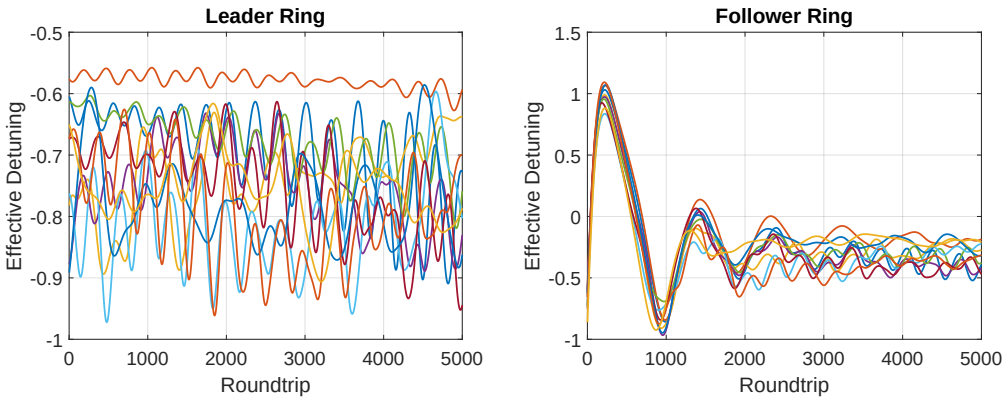

Figure 3.14: Effective detuning evolution for each run

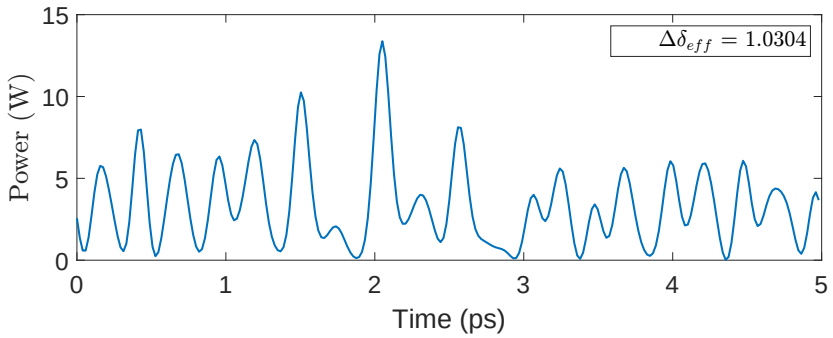

Figure 3.15: Positive effective detuning in the follower ring

signal is worsening the synchronization, as higher synchronization is achieved for a temporal signal that almost looks like a multisoliton waveform. In contrast to that, the synchronization result is below the minimum threshold for application, when the temporal waveform looks more chaotic. As the effective detuning is moving deeper into the blue-detuned regime, decreased from -0.59 to -0.8, the synchronization worsens. A similar effect of increasing chaoticness which decreases the synchronization can be seen for the follower ring. However, the leader ring seems to have more influence on the synchronizability, because even though the follower ring more often exhibits a multisoliton state-like temporal waveform, it fails to follow the leader correctly.

A reason for this multisoliton state-like might lie in the effective detuning. In figure 3.14 the evolution of the effective detuning in each ring is visible for the different repetitions of the simulation, again, recorded from the moment of connection between follower and leader. While the effective detuning for the leader resonator starts at some value and keeps oscillating in that same regime, the follower resonators effective detuning exhibits a strong shift into the positive regime when leaders signal is injected into it. The effective detuning being in the positive regime means that the ring is red-detuned, or rather, it has left the regime of the MI comb. However, the signal is still chaotic, as shown in Fig. 3.15, where the instantaneous field inside the cavity is shown

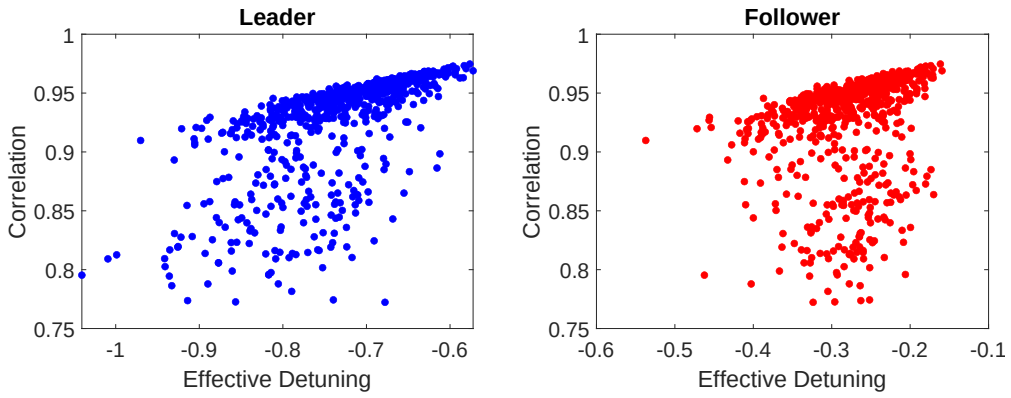

Figure 3.16: Correlation vs. effective Detuning

for said positive effective detuning of $\Delta\delta_{\text{eff}} = 1.03$. After a few hundred round trips the effective detuning returns to the blue-detuned state, and only then the instantaneous field inside the cavity is stabilizing itself to become that multisoliton-like state.

Finally, the relationship between the synchronization, or, the correlation between both cavities, is investigated with more samples. This time, the simulation is repeated 700 times using the same parameters, the effective detuning in each resonator and the average correlation between both resonators is recorded. These results are shown in Fig. 3.16. Indeed, a relation between correlation and effective detuning can be seen, namely the synchronization is better for an effective detuning which is closer to the actual effective resonance in the blue-detuned regime.

However, there are also a lot of data points which are an exception to this rule, meaning synchronization might also fail even if the effective detuning is in the right regime.

3.2.4 Effect of changing parameters on the synchronization

This section covers the effect different changing parameters have on the synchronization, in order to maximize the synchronization and increase the understanding for chaos synchronization of microcombs.

No second Pump

In this part, the synchronization is analyzed, for the case of no comb generation in the second resonator, meaning $\alpha_{\text{pump}_2} = 0$. First, the MI comb is generated in the leader resonator, and because there the second pump parameter is set to zero, no field is generated in the follower resonator. Figure 3.17 shows the moments right before and directly after the first comb is injected into the the second one. On the left, where the fields before the connection are depicted, only the leader resonator exhibits

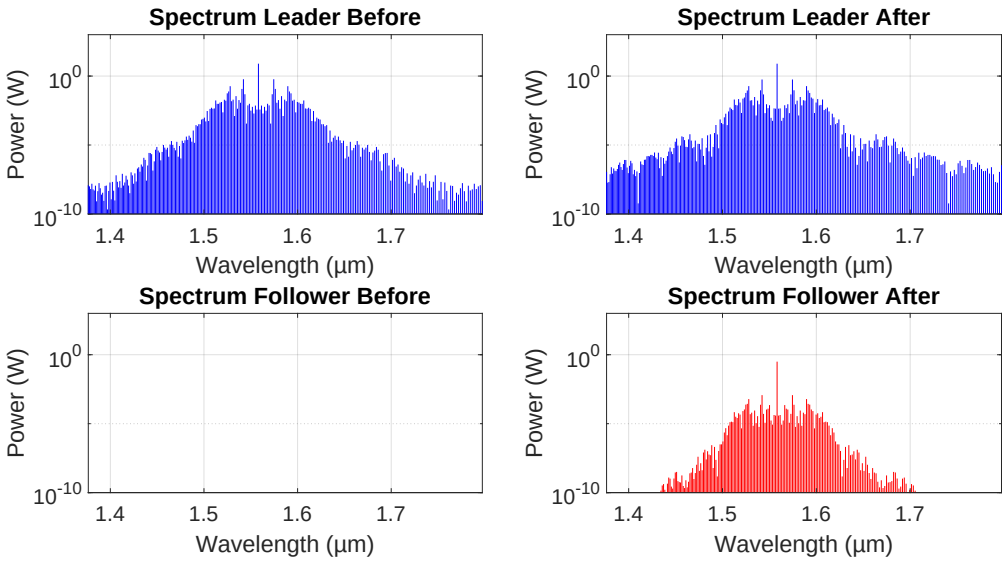

Figure 3.17: No second pump $\alpha_{\mathrm{pump}_2} = 0$

a comb. Right after cascading both resonators, the first field is inserted into the second resonator, and fields are visible in both resonators.

When determining the cross correlation between the instantaneous fields inside the leader and follower ring, high correlation can be observed. In Fig. 3.18, the cross correlation for 10 different simulation runs, which run for 5000 round trips each, can be seen. Because there was no intracavity field in the follower resonator before cascading both resonator, the cross correlation between both fields starts out very high and stays mainly above 90% for most of the runs. There are also exceptions where the correlation evolves below 90%, but in general the correlation between both signals is good enough for applications.

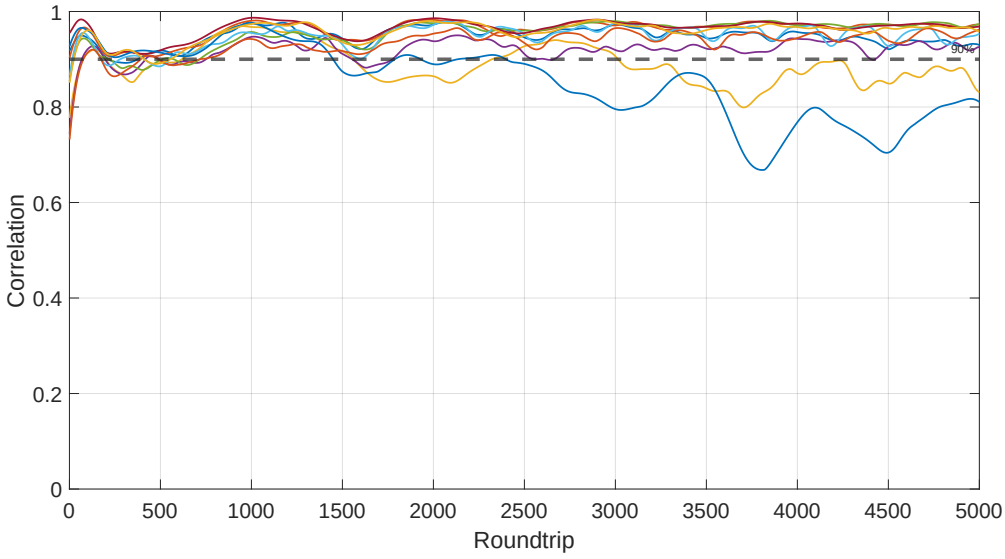

Figure 3.18: Correlation between both rings for 10 different runs

Changing the injection factor

In this section the effect of the change of the injection factor on the synchronization is briefly analyzed.

This time, the method to record the data is changed. First, both MI combs are generated without any connection. Then, the first 3000 round trips are calculated and recorded with an injection factor $\beta_{\text{inj}} = 0$, the pump factor is set to $\alpha_{\text{pump}_2} = 0.01$. After that, the injection factor is increased in 0.05 increments, while calculating 3000 round trips for each step. The correlation is then determined for each round trip and averaged over the 3000 round trips for each injection factor increment. The results are shown in Fig. 3.19. This approach to sweep the injection factor while both rings are connected might not be the best, because the injection factor used above, $\beta_{\text{inj}} = 0.55$ yielded over 90% correlation, while it is just above 85% here. Still, it shows that the synchronization has a dependence on the injection factor β_{inj}.

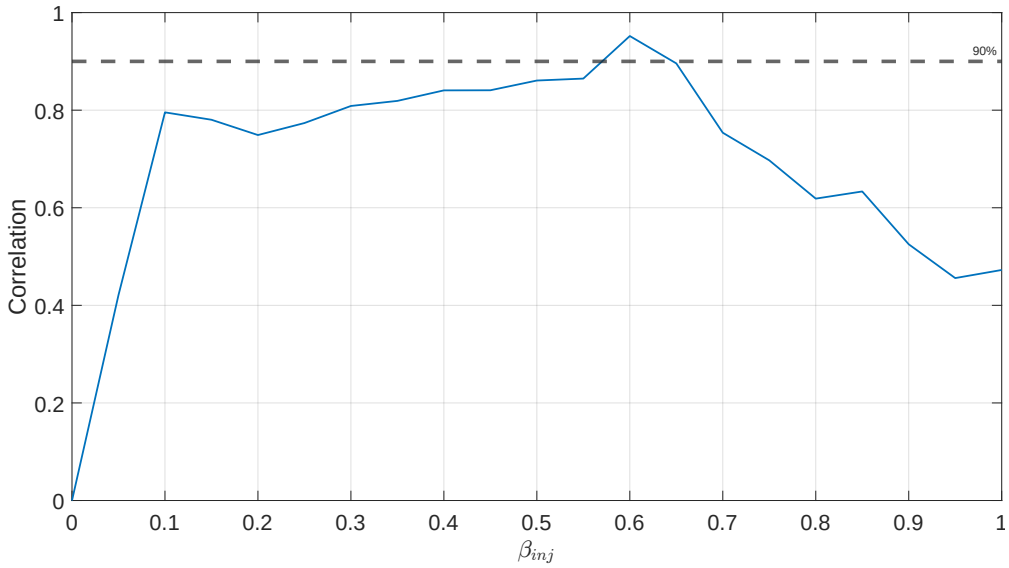

Figure 3.19: Correlation for different different values of injection factor β_{inj}

Effect of noise in the transmission line on the synchronization

In the real world, noise becomes an inevitable companion. The following section deals with the effect of noise in the transmission line on the degree of synchronization.

In Fig. 3.20, the correlation between the instantaneous fields of leader and follower ring is calculated for different values of the signal-to-noise-ratio(SNR). In the fast step of calculating the Lugiato-Levefer equations, each round trip a different temporal noise waveform is added to the temporal output waveform of the leader resonator. Depending on the current SNR, the amplitude of the added noise waveform is adjusted. To put

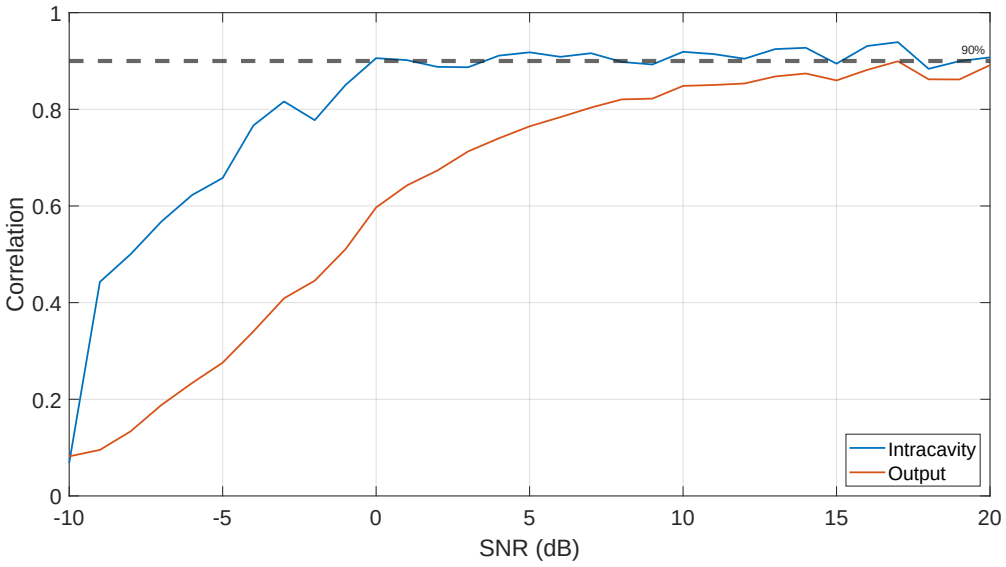

Figure 3.20: Correlation between both resonators for different levels of noise

this into equation form:

$$A_{\mathrm{N}} = \mathrm{rand}(N), \tag{3.28}$$

where A_{N} is the temporal noise waveform, that will be added in one iteration, and $\mathrm{rand}(N)$ is a function generating random numbers between -1 and 1, where N is the number of data points per calculated round trip. To calculate the amplitude of the previously generated randomized temporal signal, the powers need to be calculated and adjusted according to the SNR.

$$P_{\mathrm{S}} = \frac{1}{N}\sum_{i=0}^{N} |A_{\mathrm{out}}(i)|^2 \tag{3.29}$$

$$P_{\mathrm{N}} = \frac{P_{\mathrm{S}}}{\mathrm{SNR}_{\mathrm{lin}}} \tag{3.30}$$

$$P_{\mathrm{N_{init}}} = \frac{1}{N}\sum_{i=0}^{N} |A_{\mathrm{N}}|^2, \tag{3.31}$$

where P_{S} is the average power of the signal per data point in the present iteration, P_{N} is the average power the noise signal should have according to the SNR, with $\mathrm{SNR}_{\mathrm{lin}}$ being the SNR in decimal scale, and $P_{\mathrm{N_{init}}}$ is the average power of the generated randomized noise signal, which still has to be adjusted. Knowing the relevant powers the generated noise signal can be adjusted:

$$B_{\mathrm{in}} = \beta_{\mathrm{inj}} \left(A_{\mathrm{out}} + A_{\mathrm{N}} \sqrt{\frac{P_{\mathrm{N}}}{P_{\mathrm{N_{init}}}}} \right). \tag{3.32}$$

Inserting B_{in} into the follower cavity, the effect of noise in the transmission channel is

analyzed.

This time, not only the intracavity fields are compared, but also the output fields of each ring. As one sees in Fig. 3.20, the correlation between both signals is increasing with an increasing SNR. Each data point is calculated from averaging the cross correlation of 5 different simulation runs with 5000 round trips each. Noticeable in this graph is the discrepancy between the intracavity field and the output field. While the intracavity fields synchronize very early at an SNR of 0 dB, the output fields seem to find a managable synchronization starting at an SNR from around 15 dB. This discrepancy is because of the filtering effect of the microresonator. Only the frequencies around the resonance frequencies are able to couple into the microresonator. Therefore, most of the noise is filtered out. This means, that the synchronization seems to be very robust against external noise. Since the noise is mainly present in the waveguide that provides the follower ring with the signal from the leader ring, a method to extract the synchronized signal with less noise, is to utilize an add-drop resonator.

4 Experiment

This chapter reveals the evolution of the experimental setup. Since the approach of synchronizing two microring resonators by cascading them is novel, there is yet no report on how to set an experiment up. To motivate and justify it's viability, the experimental setup is built up step by step in this chapter. First, the methodology is discussed, which is followed by the results and the discussion afterwards, where the experiment in its different stages is shown, which is split into four stages. The four stages go from simply measuring the Q-factor and determining the resonances of the resonator, to an characterization of the MI comb to a dual MI comb generation over to the synchronization setup. Additionally for the methodology part, a setup for a detuning measurement is shown, although it was not conducted in the real experiment.

4.1 Methodology

To introduce the different experiment setups, this methodology section will list, elucidate and exemplify the various procedures. The investigated microresonators are integrated on a chip as already elucidated in chapter 2.2.1, but they are shown again in figure 4.1. On the left 4.1a, the design plan is pictured where the fiber array is clearly visible with each channel being labeled. These labels will be used below to specify the experiment setups and discuss the results. On the right 4.1b, the actual fabricated chip is depicted.

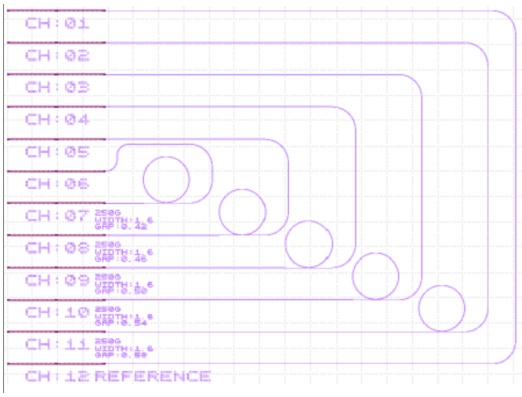

(a) Design for the chip

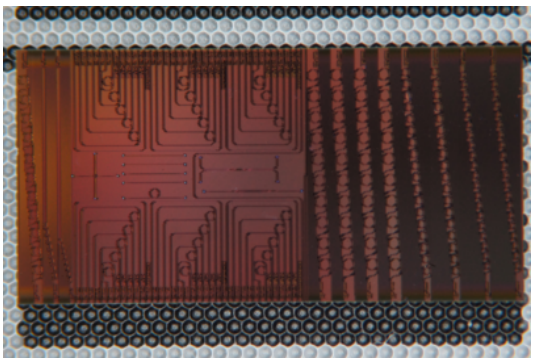

(b) Picture of the fabricated chip

Figure 4.1: Integrated microrings with fiber array

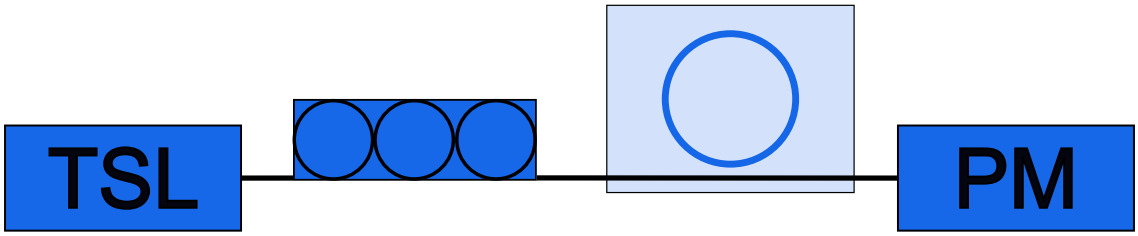

Figure 4.2: Q-Measurement setup

TSL	Santec TSL-710
Resonator	FSR = 250 GHz
PM	Agilent 81634B

Table 4.1: Equipment for Q-Measurement

4.1.1 Q-Measurement

One of the most significant parameters of the resonator is as discussed in chapter 2.2.1 the quality factor and of course the resonance frequencies. The following measurement procedure is set out to determine these parameters. In figure 4.2, the experimental setup is depicted. A tunable semiconductor laser (TSL) is inserted into a polarization controller (PC) that is connected to one of the packaged resonators. Specifications of the used equipment is summarized a table below 4.1.

The output of that chosen resonator is measured by a power meter (PWR). Utilizing the PWR connected to a computer enables the measurement of a transmission spectrum, where the wavelength of the TSL is swept from smaller to longer wavelengths. While sweeping, the power output behind the resonator is measured and the transmitted power with respect to the wavelength can be analysed, as seen in figure 4.3. This measurement is not only used to determine the resonance wavelengths but also to set the PC correctly. In Fig. 4.3a, the resonances of the microring are visible. As the resonator absorbs light at its resonance frequencies, the measured power at the PWR also drops. The resonance frequencies correspond to these transmission dips. However, the resonances also depend on the polarization, meaning depending on the composition of transverse electric (TE) and transverse magnetic (TM) modes, the TE or TM resonances are visible to a different degree. The PC has to be set in order to let mainly TE modes propagate, since the TE resonances have a higher Q-factor and microcomb generation achieves better results with TE modes. The here depicted resonances show the TE resonances.

By analyzing the transmission spectrum around the resonance wavelengths, the Q-factor is determined. As presented above in section 2.2.1, the Q-factor is sufficiently

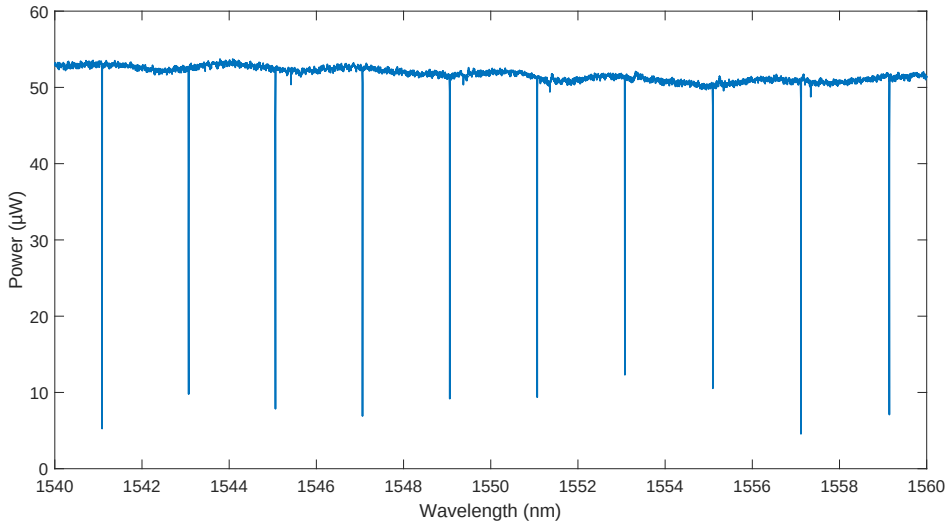

(a) Example Transmission Spectrum

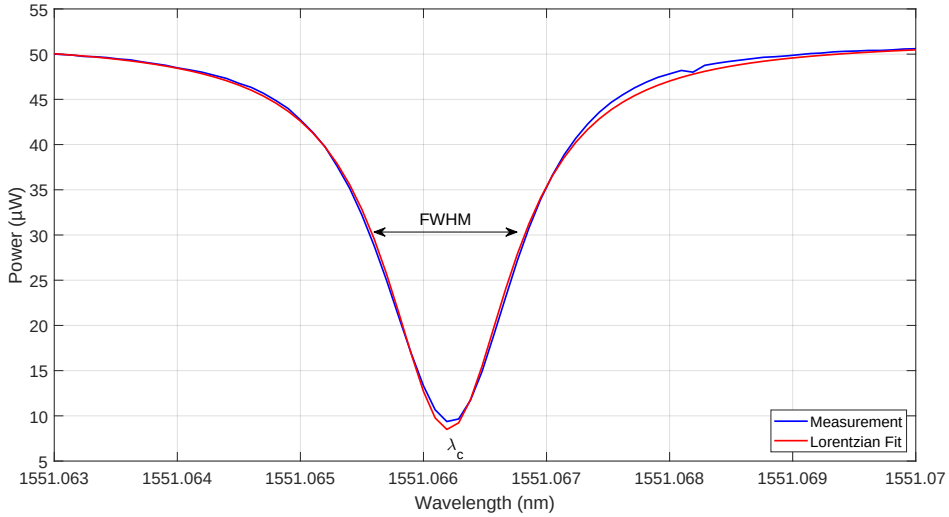

(b) Analysing the Resonance

Figure 4.3: Transmission-Wavelength

approximated by the ratio of the resonance frequency and the bandwidth of the resonance dip. In order to determine the Q-factor for one resonance, first the resonance wavelength has to be determined, which is simply one of the local minima in the transmission spectrum. In Fig. 4.3b, the very spectrum around a resonance wavelength can be seen. To calculate the Q-factor, a fit with a Lorentzian curve is done 4.1.

$$f(x) = y_0 - \frac{2A}{\pi} \frac{\text{FWHM}}{\text{FWHM}^2 + 4(x - x_c)^2} \tag{4.1}$$

To fit the experimental values to a mirrored Lorentzian curve four parameters are introduced. y_0 is the y-offset from the origin, A describes the area between the Lorentzian and y_0, FWHM is the width of the Lorentzian at its halved maximum value and x_c is the center wavelength of the resonance. Then, the center wavelength and the FWHM

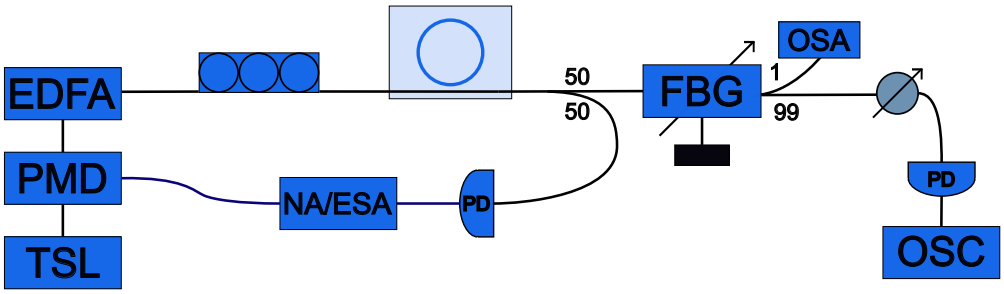

Figure 4.4: Experiment Setup to Measure Detuning

of the Lorentzian function is used to determine the Q-factor of that resonance,

$$Q = \frac{\lambda_c}{\Delta\lambda} \tag{4.2}$$

where λ_c is the resonance wavelength and $\Delta\lambda$ the FWHM of the dip in the transmission spectrum. In this example measurement, the resonance around $\lambda_c = 1551.066\,\text{nm}$ is investigated, and a bandwidth of FWHM $= 1.2\,\text{pm}$ is determined which evaluates to

$$Q = \frac{\lambda_c}{\Delta\lambda} = \frac{1551.066\,\text{nm}}{1.2\,\text{pm}} = 1.26 \times 10^6. \tag{4.3}$$

In the experiments below, the Q-factors of the resonators are determined according to this procedure, whenever possible. As this is a fast way to get not only a value for the Q-factor of the resonator, but also to set the polarization of the PC in the correct way to suppress the TM modes.

4.1.2 Detuning Measurement

Another value one might be interested is the detuning, which is effectively the distance between the resonance wavelength and the wavelength of the pump laser. In order to measure the detuning between the pump laser and the nearest resonance of the microring, the following approach is utilized. The main idea of this setup is to measure the effective detuning, since it is not determinable without actually measuring it. This is due to the fact that the effect the thermals or the nonlinearities in the cavity on the resonances have is only approximatable, even though the resonances are measured before and the pump laser's wavelength is known. The setup is shown in Fig. 4.4, and the specifications of the equipment used is shown in Tab. 4.2.

Compared to the setup for measuring the Q-factor, first an phase modulator (PMD) and an erbium-doped fiber amplifier (EDFA) is inserted between the TSL and the PC. This setup requires the PC to be set correctly, that only TE modes are transmitted to the resonator, and broad comb generation is possible. The TSLs power is set to

TSL	Santec TSL-710
EDFA	PriTel PMFA-30-10
PD	Thorlabs DET08CFC/M
ESA	Siglent SSA 3032X-R

Table 4.2: Equipment for the Detuning Measurement

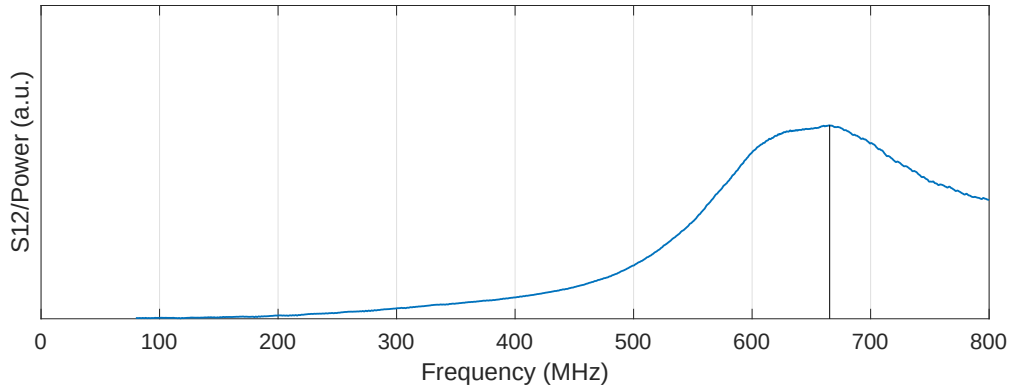

Figure 4.5: Graph depicting the measured Beatnote-spectrum (Data from [91])

3 dBm and amplified by the EDFA, so that an output power of 1 W is achieved, which is inserted into the PC that is connected to the resonator. By setting the TSL to a wavelength smaller than a chosen resonance wavelength but close to that resonance wavelength and slowly increasing the wavelength of the TSL, the comb is generated.

The generated output signal of the resonator is split into two fibers. One fiber goes into a fiber Bragg-grating (FBR) to filter the pump signal out, which is then first measured by an optical spectrum analyzer (OSA), further attenuated and converted into an electrical signal by a photodiode (PD), which sends the electrical signal to an oscilloscope (OSC). The other fiber goes directly into a PD, converting the light signal into an electrical signal, which is sent to a network analyzer (NA) or an electrical spectrum analyzer (ESA) with a tracking generator (TG), that controls the PMD. Here, a vector network analyzer or a scalar network analyzer would both work fine, but the used analyzer is an ESA with a TG. The detuning between pump and resonance wavelength can then be read from the measured spectrum of the ESA, as seen in figure 4.5. The present spectrum radio frequency (RF) spectrum and the effective detuning is read by determining the maximum value of said RF spectrum.

To explain the measurement of a peak, the existence of the feedback loop has to be motivated. The TG of the ESA is producing the same frequencies as the ESA is measuring, as the output signal of the resonator is inserted into the ESA. Feeding the PMD with the signal of the tracking resonator, the phase of the TSL is modulated according to the frequencies generated by the TG. Because of the phase modulation, the pump laser develops side bands, which are depicted in a simple schematic in figure 4.6a.

When looking at the frequency spectrum, the pump gains sidebands symmetrically to the pump frequency, f_{pump} and equidistant between each sideband. The idea, here, is to utilize the sidebands as a tool to measure the effective detuning. When the wavelength of the TSL is adjusted, meaning it is increased in order to move closer to the resonance wavelength, the mode's sidebands move closer to the resonance, too. In Fig. 4.6b, this process is depicted. Important to note, this graph shows the frequency instead of the wavelength, meaning as the wavelength is increased, the frequency of the emitted CW from the laser becomes smaller and moves closer to the resonance frequency. As one of the sidebands is absorbed by the resonator, the symmetric counterpart finds itself in an unbalance and forces the system to generate a beatnote between the uncompensated sideband and the pump frequency. The generated RF signal is measured by the ESA and the frequency of the peak in the ESA spectrum is the beating frequency generated by the unbalance of the sidebands.

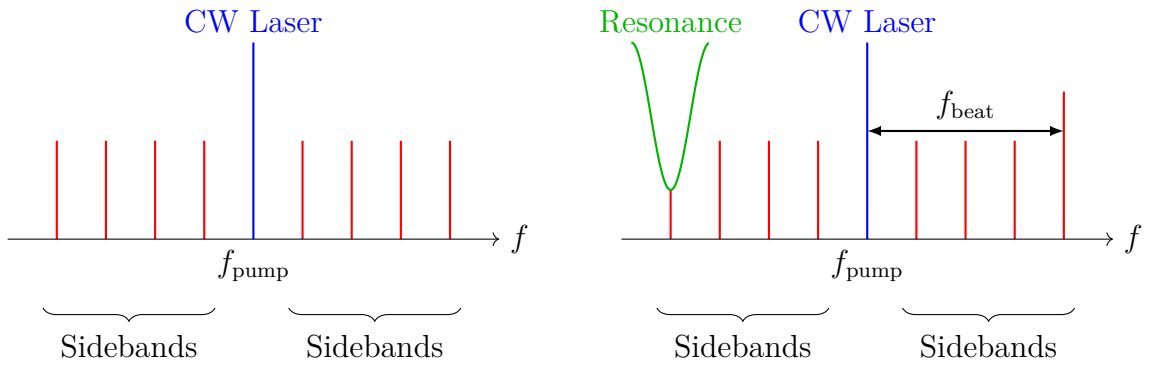

(a) Pump with Sidebands (b) Resonance absorption

Figure 4.6: Phase-modulated pump with sidebands approaching a cavity resonance

But this approach has a few drawbacks. First, the ESA which is used for the control of the PMD measures only with two decimal places. Second, and the significant drawback for this method is its deficit in accuracy when approaching the resonance. When increasing the wavelength and decreasing the detuning, the measured peak of the RF spectrum moves to lower frequencies. But only down to a certain point, where it stops moving further to smaller frequencies, even though the detuning is decreased. Because of this reason, the detuning is not measured in the following measurements.

To summarize, a simple feedback loop is introduced to generate sidebands of the pump laser, enabling measuring the detuning between the laser and the next resonance. However, this approach is not used in the following sections, as it is not accurate enough for the MI state of the comb.

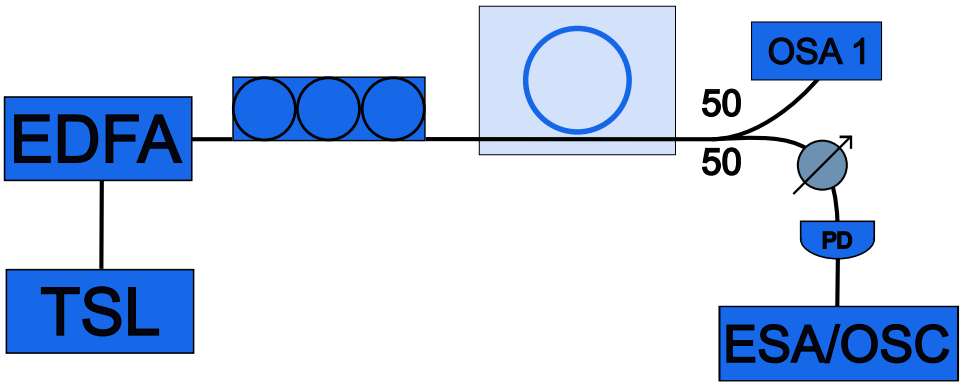

Figure 4.7: Experimental Setup for Comb Generation

4.1.3 MI Comb Characterization

In this section the setup for the generation of an MI comb is presented as the MI comb is to be analyzed afterwards. The goal is to determine the quality of chaos and whether it is random enough for possible applications. In order to do so, a bifurcation diagram is created, the chaos attractor diagram is examined and the autocorrelation function of the chaotic signal is determined. Especially, the effect of different parts of the setup on the autocorrelation function of the chaotic signal is studied. Those different setups are presented in this section.

MI Comb Generation

This section presents the setup for generating an MI comb and presents briefly the different approaches used to characterize the chaos. A simple setup is shown in figure 4.7, where a TSL is used with an output power of 3 dBm and inserted in an erbium-doped fiber amplifier (EDFA). The EDFA amplifies the signal to 1 W, or 20 dBm, which is put into the previously set PC, that connects the EDFA and the resonator on the chip. The PC is set during the Q-measurement, where the TM modes are suppressed. Since mainly TE modes are present, the MI comb is generatable. The output signal of the resonator is then injected into a fiber Bragg-grating (FBG) which reflects and filters the pump wavelength out. Behind the FBG the signal is tapped by a 1:99 beam splitter, where one percent of the signal goes into an optical spectrum analyzer (OSA) and the other 99 percent are detected by a photodetector (PD), which is connected to an oscilloscope (OSC). In order to comply with the maximum input power of the PD, an optical attenuator is adjusted as needed. The specifications of the equipment used is shown in Tab. 4.3.

The actual MI comb is generated by tuning the TSL. Since there is no need to generate a soliton comb, extensive control setups are not needed to keep the generated

TSL	Santec TSL-710
EDFA	PriTel PMFA-30-10
PD	Thorlabs DET08CFC/M
ESA	Siglent SSA 3032X-R
OSC	Rhode & Schwarz RTE 1104
OSA 1	Yokogawa AQ6375B

Table 4.3: Equipment for Comb Generation

comb in place, as the MI comb is stabilizing itself. First, the wavelength of the TSL is set close to a previously chosen resonance wavelength.

Here, the thermal resonance shift has to be taken into account, because the resonances earlier were measured with a laser output power of just $-10\,\mathrm{dBm}$, but now the resonator is pumped with $10\,\mathrm{dBm}$. This leads to a heating up of the cavity so, that the resonance wavelength is shifted to a longer wavelength. Therefore, a small shift is added to the initially measured "cold" resonance, where usually a shift of around $100\,\mathrm{pm}$ is used. When trying to generate an MI comb, the "cold" resonance of the chosen resonance wavelength is taken and prolonged by the above approximated thermal shift. Note, a meticulously exact calculation of the thermal shift is not needed as the pump laser does not need to be perfectly aligned with the resonance wavelength, but only on a wavelength just below the "warm" resonance, because the laser is swept to longer wavelengths anyway.

After choosing and setting the initial pump wavelength for the TSL, it is manually increased, decreasing the detuning between pump laser and effective resonance wavelength. This process of generating an MI comb by increasing the wavelength of the pump laser is presented in figure 4.8. From subfigures (a) to (j) the pump wavelength is increased and approaches the effective resonance wavelength of the chosen resonance. The y-axes are showing the power and the x-axes the corresponding wavelength. For this visualization no bandpass filter (BPF) is used, so the amplified spontaneous emission (ASE) noise is visible in the measured optical spectrum. First, only a Turing pattern is visible, which then evolves into an MI comb.

As the pump wavelength is increased and moves closer to the resonance wavelength, different stages of the comb are observed. First, only a continuous wave (CW) is seen in addition with the ASE noise. Then, more comb lines start to emerge and the Turing pattern appears and manifests itself. As the laser's wavelength is elongated an increasing number of comb lines adds itself to the existent Turing pattern, starting to form the MI comb. By further tuning the wavelength, the spectral components of the MI comb grow greater, finally resulting in a stable, high power, flat-top spectrum. However, if the pump wavelength is increased even further beyond the stable regime of

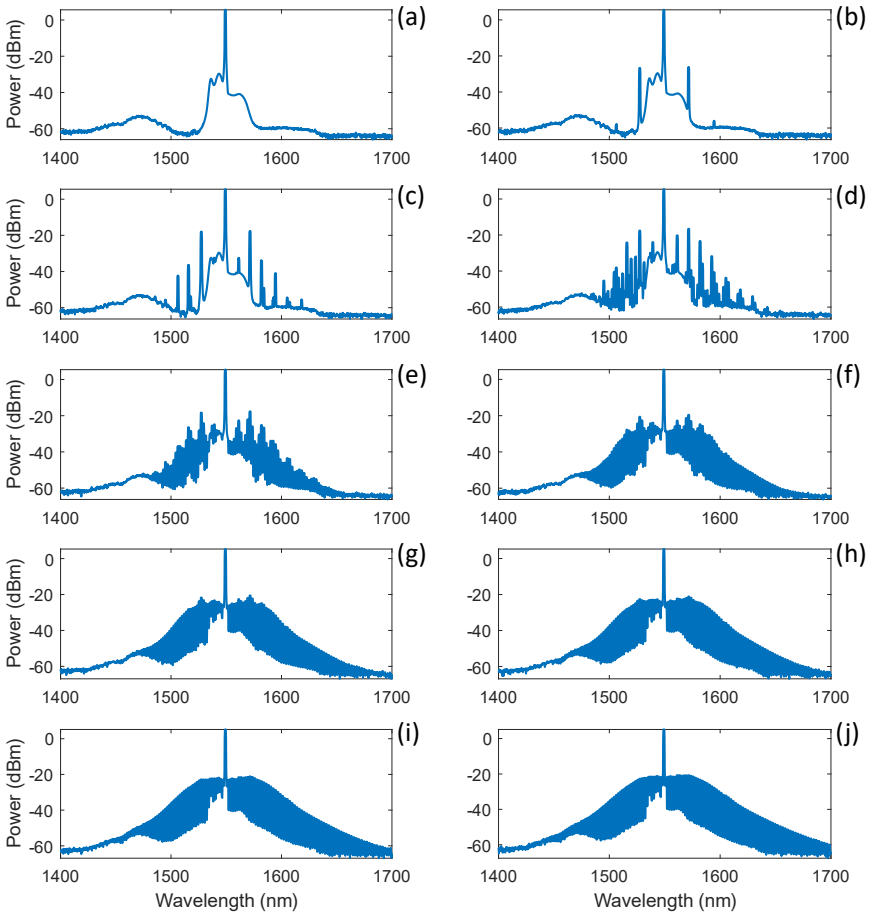

Figure 4.8: MI Comb Evolution

the MI comb, the comb disappears and leaves only the CW spectrum. Unfortunately, the in this chapter presented approach on measuring the effective detuning is not accurate enough and was not conducted in these experiments. If one was able to measure the effective detuning exactly, one could compare the simulation results better to the experimental results.

In addition to the optical spectra which were measured by an OSA, also the electrical spectra for the base band, measured by the ESA, and the temporal chaotic signal, measured by an oscilloscope, are analyzed. The ESA has a maximum bandwidth of 3.2 GHz and is provided with an electrical signal through an PD with a maximum bandwidth of 5 GHz. The oscilloscope has an analog bandwidth of 1 GHz and samples with 5 GSa s^{-1}, but is in a few measurements only connected to a PD with a maximum bandwidth of 100 MHz, but most of the measurements are done with a PD with a bandwidth of 5 GHz.

The measured electrical spectra are investigated with different pump powers of the

EDFA and a varied detuning. With the obtained data from the oscilloscope the chaos can be analyzed with different approaches. First, a bifurcation diagram is presented by plotting the local maxima of the temporal signal for each increase-step of the pump wavelength. Then, a chaos attractor is tried to be reconstructed, using the approach mentioned in 2.3. The most important measure to characterize the chaos might be the autocorrelation and its FWHM because of its simplicity.

Since the focus on the chaos characterization and the later synchronization will require a high use of the autocorrelation and crosscorrelation, the effect of different experiment equipment has to be determined. Here, the effect of the FBGs and an BPF on the autocorrelation, and with that also the crosscorrelation, is investigated.

Effect of Different Fiber Bragg-Gratings on Autocorrelation

When utilizing two rings and letting them synchronize, it needs to be investigated how the FBGs are affecting the correlation between two signals. Assuming an ideal case of two synchronized rings, the crosscorrelation between the leader and follower signal should be close to 1, as the normalized Pearson coefficient is utilized to determine the crosscorrelation. However, when the output of each ring is filtered by a different FBG or when one is not filtered while the other one is filtered, it could lead to an impairment of the crosscorrelation. Therefore, it is analyzed how significant this alteration is. The above mentioned two cases are investigated in this section. Figure 4.9 shows the setup for both cases. The specifications of the equipment are written in 4.4. First, the effect of only one FBG on the signal is studied, as seen in figure 4.9a. The left part of this setup, including the ring resonator, is generating the MI comb, while the right part works as the measuring part. Here, only one resonator is used, which signal is split into half using a 3 dBm-splitter afterwards, meaning the signal is split into two equal parts. The first part is inserted in a FBG, getting its pump mode filtered out, and then measured by an OSA and OSC. The second part of the split signal is directly fed into a PD that is connected to the oscilloscope.

TSL	Santec TSL-710
EDFA	PriTel PMFA-30-10
PD	Thorlabs DET08CFC/M
OSC	Rhode & Schwarz RTE 1104
OSA 1	Yokogawa AQ6375B
OSA 2	Yokogawa AQ6370D
FBG 1 (variable)	Alnair WTF-200
FBG 2 (variable)	FLT Photonics Fiber Bragg Grating Tuner (Model:C)
FBG 3 (fixed)	Tatsuta FBG-SMF-1550.5-99-50-LS-FPC-IM

Table 4.4: Equipment when investing the impact of FBGs

With both temporal signals at hand, the autocorrelation function with and without FBG can be calculated. Furthermore, the cross correlation between both signals gives insight about how the chaotic signal is changed by filtering it with an FBG.

The second variation of this setup, seen in figure 4.9b, utilized not just one but two FBGs at the same time. Three different FBGs are investigated, two with variable modes and one with a fixed reflected mode. As each FBG is a different model, the filtering behavior differs, too. That is why, it is important to validate whether the same signal inserted in two different FBGs is behind them still highly correlated or not. The variable FBGs are set to optimally block the pump mode at 1551 nm, which is slightly offset from the fixed FBG, which is set to 1550 nm.

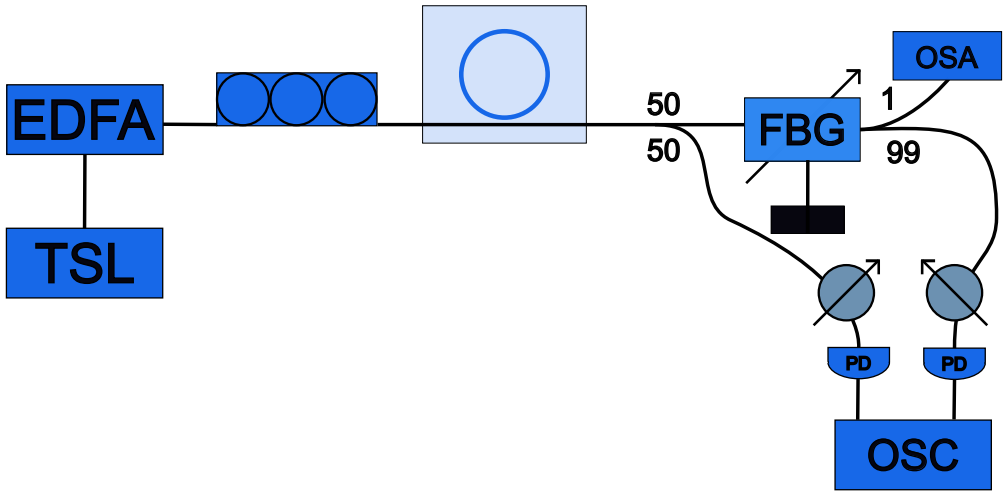

(a) Effect of one FBG

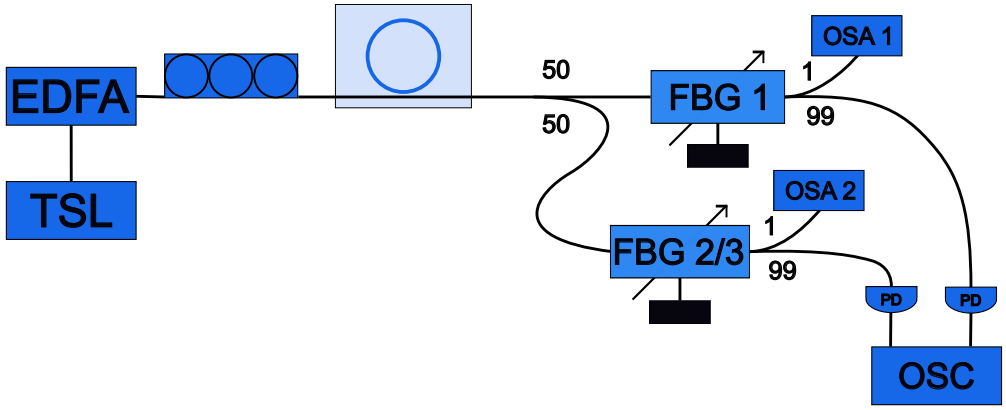

(b) Effect of two different FBGs

Figure 4.9: Setups to analyze the effect the FBG has on the correlation

Effect of a Bandpass Filter on Autocorrelation

In the case of reamplifying the output signal, it is important to filter the ASE noise out, so that the ASE noise from the previous EDFA is not amplified again. To inves-

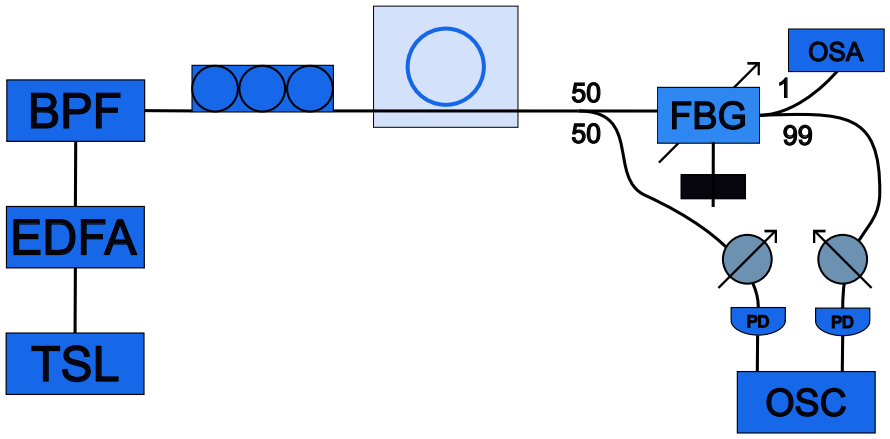

Figure 4.10: Setup to analyze the effect of the BPF's FWHM on the correlation

tigate the impact of the BPF, or more specifically the BPF's FWHM, on the signal and its autocorrelation function, the following setup is created, mostly similar to the previous one, but with a BPF inserted between the EDFA and PC, Fig. 4.10. The used equipment is shown in Tab. 4.5.

TSL	Santec TSL-710
EDFA	PriTel PMFA-30-10
BPF	Yenista XTA-50
FBG 1 (variable)	Alnair WTF-200
OSA 1	Yokogawa AQ6375B
PD	Thorlabs DET08CFC/M
OSC	Rhode & Schwarz RTE 1104

Table 4.5: Equipment when investing the impact of FBGs

4.1.4 Dual MI Comb Generation

Since chaos strongly depends on the initial conditions, other groups were able to synchronize the chaos in semiconductor lasers which are driven by a common drive source. In this section, a similar concept is tested, where two resonators are pumped by the same laser. The setup can be seen in figure 4.11. The used equipment is shown in Tab. 4.6. Generating two MI combs simultaneously is similarly done as generating just one, since the only thing that is changed is the number of resonators. The resonators are on the same chip in the same area of that chip, which should make the deviation due to fabrication errors small enough, that the chaos only depends on the laser input. This hypothesis is evaluated by the dual MI comb generation.

Important to note, the beam splitter in front of the polarization controllers (PCs) is polarization maintaining (PM). First, the PCs are set to polarize the incoming light

to suppress the TM modes, which is done in a similar manner as before in the Q-measurement above in Fig. 4.2. After inserting the EDFA, the TSL's output power can be increased to 3 dBm and amplified by the EDFA to 1 W, which is then split by the beam splitter, so that the input onto the photonic chip for each resonator is effectively given by 500 mW. MI combs in each resonator are generated by sweeping only one laser which is amplified by only one EDFA but then inserted into two different PCs, slightly changing the initial conditions for each resonator. After generating the MI combs, the cross correlation between both combs is calculated from the measured temporal chaotic signal.

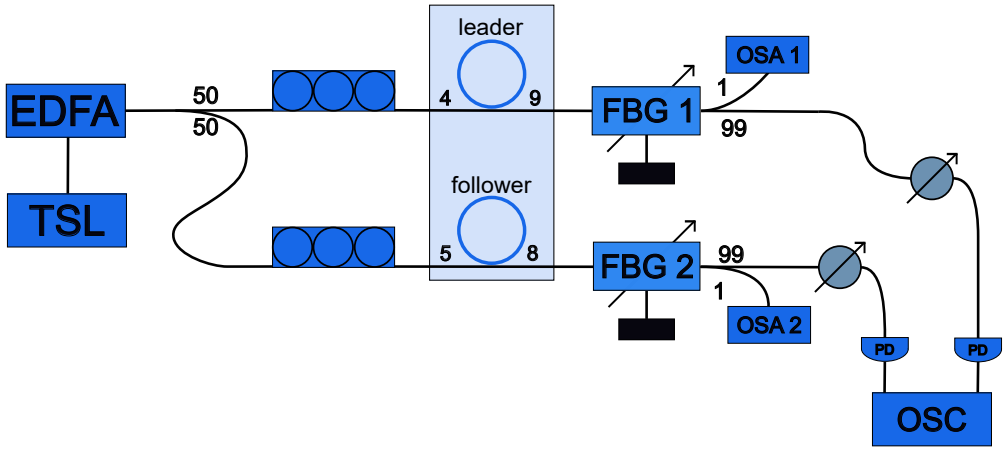

Figure 4.11: Setup for Dual MI Comb Generation

TSL	Santec TSL-710
EDFA	PriTel PMFA-30-10
FBG 1 (variable)	Alnair WTF-200
FBG 2 (variable)	FLT Photonics Fiber Bragg Grating Tuner (Model:C)
OSA 1	Yokogawa AQ6375B
OSA 2	Yokogawa AQ6370D
PD	Thorlabs DET08CFC/M
OSC	Rhode & Schwarz RTE 1104

Table 4.6: Dual Comb Generation

This short section dealt with the generation of two MI combs in two different but similar resonators on the same chip with only one laser, investigating whether a common drive solution might be feasible.

4.1.5 Synchronization Setup

Since generation of two MI combs at the same time was already shown in the previous section, the goal is now to cascade them in a master-follower configuration to achieve

synchronization as in the simulation. In the simulation, the output from the leader resonator is simply injected into the follower resonator with adjusted power. In order to replicate this scenario in the experiment, the setup shown in figure 4.12 is used. The used equipment is summarized in Tab. 4.7. Two different setups are investigated. While one setup is without any additional amplification of the leader signal 4.12a, the other setup also utilizes an EDFA to amplify the output signal of the leader comb, 4.12b. As in the simulation, MI combs in each resonator are generated, which is done with only one laser. The output of the leader comb is then taken and inserted in the follower comb, which is done by a variable optical attenuator (VOA) which is first set to attenuate the signal by 60 dBm to reduce the attenuation step-wise for each of the following measurements. Furthermore, in the setup scheme a switch between the laser and the follower resonator can be seen, which is realized in the experiment by inserting a terminator or removing it, in order to turn the pump for the follower off or on, respectively. Turning the pump for the follower resonator off is important to set the PC between the output of the first resonator and the input of the second resonator, so that the resonances which are seen behind the follower resonator are all induced by the polarization of that PC.

TSL	Santec TSL-710
EDFA	PriTel PMFA-30-10
FBG 1 (variable)	Alnair WTF-200
FBG 2 (variable)	FLT Photonics Fiber Bragg Grating Tuner (Model:C)
OSA 1	Yokogawa AQ6375B
OSA 2	Yokogawa AQ6370D
PD	Thorlabs DET08CFC/M
OSC	Rhode & Schwarz RTE 1104
BPF	Alnair TFF-15-1-PM-L-050-55
Second EDFA	PriTel LNTFA-15-MA

Table 4.7: Equipment for synchronization setup

Not much changes for the second setup with the EDFA to amplify the output of the leader resonator, except an additional BPF after splitting the pump laser before the light goes into the leader resonator. This is done to remove the ASE noise so that the EDFA in the secondary amplification stage is not amplifying the ASE noise of the main EDFA but only the signal. To set the third PC, right behind the VOA and second EDFA, it is not possible to conduct the laser scan anymore to find out how the light is polarized, because of the EDFA. Instead of sweeping the wavelengths of the laser as above mentioned, a different approach is used to set the polarization of the PC here. When generating a Turing pattern, it can be observed that the distance between the comb lines is smaller for TM modes than it is for TE modes. By changing the

polarization so that mostly TE modes propagate, the comb lines of the Turing pattern comb move farther apart from each other, the maximum achievable distance between these comb lines is when the PC is optimally set. Another way to check for the correct polarization is to utilize a power meter (PWR). Since the comb becomes broader with the correct polarization, setting the PC so, that the PWR measures the maximum achievable power, is also a way to determine the setting for an optimal polarization.

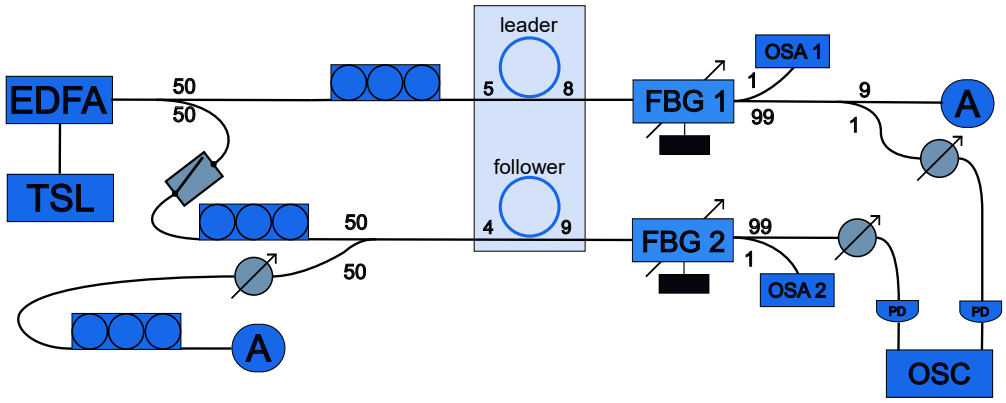

(a) Without further amplification

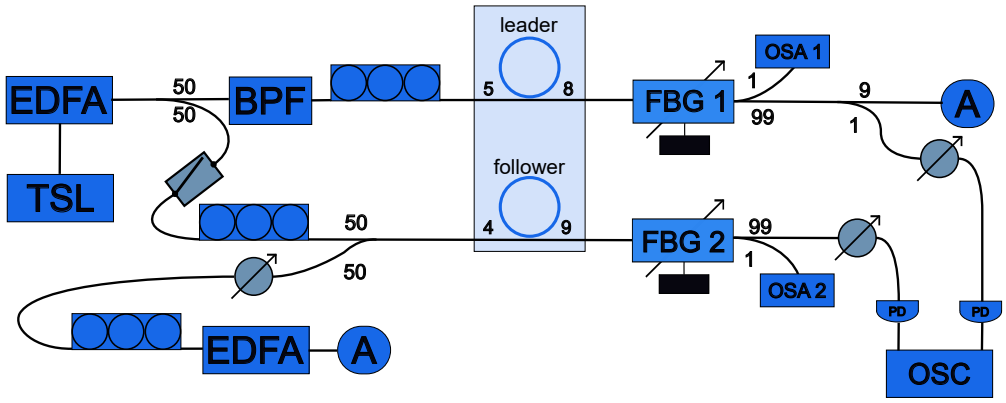

(b) With additional EDFA

Figure 4.12: Synchronization Setup via Cascading

The goal is to achieve synchronization of the cascaded resonators. A requirement for synchronization is the high correlation between both signals, and usually the measure used by other groups in the same field to determine whether two chaotic source are synchronized or not. The correlation value that has been established as sufficient for applications is a correlation of 90%, meaning a cross correlation between both signals exceeding this value is required. Furthermore, it has to be proved that this correlation value is because of the actual synchronization and not just the leader signal measured once again without coupling into the follower ring. This can be done by for example just inserting the lower half of the comb into the second follower, and measuring the upper half of the comb of each resonator to determine the cross correlation between each other. But since the symmetric modes of the MI comb exhibit a cross correlation, an even

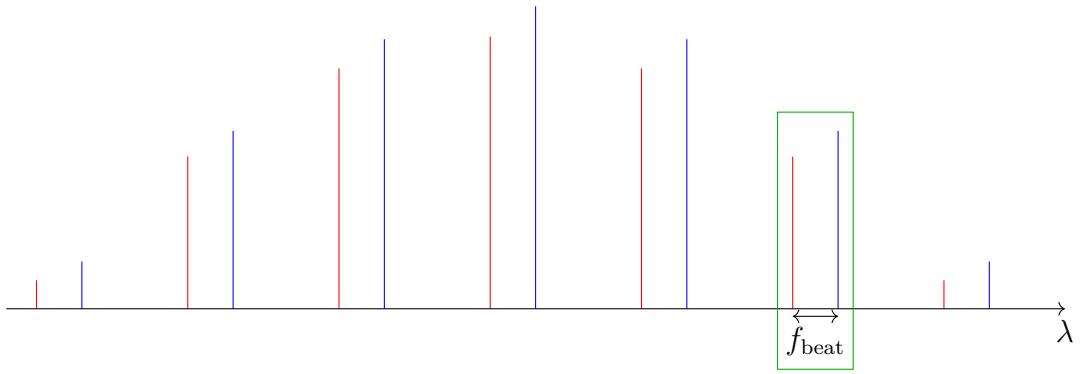

Figure 4.13: Turing Pattern Synchronization Optical Spectrum

better method would be to filter a few comb lines with their respective symmetrical counterpart out, insert that filtered comb into the follower one, and measure behind both combs only the previously filtered out part.

At last, the optimal way to be sure that only the light of the follower cavity is measured is to use an add-drop resonator. An add-drop resonator enables to try to couple the leader light into the follower resonator without it impairing the measurement of the follower signal's measurement appearing in the measurement of the follower cavity, resulting in proof of synchronization, once a small correlation between leader and follower is achieved, because both signals can not simply mix together.

Turing Pattern Synchronization

When trying to synchronize Turing pattern combs, a different approach than above can be applied. Let there be two different Turing pattern combs, depicted in figure 4.13 by the red and the blue comb. In this example they are shifted by a frequency f_{beat} and the power of each spectral component differs by some factor. The same approach as above is conducted to let them synchronize, but this time not the temporal signal of each comb is measured, but the temporal signal of both combs together. Optimally, one would filter out a pair of comb lines from the overlapped spectrum, marked by the green rectangle. When measuring these two spectral components, a beatnote can be measured, corresponding to f_{beat}, the frequency both combs are shifted apart from each other. If both combs were to synchronize, meaning the follower Turing pattern would align with the leader comb, the beatnote would disappear.

In comparison with the previous synchronization setup, an additional VOA is used, namely between the laser and the follower resonator to have better control over the ratio between pump and leader signal that goes into the follower resonator. Furthermore, the oscilloscope is not used, but the ESA, where both signals are first coupled together with a 3 dB coupler, filtered by a BPF, so that only one comb line pair passes through, and detected by a 5 GHz PD, that sends the electrical signal of both overlapping spectra

to the ESA.

4.2 Results and Discussion

This section covers the results and the concurrent discussion of the above described experimental setups. Each experimental setup depends on the outcome of the previous setup. That is why, both, the results and discussion, are treated in the same section.

Starting with the Q-Measurement, the resonators are described, which is followed by the MI comb characterization, or rather the chaos characterization. Then, the setup is slowly built up, where only one laser is used to pump two different cavities, which might have a higher possibility to induced synchronization in those cavities. Furthermore, as written above, the resonators are located on the same chip, minimizing the effect of fabrication deviations between different resonators. In the end, the injection setup is investigated with respect to the synchronization of two chosen resonators.

4.2.1 Q-Measurement

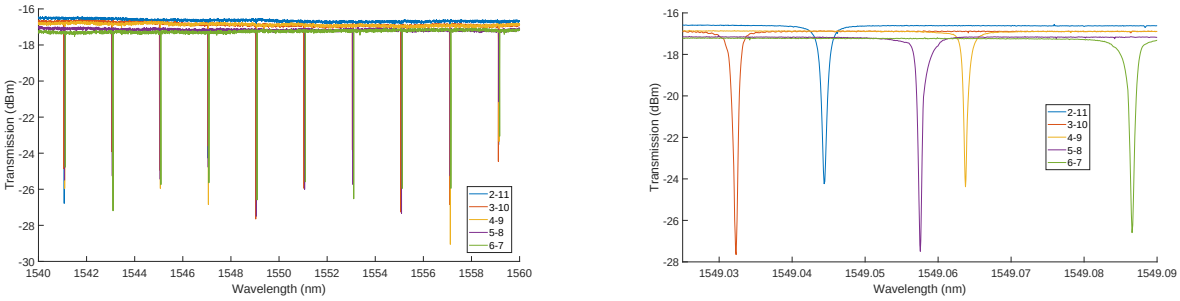

(a) Full Range (b) Middle-Resonance

Figure 4.14: Transmission Spectra for the different resonators on the chip

Conducting transmission spectrum measurements, one can quickly determine the resonance wavelengths of each resonators, and then approximate the Q-factor of the investigated resonator. In Fig. 4.14a, the transmission spectra for the five different resonators on the investigated chip can be seen. The numbers in the legend are indicating the numbers of the used fibers connected to the chip. As the measured power is plotted against the wavelength, it seems as if each resonance mode is exactly the same for the different cavities. However, looking closer to only one resonance mode and comparing that across the five resonators small differences emerge, Fig. 4.14b.

For now, it does not really matter, which cavity is chosen for the next experiment. But, when trying to synchronize the cavities, the parameters should be as close as possible to simplify the synchronization process.

4.2.2 MI Comb Characterization

In this section, the characteristics of the MI comb and its inherent chaos is investigated, to build a better comprehension. The focus lies first on the simple generation of an MI comb, from which the signal is analyzed afterwards, approximating the strange attractor of the chaotic source. Then the effects of the different FBGs and a BPF are studied.

MI Comb Generation

Similarly to the MI comb generation in Fig.4.8, the pump laser is swept to longer wavelengths, but instead of the optical spectrum, the base band in the electrical RF spectrum is analysed. Furthermore, the pump power, i.e. the output of the EDFA is varied, as each data set, meaning the received power for each frequency component, is measured. The results are shown in Fig.4.15, where the output power of the EDFA is changed from 200 mW to 1000 mW in 200 mW-steps, from the top figure to the bottom figure. As the detuning is decreased and the pump wavelength is approaching the resonance wavelength, a peak is arising. This peak moves to higher frequencies and widens, while the pump power is increased. Moreover, at a certain detuning level, sharp and noticeable peaks are emerging, which belongs to a stage between the Turing pattern and the known MI comb, which is called MI phase 1 [92]. The electrical spectrum corresponding to the smallest detuning and the highest power output of the cavity is also in good agreement with the simulation results of the chaotic base band, which validates the simulation's approach.

In the next step the chaotic output of the comb shown in figure 4.16a is analyzed. While the MI comb in this measurement has no flat-top spectrum, it still exhibits chaotic waves, which are shown in Fig. 4.16b and 4.16c, with ranges of 5 µs and 50 ns on the x-axis. The voltage from the photodetector is measured and its mean is substracted, meaning only the RF signal remains. When considering the 5 µs clipping of the temporal signal, it does look as if just amplified noise is measured. Viewing closer at the 50 ns cutout, gives a better feeling for the signal, as it does not look that much like noise.

The Analysis of this this chaotic waveform, is done by creating the attractor plots of the said signal, according to the the methodology mentioned in Chap. 3. Attractor portraits are investigated, to confirm the chaotic behavior of the temporal waveform and to find any possible strange attractor. In Fig. 4.17, the attractor is plot by shifting the data by a value ΔT which is here arbitrarily set to 0.1 ns, 1 ns and 10 ns, as seen in 4.17a, 4.17b and 4.17c, respectively. In these figures the effect of choosing the right value for ΔT becomes noticeable. The smaller the time shift is, the more the portrait

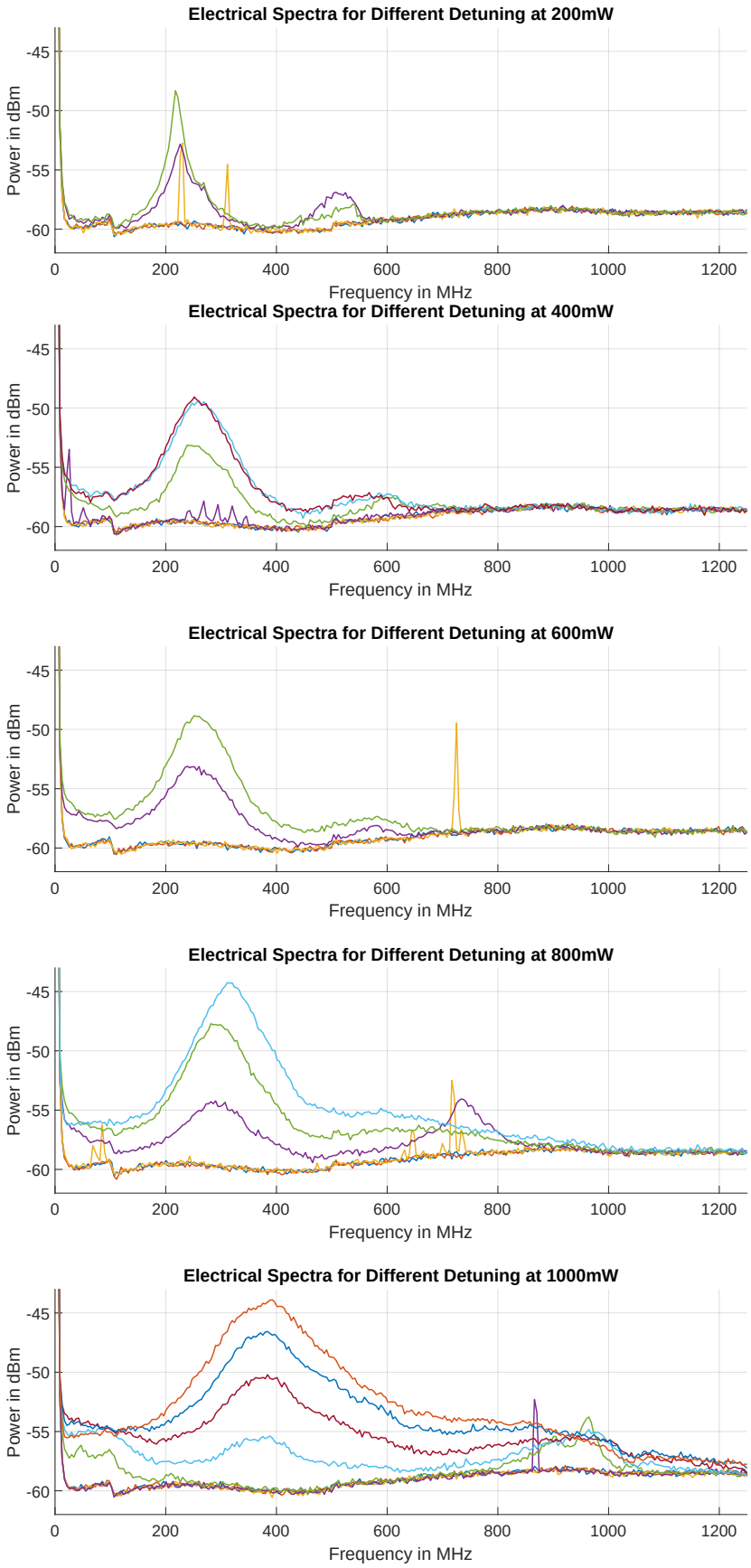

Figure 4.15: Electrical Spectra for different pump powers

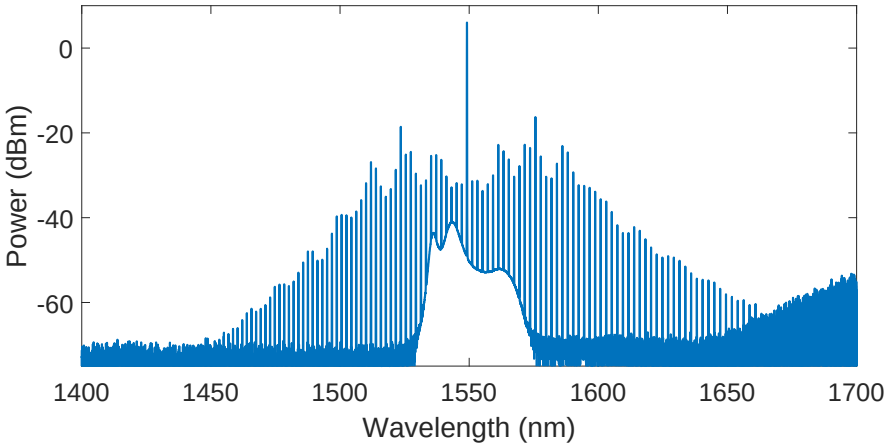

(a) MI comb that generated the waveforms

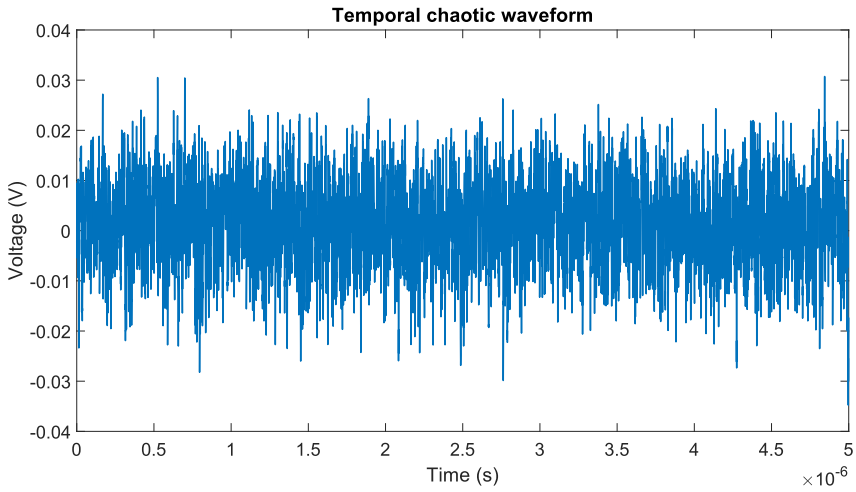

(b) 5 µs range

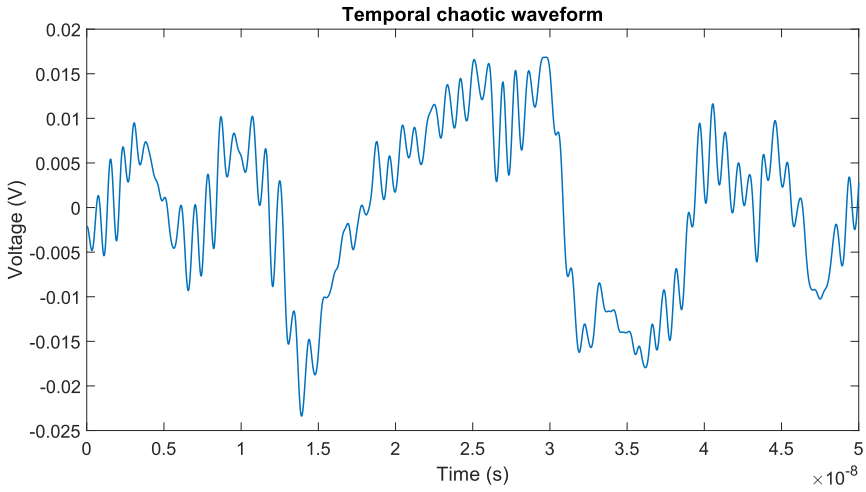

(c) 50 ns range

Figure 4.16: MI comb and its temporal chaotic waveforms, horizontal scaling differs

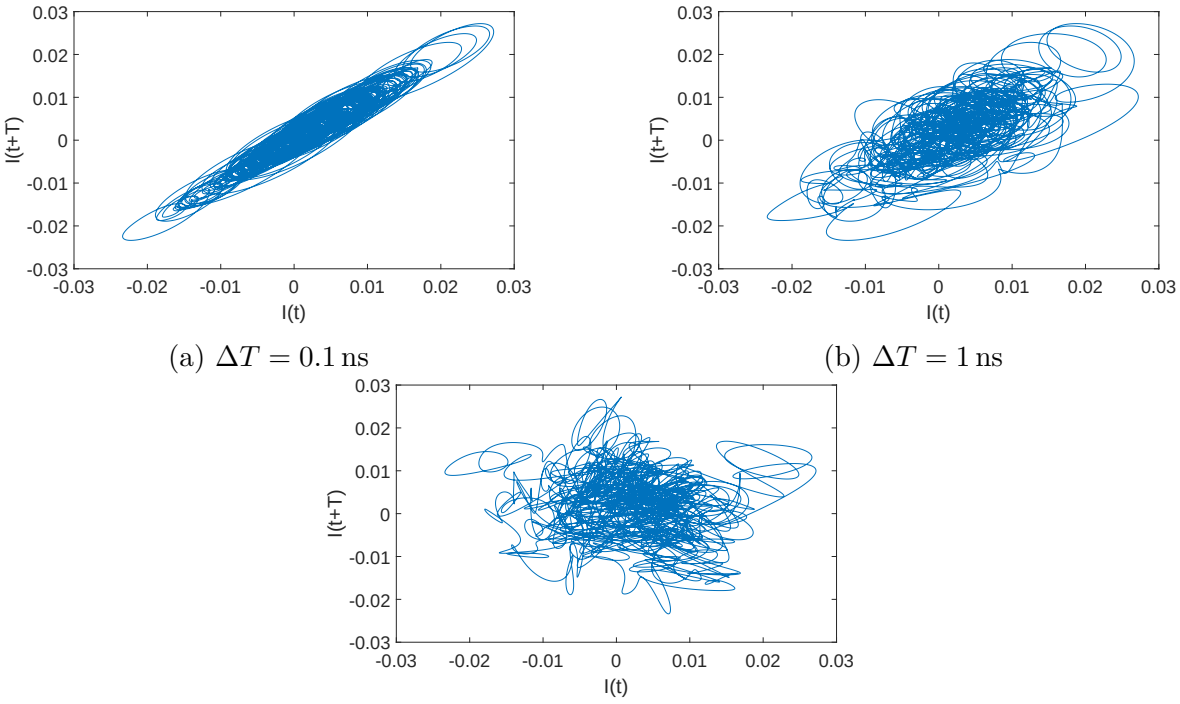

(a) $\Delta T = 0.1\,\mathrm{ns}$ (b) $\Delta T = 1\,\mathrm{ns}$

(c) $\Delta T = 10\,\mathrm{ns}$

Figure 4.17: Attractor Portraits for different ΔT

changes into a diagonal line, in correspondence to the autocorrelation function of the chaos.

To find the optimal value for ΔT that shows the highest linear independence, the mutual information of the chaotic signal is analyzed.

In Fig. 4.18, the calculated mutual information can be seen with respect to the time shift ΔT. In order to calculate the mutual information, the probability density has to be assumed which is done by sorting the measured points into a histogram. An example histogram can be seen in the inset of Fig. 4.18. According to Fraser [90], one of the minima in the mutual information has to be chosen and the corresponding ΔT value is used to shift the initial signal, to plot the attractor portrait.

Furthermore, mutual information is a measure which shows just like the the cross correlation function, how correlated two signal are. If two signals have a mutual information of 0 bit, there is nothing to be concluded over the other signal, when knowing one signal. Thus, evaluating the mutual information might be an interesting approach to proof whether synchronization between two signals is present or not, but the common procedure is to calculate the cross correlation.

The determined optimal temporal shift is $\Delta T = 1.3\,\mathrm{ns}$ and when shifting the signal by that amount, the attractor portrait as shown in Fig. 4.19 is obtained. In this attractor plot, too, no strange attractor is visible. However, even if a hint for a strange attractor is not noticable, the fact that the signal is chaotic is clearly seen. A periodic

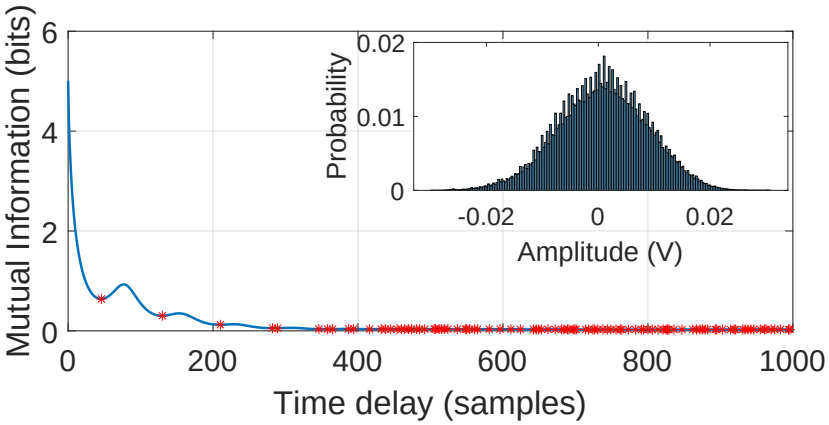

Figure 4.18: Optimization by mutual information technique [90]

signal or even a quasi-periodic signal would show a ring-shaped attractor portrait.

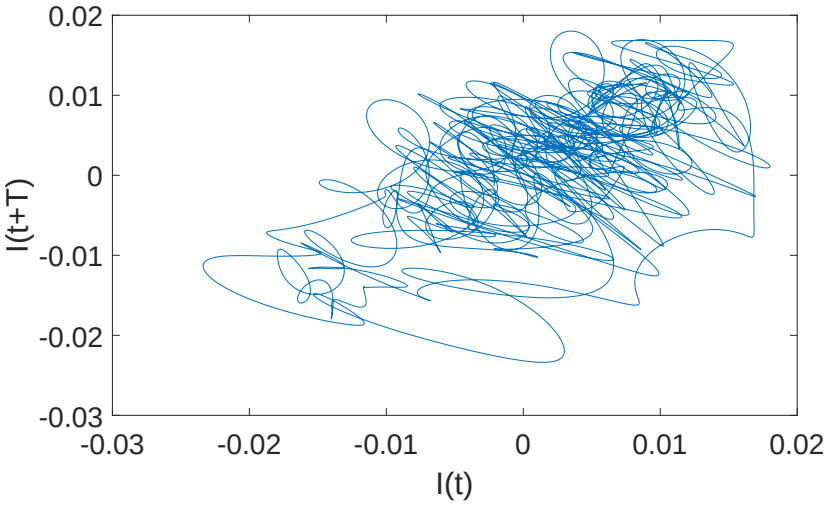

(a) 2D

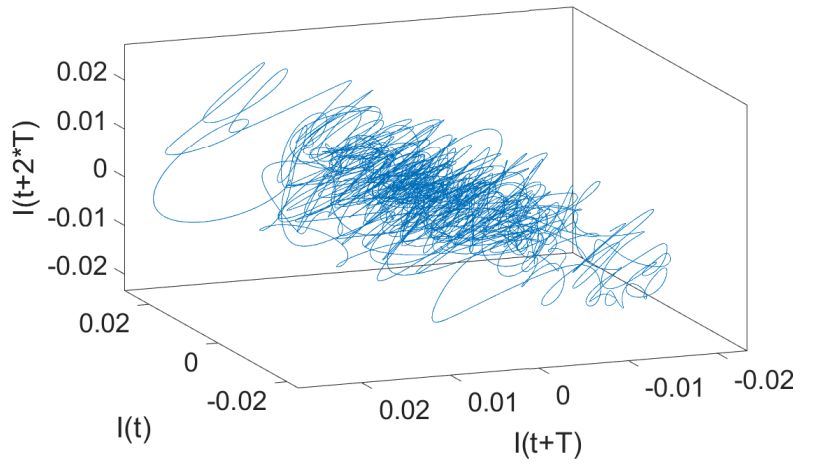

(b) 3D

Figure 4.19: With optimized $\Delta T = 1.3\,\mathrm{ns}$

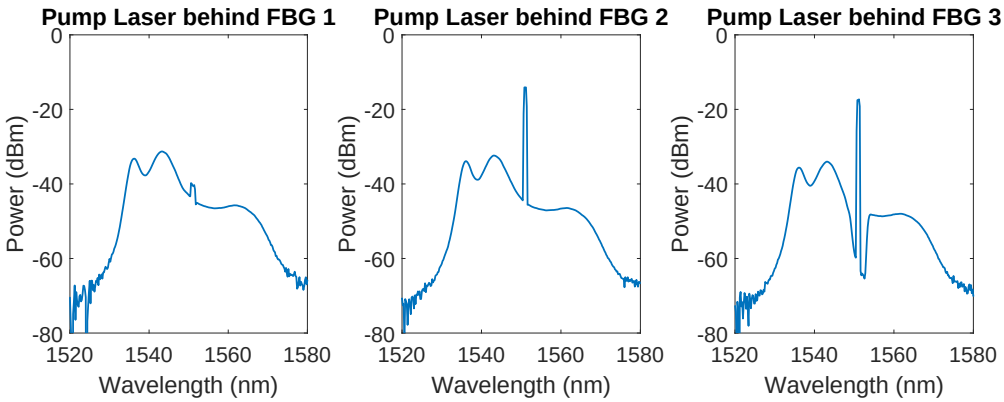

Figure 4.20: Output of the ASE noise behind each FBG

Comparing these chaotic attractors with the chaotic attractor obtained in the simulation, see above Fig. 3.6, similarities can be seen. The time delay T is in both cases determined by analysing the mutual information, which gives reason to compare both in this context. While the values on the axis are different, because the experimental values are without the DC-component of the chaotic signal, the shapes and the direction of the trajectories match the simulation. Therefore, these chaos attractors validate the simulation.

Effect of Different Fiber Bragg-Gratings on Autocorrelation

After confirming the chaotic behavior of the MI comb, in this section, the effect of different Fiber Bragg-Gratings (FBGs) on the signal is investigated. First, consider the optical spectra of the three different FBGs, shown in Fig. 4.20. All optical spectra show here the ASE noise of the EDFA in front of the cavity. The pump laser is not swept, so that no comb is generated, and no BPF is inserted between the PC and EDFA.

The figures show the blocking performance of the pump mode for the different FBGs. The first and second FBG are both variable with a small filtering-bandwidth and can be set directly onto the pump wavelength. The third FBG is fixed at 1550 nm, but has a broader blocking width, so that the pump mode is also suppressed.

For the following experiment, the first FBG, FBG 1, is chosen, as it shows the best highest and most accurate blocking performance. Now, an MI comb is generated, which can be seen in Fig. 4.21, the output of that comb is then split into two lines, and each line is investigated on its own.

The autocorrelation in front and behind the FBG can be seen in Fig. 4.22a and 4.22b, respectively. Suppressing the pump mode by the FBG seems to smooth out the autocorrelation function for higher time delays. However, despite the autocorrelation functions in front and behind the FBG look very similar, when calculating the cross

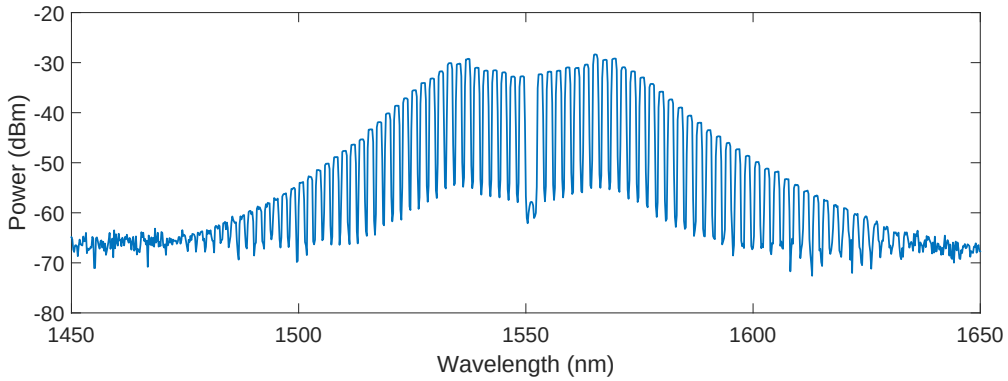

Figure 4.21: Generated MI Comb

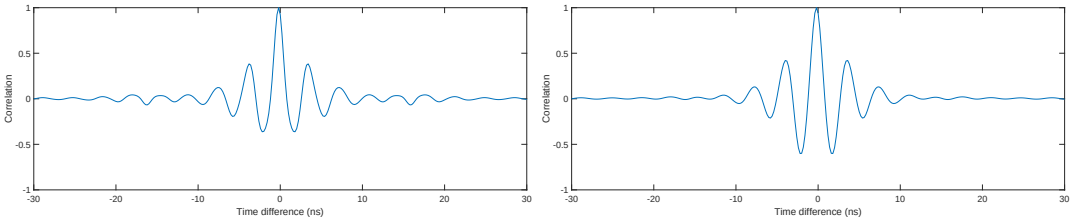

(a) Autocorrelation in front of the FBG (b) Autocorrelation behind the FBG

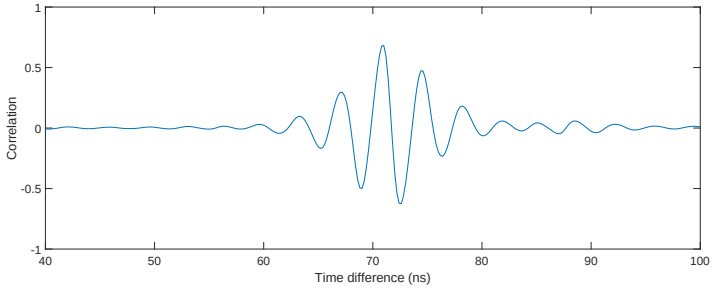

(c) Crosscorrelation between in front and behind FBG

Figure 4.22: Effect of one variable FBG on the Signal

correlation between both signal lines, the correlation decreased. So, the same signal is split, one half is transmitted through the FBG while the other half is directly measured. The cross correlation between these two signals is measured and a correlation of just around 70 % can be seen, Fig. 4.22c.

Instead of using just one FBG, two FBGs in tandem are employed. Since three different FBGs are available, two setups are studied. One setup is splitting the signal behind the cavity and transmitting the signals through each FBG. The other setup does the same, but instead of transmitting the signal through FBG 2, the second signal is transmitted through FBG 3, the one with the fixed wavelength. The results are shown in Fig. 4.23, where two characteristics are visible. The fibers connected to the second and to the third FBG are slightly differing in length. But the more important characteristic is the cross correlation between the first and second FBG as it is higher than the correlation between the first and third FBG. Therefore, in the

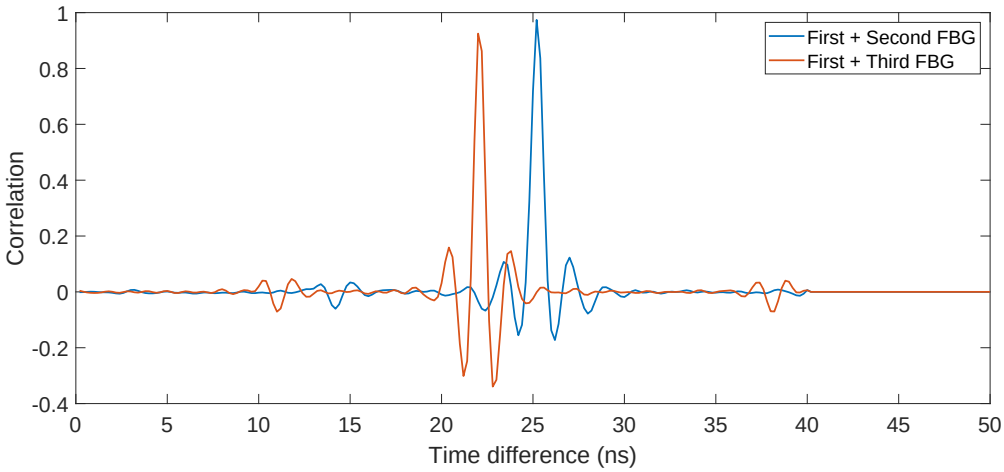

Figure 4.23: Crosscorrelation between the output of different FBGs

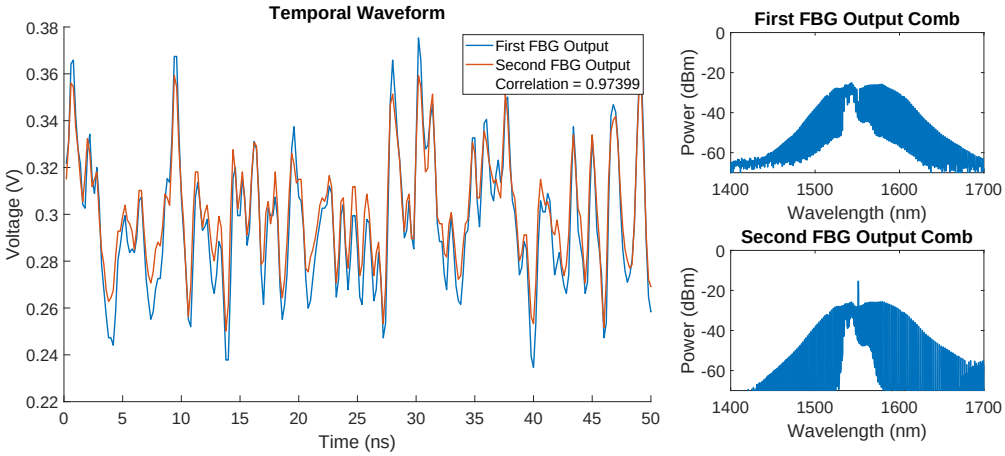

Figure 4.24: Signal Deviation between both filtered signal lines

following experiments, the first and second FBG is used. Both are variable FBG with a similar blocking behavior, which makes it comprehensible why they exhibit a higher correlation than in the case where the fixed FBG is used which block more wavelengths.

To show the concrete differences between the first and second FBG, the shifted temporal waveforms are depicted in Fig. 4.24. The right figure shows the MI comb after the respective FBG, while the figure on the left compares the temporal waveforms. Optimally, a correlation of 100 % is wanted, but in this case only a correlation of 97.4 % is determined, which is probably due to the FBGs still being different, even though they are both adjustable. Nevertheless, such a high correlation is enough, to verify synchronization later on.

Effect of a Bandpass Filter on Autocorrelation

In Fig. 4.25, the effect the BPF in front of the PC can have on the autocorrelation function, when the FWHM of the BPF is changed. While the autocorrelation function

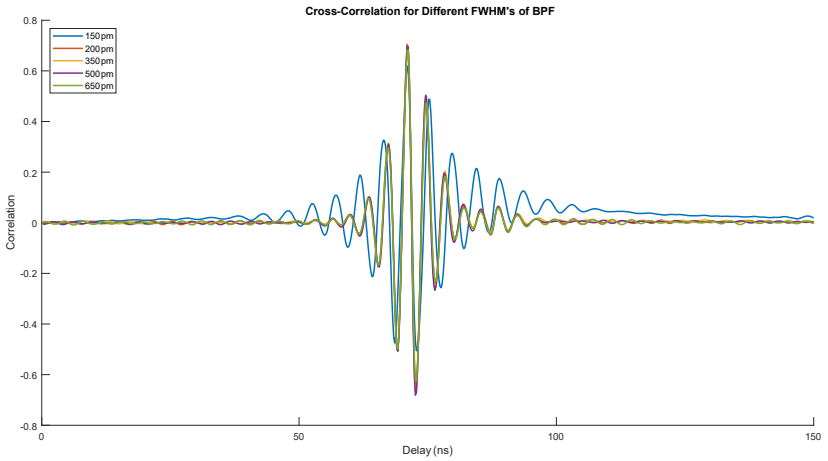

Figure 4.25: Effect of the FWHM of BPF on the autocorrelation function

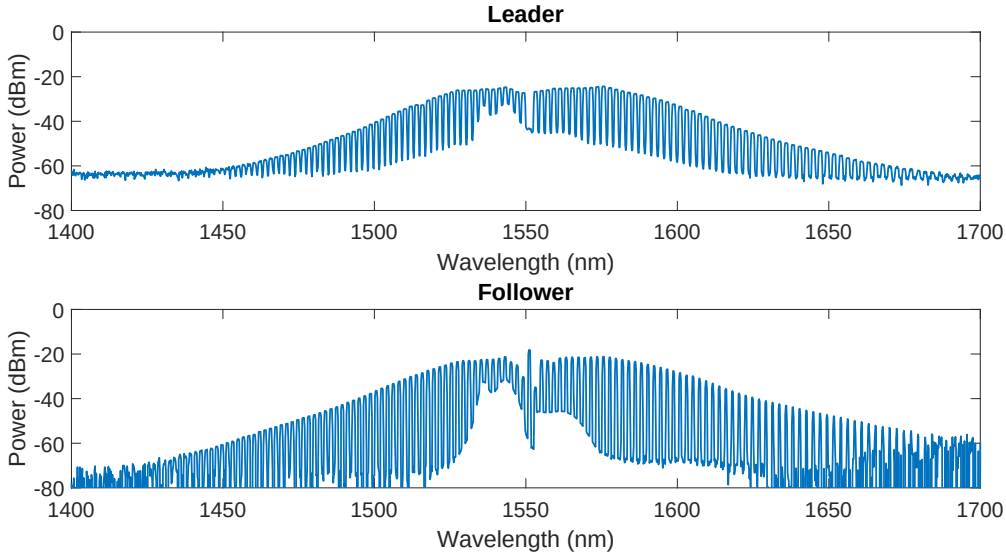

Figure 4.26: Leader and Follower Comb

is basically the same for higher FWHM of the filter function, when setting the FWHM to just 150 pm, the autocorrelation function broadens.

4.2.3 Dual MI Comb Generation

In this section, two MI combs are generated with the use of just one laser. This is not possible for any two microrings, but only for very similar ones. Previously in the Q-measurement, the resonance wavelengths of each resonator were determined. By choosing two resonators which are close to each other, it is feasible to generate two MI combs at the same time, which is shown in Fig. 4.26.

Although they are powered by the same pump laser, the emitted chaotic waveforms are completely different, which is shown in Fig. 4.27. The cross correlation function is

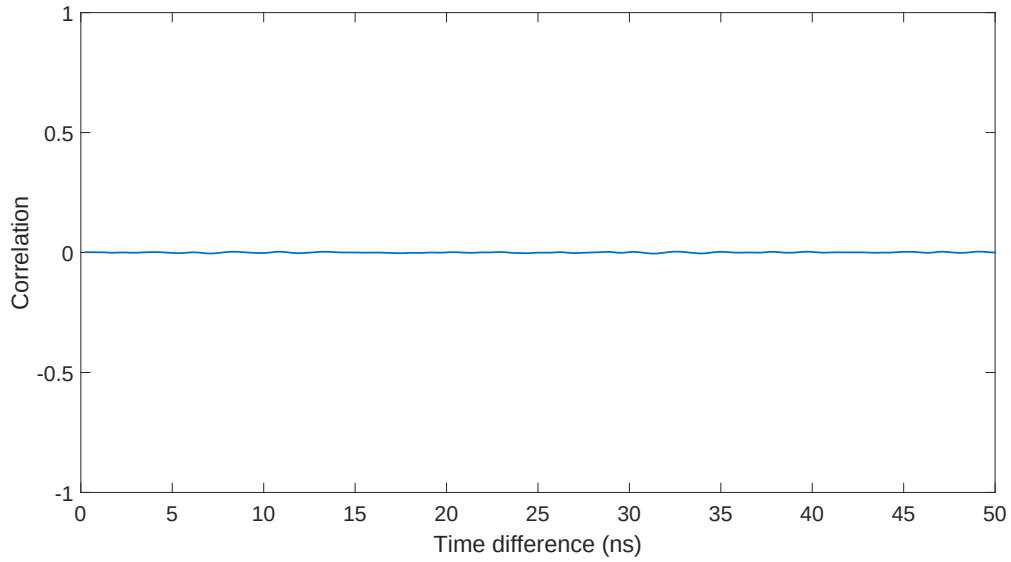

Figure 4.27: Cross correlation between Leader and Follower

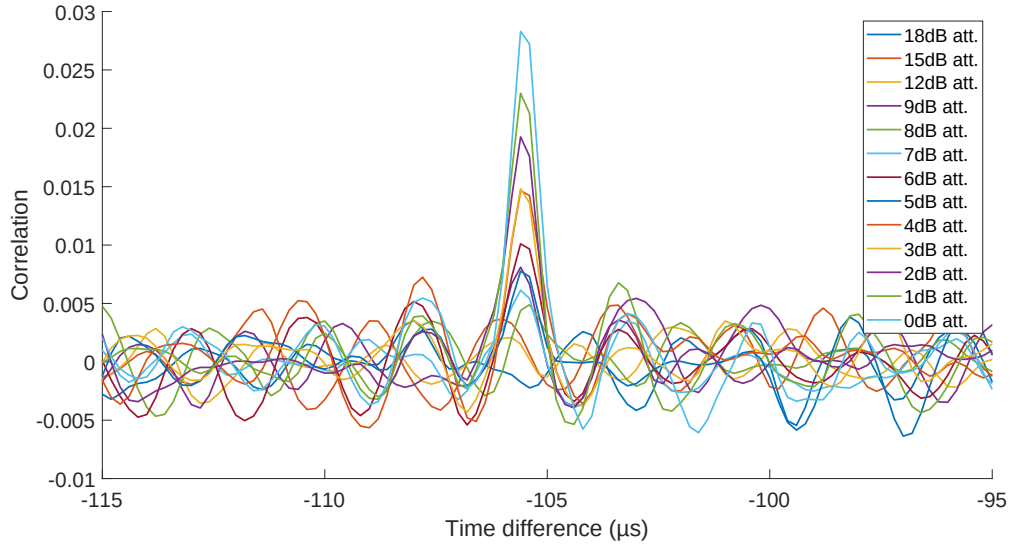

Figure 4.28: Cross correlation without amplifying the output from the leader

very close to zero at any given moment.

4.2.4 Synchronization Setup

This section is about the synchronization setup. The first setup, where the output from the first cavity is not yet amplified yielded a low correlation between the leader and the follower output. The cross correlation function can be seen in Fig. 4.28, where the attenuation between the output of the leader and the input of the follower is changed. The lower the attenuation the higher is the correlation. However, a correlation of just about 3 % is not usable.

To increase the correlation between both resonators, an EDFA is inserted between

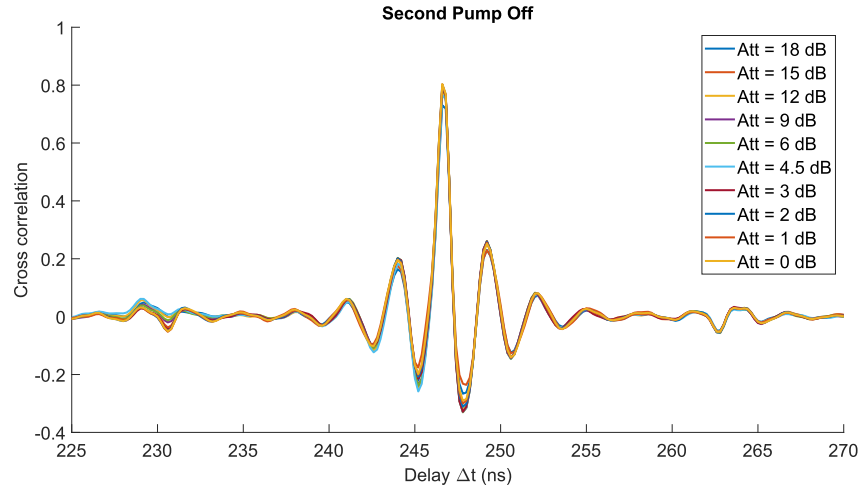

Figure 4.29: Cross correlation with amplifying the output from the leader but without pumping the second cavity

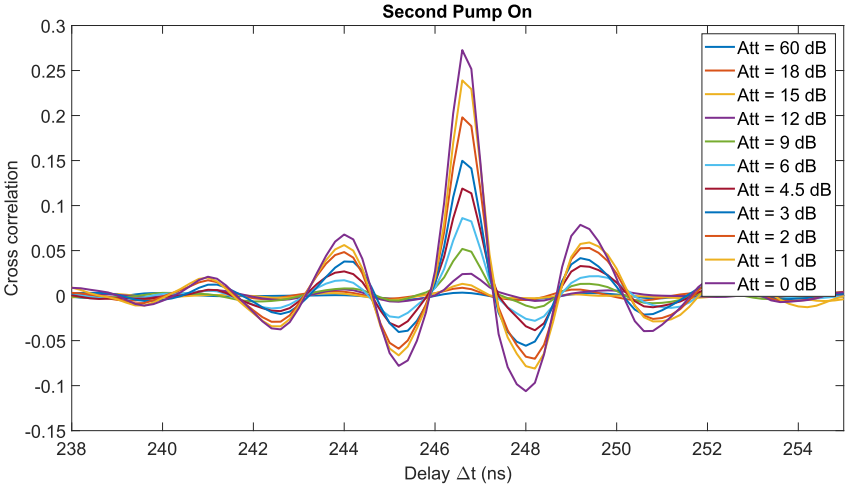

Figure 4.30: Cross correlation with amplifying the output from the leader

the output of the leader and the input of the follower ring. With that, two different settings are measured. First, as shown in Fig. 4.29, the cross-correlation when the second ring is not powered, meaning only the signal from the leader cavity, is measured as it is transmitted through the waveguide next to the follower resonator. There is no visible effect for the whole range of set attenuations between the second EDFA and the follower ring.

The second setting was pumping the follower cavity as well as generating an MI comb in it, then inputting the signal from the leader cavity into the follower cavity. And it is visible from the cross correlation in Fig. 4.30 for high attenuations, that both signals are uncorrelated. But, the more the attenuation is lowered, the higher becomes the cross correlation between leader and follower.

This might either be both signals just being mixed together or an actual partial

synchronization due to injection of the leader comb into the follower resonator.

4.2.5 Expected Correlation

In this section a formula for the expected cross-correlation of the superposition of two uncorrelated signals will be derived, in order to investigate, whether the measured cross correlation is a hint for synchronization or not. To have a measure for the cross-correlation, the sample Pearson correlation coefficient is used, but the derivation might be easier from the general Pearson correlation coefficient.

$$\rho_{xy} = \frac{\mathrm{cov}(x, y)}{\sigma_x \sigma_y} \tag{4.4}$$

where $\mathrm{cov}(x, y)$ is the covariance of signals x and y and σ_x and σ_y are the respective standard deviation. The covariance for a set of samples is defined as:

$$\mathrm{cov}(x, y) = \frac{1}{N-1} \sum_{i=1}^{N} (x_i - \overline{x})(y_i - \overline{y}) \tag{4.5}$$

where N is the number of samples in the set, and $\overline{x}$ and $\overline{y}$ are the respective means of each signal. The mean is defined as:

$$\overline{x} = \frac{1}{N} \sum_{i=1}^{N} x_i \tag{4.6}$$

Furthermore, the standard deviation of a sample is defined as:

$$\sigma_x = \sqrt{\frac{1}{N-1} \sum_{i=1}^{N} (x_i - \overline{x})^2} \tag{4.7}$$

When inserting 4.5 into 4.4, the sample Pearson correlation coefficient can be obtained:

$$r_{xy} = \frac{1}{N-1} \frac{\sum_{i=1}^{N} (x_i - \overline{x})(y_i - \overline{y})}{\sigma_x \sigma_y} \tag{4.8}$$

Which simplifies to

$$r_{xx} = \frac{1}{N-1} \frac{\sum_{i=1}^{N} (x_i - \overline{x})^2}{\sigma_x^2} \tag{4.9}$$

when the auto-correlation is calculated. Now, let a third signal, z, be the weighted superposition of signals x and y.

$$z = \alpha x + \beta y \tag{4.10}$$

To simplify the calculation, the weights are normalized to $\alpha + \beta = 1$. Additionally, it is required that signals x and y are uncorrelated. Which means, that the covariance disappears, $\text{cov}(x, y) = 0$, resulting in:

$$\sum_{i=1}^{N}(x_i - \overline{x})(y_i - \overline{y}) = 0 \tag{4.11}$$

Lastly, the linearity of the mean is required:

$$\overline{\alpha x + \beta y} = \sum_{i=1}^{N} \alpha x_i + \beta y_i = \sum_{i=1}^{N} \alpha x_i + \sum_{i=1}^{N} \beta y_i = \alpha \sum_{i=1}^{N} x_i + \beta \sum_{i=1}^{N} y_i = \alpha\overline{x} + \beta\overline{y} \tag{4.12}$$

To calculate the cross-correlation between x and z, the above reviewed sample Pearson correlation coefficient 4.8 is used and the signals are inserted.

$$r_{xz} = \frac{1}{N-1} \frac{\sum_{i=1}^{N}(x_i - \overline{x})(z_i - \overline{z})}{\sigma_x \sigma_z} \tag{4.13}$$

Knowing the signal z is the weighted superposition of x and y, 4.10, the cross-correlation r_{xz} can be expressed in terms of x, y and the standard deviation of z, σ_z.

$$\begin{aligned} r_{xz} &= \frac{1}{N-1} \frac{\sum_{i=1}^{N}(x_i - \overline{x})(z_i - \overline{z})}{\sigma_x \sigma_z} \\ &= \frac{1}{N-1} \frac{\sum_{i=1}^{N}(x_i - \overline{x})((\alpha x_i + \beta y_i) - \overline{\alpha x + \beta y})}{\sigma_x \sigma_z} \end{aligned}$$

The mean of z is now simplified by the previously derived linearity of the mean 4.12.

$$\begin{aligned} r_{xz} &= \frac{1}{N-1} \frac{\sum_{i=1}^{N}(x_i - \overline{x})(\alpha x_i + \beta y_i - \overline{\alpha x} - \overline{\beta y})}{\sigma_x \sigma_z} \\ &= \frac{1}{N-1} \frac{\sum_{i=1}^{N}(x_i - \overline{x})(\alpha x_i - \overline{\alpha x})}{\sigma_x \sigma_z} + \frac{1}{N-1} \frac{\sum_{i=1}^{N}(x_i - \overline{x})(\beta y_i - \overline{\beta y})}{\sigma_x \sigma_z} \\ &= \frac{1}{N-1} \frac{\sum_{i=1}^{N}(x_i - \overline{x})(\alpha x_i - \alpha\overline{x})}{\sigma_x \sigma_z} + \frac{1}{N-1} \frac{\sum_{i=1}^{N}(x_i - \overline{x})(\beta y_i - \beta\overline{y})}{\sigma_x \sigma_z} \\ &= \frac{\alpha}{N-1} \frac{\sum_{i=1}^{N}(x_i - \overline{x})(x_i - \overline{x})}{\sigma_x \sigma_z} + \frac{\beta}{N-1} \frac{\sum_{i=1}^{N}(x_i - \overline{x})(y_i - \overline{y})}{\sigma_x \sigma_z} \end{aligned}$$

With the requirement that the signals x and y are uncorrelated, 4.11, one of the addends disappears.

$$\begin{aligned} r_{xz} &= \frac{\alpha}{N-1}\frac{\sum_{i=1}^{N}(x_i-\overline{x})(x_i-\overline{x})}{\sigma_x\sigma_z} + \frac{\beta}{N-1}\frac{\overbrace{\sum_{i=1}^{N}(x_i-\overline{x})((y_i)-\overline{y})}^{=0}}{\sigma_x\sigma_z} \\ &= \frac{\alpha}{N-1}\frac{\sum_{i=1}^{N}(x_i-\overline{x})(x_i-x)}{\sigma_x\sigma_z}\frac{\sigma_x}{\sigma_x} \\ &= \alpha\underbrace{\frac{1}{N-1}\frac{\sum_{i=1}^{N}(x_i-\overline{x})^2}{\sigma_x^2}}_{r_{xx}}\frac{\sigma_x}{\sigma_z} \\ &= \alpha\frac{\sigma_x}{\sigma_z}r_{xx} \end{aligned}$$

Thus, the cross-correlation can be expressed as the ratio of the respective standard deviation of x and z multiplied with the factor α, and dependent on the auto-correlation function of x. Now, the standard deviation of the superimposed signal, σ_z has to be calculated in terms of the standard deviation of signal x, σ_x. Again, with 4.10

$$\begin{aligned} \sigma_z^2 &= \frac{1}{N-1}\sum_{i=1}^{N}(z_i-\overline{z})^2 \\ &= \frac{1}{N-1}\sum_{i=1}^{N}((\alpha x_i+\beta y_i)-\overline{\alpha x+\beta y})^2 \end{aligned}$$

and the linearity of the mean, 4.12, the formula can be similarly rearranged.

$$\begin{aligned} \sigma_z^2 &= \frac{1}{N-1}\sum_{i=1}^{N}((\alpha x_i+\beta y_i)-\overline{\alpha x+\beta y})^2 \\ &= \frac{1}{N-1}\sum_{i=1}^{N}(\alpha(x_i-\overline{x})+\beta(y_i-\overline{y}))^2 \end{aligned}$$

When applying the binomial theorem, the requirement 4.11 can be employed and reduces the equation to two addends.

$$\sigma_z^2 = \frac{1}{N-1}\sum_{i=1}^{N}\alpha^2(x_i-\overline{x})^2+\beta^2(y_i-\overline{y})^2+2\alpha\beta\underbrace{(x_i-\overline{x})(y_i-\overline{y})}_{=0}$$

After extracting α and β from the sums, the definition for the standard deviation, 4.7, is applied, so that a simple relation is left.

$$\begin{aligned}\sigma_z^2 &= \frac{1}{N-1}\sum_{i=1}^{N}\alpha^2(x_i-\overline{x})^2 + \frac{1}{N-1}\sum_{i=1}^{N}\beta^2(y_i-\overline{y})^2 \\ &= \alpha^2\frac{1}{N-1}\sum_{i=1}^{N}(x_i-\overline{x})^2 + \beta^2\frac{1}{N-1}\sum_{i=1}^{N}(y_i-\overline{y})^2 \\ &= \alpha^2\sigma_x^2 + \beta^2\sigma_y^2\end{aligned}$$

With this expression for σ_z we get the cross-correlation, r_{xz}, that only depends on the values of signals x and y, enabling the calculation of the correlation in case of both signals being ideally mixed together.

$$r_{xz} = \alpha\frac{\sigma_x}{\sigma_z}r_{xx} = \alpha\frac{\sigma_x}{\sqrt{\alpha^2\sigma_x^2+\beta^2\sigma_y^2}}r_{xx} \tag{4.14}$$

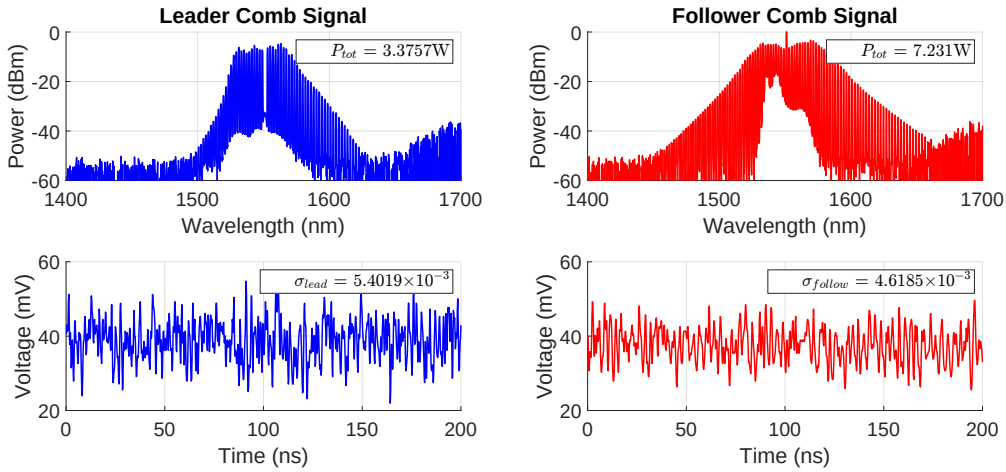

Figure 4.31: Spectra and temporal waveforms measured behind the follower ring

Utilizing measurements from the setup, Fig. 4.12b, the respective standard deviation the factors α and β are calculated to be inserted in the above derived formula. In order to calculate the factors α and β, it is assumed that the leader signal has no effect on the ring resonator and two cases are investigated to measure the respective Power. First, the leader comb is transmitted through the waveguide which is adjacent to the follower resonator, while the pump to the follower is turned off. This can be seen in Fig. 4.31 on the left side, where the upper graph shows the comb signal of the leader resonator measured behind the follower ring. And the lower graph is the recorded temporal signal, also behind the follower resonator. The spectrum can then be used to calculated the power of the leader which is arrives behind the follower ring, and the temporal waveform to calculate the standard deviation.

Second, the leader comb is blocked and a simple MI comb is generated in the follower ring, which can be seen on the right side of Fig. 4.31. The temporal signal of the follower comb is seen below the spectrum. These data sets are used to calculate the power and the standard deviation, respectively. Knowing the power of each comb, enables the calculation of the factors α and β:

$$\alpha = \frac{P_L}{P_L + P_F} = 0.31 \tag{4.15}$$

$$\beta = \frac{P_F}{P_L + P_F} = 0.69, \tag{4.16}$$

where P_L and P_F are the powers in of the leader and the follower comb, measured behind the follower ring, respectively.

Thus, the standard deviation of the mixed signal evaluates to:

$$\sigma_{mix} = \sqrt{\alpha^2\sigma_L^2 + \beta^2\sigma_F^2} = 3.6 \times 10^{-3}, \tag{4.17}$$

where σ_L and σ_F are the standard deviations of the previously measured temporal signals in Fig. 4.31 for the leader and follower comb, respectively.

Finally, the expected maximum correlation between two signals which are ideally mixed together is evaluated according to Eq. 4.14:

$$r_{mix} = \alpha\frac{\sigma_x}{\sigma_{mix}} = 46.32\% \tag{4.18}$$

The expected correlation, when both signals are just mixed together, is higher than the highest measured correlation value in Fig. 4.30, which is just around 27%. Hence, not even partial synchronization was achieved. But to end on a positive note, with this formula, a minimum limit is set which has to be overcome, in order to show chaos synchronization.

5 Summary & Outlook

5.1 Simulation

Utilizing the Lugiato-Levefer equations, microresonator rings were simulated in different setups. A chaotic attractor was determined by employing the minimum of mutual information function depending on the difference time delay between original and shifted signal. Simulating two microrings on their own without being connected, demonstrated the uncorrelatedness of the fields emitted by the rings. When the leader resonator's output is injected into the follower resonator by choosing the correct injection parameter and controlling the follower resonator with a suitable pump power, while keeping all other parameters the same for both resonators, synchronization of both fields inside the rings was observed. Furthermore, an analysis of chosen parameters took place, where the parameters of the follower ring were investigated, that showed insightful conditions for the synchronization. Finally, the effect of noise in the transmission line was investigated, our model shows a high robustness against external noise, which the transmission line might be prone to.

5.2 Experiment

In the experimental part, an array of the same resonators was used, which were all fabricated on the same chip. First analysis revealed that the resonator exhibits a similar chaotic attractor as the simulation, which validates the simulation results. The single resonator was also used to examine the base band of the in the chaotic regime for different pump powers when lowering the effective detuning. That revealed what effect the pump power has on the chaotic spectrum, where the bandwidth is broadened with an increasing pump power. In order to proof synchronization once high correlation is achieved, the equipment's effect on the correlation was analyzed, where the same chaotic signal was split and injected into different FBGs, which showed that they worsened the correlation. However, the worsening is marginal when using FBGs that are similar to each other. Then, similarly to the simulation an experiment generating MI combs in two resonators on the same chip was conducted. It revealed, that even though both resonators were on the same chip next to each other and pumped by the same laser at the same time, the spectra were different and the cross correlation function of the emitted temporal signals was 0 over the recorded time. To increase the chance of seeing synchronization in the two microresonators, the output of the leader resonator was injected into the follower resonator with a variable attenuator

in between, to adjust the injected power. However, contrary to the simulation, no synchronization was achieved, hinting the presence of parameter that might have an effect on the synchronization but is not taken into account in the simulation. Even when there is no comb generated in the follower comb, the transmitted leader comb is not injected into the follower comb, although the simulation suggests otherwise. In the end, a proof is delivered to give a measure for the minimum cross correlation which has to be achieved in order to have evidence for synchronization.

5.3 Outlook

Questions still remain. A concrete analysis with respect to the proposed chaos secure communication protocol has to be conducted in order to proof the assumptions made numerically. Experimentally, it was already shown that one can not simply take the same microresonator, let the other chaotic signal be injected into it and hope for synchronization, which suggests the presence of a parameter that is not implemented in the simulation. To note, in the simulation, both rings were pumped by different pump lasers and still achieved synchronization.

One of the biggest challenges, and what might be the reason for not being able to synchronize both rings, is the setting of the lights polarization. As the comb generation and the coupling into the rings strongly depends on the polarization of the incoming light, it is crucial to inject correctly TE-polarized light into each cavity, which is difficult in the current approach. Therefore, employing a chip which maintains the polarization and using only devices which maintain the polarization between the resonators, might help to achieve better injection of the leader comb into the follower ring.

Once high correlation in the experiment is reached, different approaches can be utilized to proof that the high correlation is caused by chaos synchronization. Right now, it might not be clear whether the signal behind the follower ring is the actual output of the follower or the output of the leader ring, since both rings are cascaded. Therefore, employing add-drop resonators to filter the leaders signal out would solve this problem. Another way to proof synchronization could be achieved by injecting for example only the first half of the spectrum (every wavelength smaller than the pump wavelength) into the follower ring and measuring the latter half (every wavelength longer than the pump wavelength) of both resonators spectra.

As synchronization is already achieved numerically, the application of chaos communication could be implemented and analyzed numerically. The actual bandwidth for chaos communications using two cascaded microring resonators should be estimated using a simulation approach.

Achievements

International Conferences

- **ALPS**: Lemcke, D., Moreno, D., Fujii, S., Nakashima, A., Uchida, A., Tanabe, T. (2023, April 18-21). Evaluation of Chaos Synchronization in Two Cascaded Microresonators[Poster presentation, ALPSp2-32]. The 12th Advanced Lasers and Photon Sources (ALPS2023), Yokohama, Japan
- **CLEO-EU**: Lemcke, D., Moreno, D., Fujii, S., Nakashima, A., Uchida, A., Tanabe, T. (2023, June 26-30). Assessment of the Feasibility of Employing Chaos Synchronization in Two Cascaded Microresonators for Secure Data Transmission[Poster presentation, CD-P.17], CLEO/Europe, Munich, Germany, [85]
- **CLEO**: Lemcke, D., Moreno, D., Fujii, S., Nakashima, A., Uchida, A., Tanabe, T. (2024, May 05-10). Study on Chaos Synchronization of Cascaded Microresonator Optical Frequency Combs[Pending], CLEO, Charlotte, North Carolina, USA

Domestic Conference

- **JSAP**: Lemcke, D., Moreno, D., Fujii, S., Nakashima, A., Uchida, A., Tanabe, T. (2023, March 15-18). Analysis of Chaos Synchronization of Microresonator Frequency Combs[Conference presentation, 15a-A305-6]. The 70th JSAP Spring Meeting 2023, Tokyo, Japan

Co-Authored Paper

- Moreno, D., Fujii, S., Nakashima, A., Lemcke, D., Uchida, A., Sanchis, P., Tanabe, T., Synchronization of microresonator frequency combs in chaotic regime, Optics Express 32, 2024, Jan, Nr.2, 2460-2472 [84]

List of Figures

List of Tables

Bibliography

[1] Udem, T. ; Reichert, J. ; Holzwarth, R. ; Hänsch, T. W.: Accurate measurement of large optical frequency differences with a mode-locked laser. In: *Optics Letters* 24 (1999), Nr. 13, 881-883. http://dx.doi.org/Doi10.1364/Ol.24.000881. – DOI Doi 10.1364/Ol.24.000881. – ISSN 0146–9592. – 212pp Times Cited:327 Cited References Count:14

[2] Jones, D. J. ; Diddams, S. A. ; Ranka, J. K. ; Stentz, A. ; Windeler, R. S. ; Hall, J. L. ; Cundiff, S. T.: Carrier-envelope phase control of femtosecond mode-locked lasers and direct optical frequency synthesis. In: *Science* 288 (2000), Nr. 5466, 635-639. http://dx.doi.org/DOI10.1126/science.288.5466.635. – DOI DOI 10.1126/science.288.5466.635. – ISSN 0036–8075. – 308rr Times Cited:2085 Cited References Count:27

[3] Hänsch, T. W.: Nobel Lecture:: Passion for precision. In: *Reviews of Modern Physics* 78 (2006), Nr. 4, 1297-1309. http://dx.doi.org/10.1103/RevModPhys.78.1297. – DOI 10.1103/RevModPhys.78.1297. – ISSN 0034–6861. – 112pm Times Cited:579 Cited References Count:90

[4] Hall, J. L.: Nobel Lecture: Defining and measuring optical frequencies. In: *Reviews of Modern Physics* 78 (2006), Nr. 4, 1279-1295. http://dx.doi.org/10.1103/RevModPhys.78.1279. – DOI 10.1103/RevModPhys.78.1279. – ISSN 0034–6861. – 112pm Times Cited:394 Cited References Count:57

[5] Fortier, T. ; Baumann, E.: 20 years of developments in optical frequency comb technology and applications (vol 2, 153, 2019). In: *Communications Physics* 3 (2020), Nr. 1. http://dx.doi.org/ARTN8510.1038/s42005-020-0358-7. – DOI ARTN 85 10.1038/s42005–020–0358–7. – ISSN 2399–3650. – Qi8vn Times Cited:6 Cited References Count:2

[6] Delva, P. ; Lodewyck, J. ; Bilicki, S. ; Bookjans, E. ; Vallet, G. ; Le Targat, R. ; Pottie, P. E. ; Guerlin, C. ; Meynadier, F. ; Le Poncin-Lafitte, C. ; Lopez, O. ; Amy-Klein, A. ; Lee, W. K. ; Quintin, N. ; Lisdat, C. ; Al-Masoudi, A. ; Dörscher, S. ; Grebing, C. ; Grosche, G. ; Kuhl, A. ; Raupach, S. ; Sterr, U. ; Hill, I. R. ; Hobson, R. ; Bowden, W. ; Kronjäger, J. ; Marra, G. ; Rolland, A. ; Baynes, F. N. ; Margolis, H. S. ; Gill, P.: Test of Special Relativity Using a Fiber Network of Optical Clocks. In: *Physical Review Letters* 118 (2017), Nr.

22. http://dx.doi.org/ARTN22110210.1103/PhysRevLett.118.221102. – DOI ARTN 221102 10.1103/PhysRevLett.118.221102. – ISSN 0031–9007. – Ew7hx Times Cited:133 Cited References Count:43

[7] Schulz, S. ; Grguras, I. ; Behrens, C. ; Bromberger, H. ; Costello, J. T. ; Czwalinna, M. K. ; Felber, M. ; Hoffmann, M. C. ; Ilchen, M. ; Liu, H. Y. ; Mazza, T. ; Meyer, M. ; Pfeiffer, S. ; Predki, P. ; Schefer, S. ; Schmidt, C. ; Wegner, U. ; Schlarb, H. ; Cavalieri, A. L.: Femtosecond all-optical synchronization of an X-ray free-electron laser. In: *Nature Communications* 6 (2015). http://dx.doi.org/ARTN593810.1038/ncomms6938. – DOI ARTN 5938 10.1038/ncomms6938. – ISSN 2041–1723. – Ca2mo Times Cited:145 Cited References Count:51

[8] Millo, J. ; Boudot, R. ; Lours, M. ; Bourgeois, P. Y. ; Luiten, A. N. ; Le Coq, Y. ; Kersalé, Y. ; Santarelli, G.: Ultra-low-noise microwave extraction from fiber-based optical frequency comb. In: *Optics Letters* 34 (2009), Nr. 23, 3707-3709. http://dx.doi.org/Doi10.1364/Ol.34.003707. – DOI Doi 10.1364/Ol.34.003707. – ISSN 0146–9592. – 526gi Times Cited:107 Cited References Count:18

[9] Probst, R. A. ; Lo Curto, G. ; Avila, G. ; Brucalassi, A. ; Martins, B. L. C. ; Leao, I. D. ; Esposito, M. ; Hernández, J. I. G. ; Grupp, F. ; Hänsch, T. W. ; Holzwarth, R. ; Kellermann, H. ; Kerber, F. ; Mandel, O. ; Manescau, A. ; Pasquini, L. ; Pozna, E. ; Rebolo, R. ; Medeiros, J. R. ; Stark, S. P. ; Steinmetz, T. ; Mascareño, A. S. ; Udem, T. ; Urrutia, J. ; Wu, Y. J.: Relative stability of two laser frequency combs for routine operation on HARPS and FOCES. In: *Ground-Based and Airborne Instrumentation for Astronomy Vi* 9908 (2016). http://dx.doi.org/Artn99086410.1117/12.2231434. – DOI Artn 990864 10.1117/12.2231434. – ISSN 0277–786x. – Bg7nf Times Cited:22 Cited References Count:20 Proceedings of SPIE

[10] Glenday, A. G. ; Li, C. H. ; Langellier, N. ; Chang, G. Q. ; Chen, L. J. ; Furesz, G. ; Zibrov, A. A. ; Kärtner, F. ; Phillips, D. F. ; Sasselov, D. ; Szentgyorgyi, A. ; Walsworth, R. L.: Operation of a broadband visible-wavelength astro-comb with a high-resolution astrophysical spectrograph. In: *Optica* 2 (2015), Nr. 3, 250-254. http://dx.doi.org/10.1364/Optica.2.000250. – DOI 10.1364/Optica.2.000250. – ISSN 2334–2536. – Ci6ke Times Cited:48 Cited References Count:22

[11] Minoshima, K. ; Matsumoto, H.: High-accuracy measurement of 240-m distance in an optical tunnel by use of a compact femtosecond laser. In: *Applied*

Optics 39 (2000), Nr. 30, 5512-5517. http://dx.doi.org/Doi10.1364/Ao.39.005512. – DOI Doi 10.1364/Ao.39.005512. – ISSN 1559–128x. – 364zv Times Cited:383 Cited References Count:10

[12] Coddington, I. ; Swann, W. C. ; Nenadovic, L. ; Newbury, N. R.: Rapid and precise absolute distance measurements at long range. In: *Nature Photonics* 3 (2009), Nr. 6, 351-356. http://dx.doi.org/10.1038/Nphoton.2009.94. – DOI 10.1038/Nphoton.2009.94. – ISSN 1749–4885. – 452mk Times Cited:689 Cited References Count:50

[13] Schliesser, A. ; Brehm, M. ; Keilmann, F. ; Weide, D. W. d.: Frequency-comb infrared spectrometer for rapid, remote chemical sensing. In: *Optics Express* 13 (2005), Nr. 22, 9029-9038. http://dx.doi.org/Doi10.1364/Opex.13.009029. – DOI Doi 10.1364/Opex.13.009029. – ISSN 1094–4087. – 979xe Times Cited:276 Cited References Count:19

[14] Faist, J. ; Villares, G. ; Scalari, G. ; Rösch, M. ; Bonzon, C. ; Hugi, A. ; Beck, M.: Quantum Cascade Laser Frequency Combs. In: *Nanophotonics* 5 (2016), Nr. 2, 272-291. http://dx.doi.org/10.1515/nanoph-2016-0015. – DOI 10.1515/nanoph–2016–0015. – ISSN 2192–8606. – Sp. Iss. SI Dp6jh Times Cited:133 Cited References Count:86

[15] Gaeta, A. L. ; Lipson, M. ; Kippenberg, T. J.: Photonic-chip-based frequency combs. In: *Nature Photonics* 13 (2019), Nr. 3, 158-169. http://dx.doi.org/10.1038/s41566-019-0358-x. – DOI 10.1038/s41566–019–0358–x. – ISSN 1749–4885. – Hm2xb Times Cited:523 Cited References Count:159

[16] Gaafar, M. A. ; Rahimi-Iman, A. ; Fedorova, K. A. ; Stolz, W. ; Rafailov, E. U. ; Koch, M.: Mode-locked semiconductor disk lasers. In: *Advances in Optics and Photonics* 8 (2016), Nr. 3, 370-400. http://dx.doi.org/10.1364/Aop.8.000370. – DOI 10.1364/Aop.8.000370. – ISSN 1943–8206. – Dy1cc Times Cited:45 Cited References Count:136

[17] Link, S. M. ; Klenner, A. ; Mangold, M. ; Zaugg, C. A. ; Golling, M. ; Tilma, B. W. ; Keller, U.: Dual-comb modelocked laser. In: *Optics Express* 23 (2015), Nr. 5, 5521-5531. http://dx.doi.org/10.1364/Oe.23.005521. – DOI 10.1364/Oe.23.005521. – ISSN 1094–4087. – Cd2bl Times Cited:99 Cited References Count:31

[18] Hugi, A. ; Villares, G. ; Blaser, S. ; Liu, H. C. ; Faist, J.: Mid-infrared frequency comb based on a quantum cascade laser. In: *Nature* 492 (2012), Nr.

7428, 229-233. http://dx.doi.org/10.1038/nature11620. – DOI 10.1038/nature11620. – ISSN 0028–0836. – 053gm Times Cited:540 Cited References Count:30

[19] Sterczewski, L. A. ; Westberg, J. ; Yang, Y. ; Burghoff, D. ; Reno, J. ; Hu, Q. ; Wysocki, G.: Terahertz hyperspectral imaging with dual chip-scale combs. In: *Optica* 6 (2019), Nr. 6, 766-771. http://dx.doi.org/10.1364/Optica.6.000766. – DOI 10.1364/Optica.6.000766. – ISSN 2334–2536. – Ie1oj Times Cited:56 Cited References Count:39

[20] Carlson, D. R. ; Hickstein, D. D. ; Zhang, W. ; Metcalf, A. J. ; Quinlan, F. ; Diddams, S. A. ; Papp, S. B.: Ultrafast electro-optic light with subcycle control. In: *Science* 361 (2018), Nr. 6409, 1358-1362. http://dx.doi.org/10.1126/science.aat6451. – DOI 10.1126/science.aat6451. – ISSN 0036–8075. – Sp. Iss. SI Gv5la Times Cited:95 Cited References Count:35

[21] Metcalf, A. J. ; Anderson, T. ; Bender, C. F. ; Blakeslee, S. ; Brand, W. ; Carlson, D. R. ; Cochran, W. D. ; Diddams, S. A. ; Endl, M. ; Fredrick, C. ; Halverson, S. ; Hickstein, D. D. ; Hearty, F. ; Jennings, J. ; Kanodia, S. ; Kaplan, K. F. ; Levi, E. ; Lubar, E. ; Mahadevan, S. ; Monson, A. ; Ninan, J. P. ; Nitroy, C. ; Osterman, S. ; Papp, S. B. ; Quinlan, F. ; Ramsey, L. ; Robertson, P. ; Roy, A. ; Schwab, C. ; Sigurdsson, S. ; Srinivasan, K. ; Stefansson, G. ; Sterner, D. A. ; Terrien, R. ; Wolszczan, A. ; Wright, J. T. ; Ycas, G.: Stellar spectroscopy in the near-infrared with a laser frequency comb. In: *Optica* 6 (2019), Nr. 2, 233-239. http://dx.doi.org/10.1364/Optica.6.000233. – DOI 10.1364/Optica.6.000233. – ISSN 2334–2536. – Hm1eo Times Cited:77 Cited References Count:35

[22] Savchenkov, A. A. ; Matsko, A. B. ; Ilchenko, V. S. ; Solomatine, I. ; Seidel, D. ; Maleki, L.: Tunable optical frequency comb with a crystalline whispering gallery mode resonator. In: *Physical Review Letters* 101 (2008), Nr. 9. http://dx.doi.org/ARTN09390210.1103/PhysRevLett.101.093902. – DOI ARTN 093902 10.1103/PhysRevLett.101.093902. – ISSN 0031–9007. – 348fg Times Cited:292 Cited References Count:18

[23] Del'Haye, P. ; Schliesser, A. ; Arcizet, O. ; Wilken, T. ; Holzwarth, R. ; Kippenberg, T. J.: Optical frequency comb generation from a monolithic microresonator. In: *Nature* 450 (2007), Nr. 7173, 1214-1217. http://dx.doi.org/10.1038/nature06401. – DOI 10.1038/nature06401. – ISSN 0028–0836. – 243ha Times Cited:1428 Cited References Count:30

[24] Del'Haye, P. ; Diddams, S. A. ; Papp, S. B.: Laser-machined ultra-high-Q microrod resonators for nonlinear optics. In: *Applied Physics Letters* 102 (2013), Nr. 22. http://dx.doi.org/Artn22111910.1063/1.4809781. – DOI Artn 221119 10.1063/1.4809781. – ISSN 0003–6951. – 167hh Times Cited:68 Cited References Count:44

[25] Herr, T. ; Brasch, V. ; Jost, J. D. ; Wang, C. Y. ; Kondratiev, N. M. ; Gorodetsky, M. L. ; Kippenberg, T. J.: Temporal solitons in optical microresonators. In: *Nature Photonics* 8 (2014), Nr. 2, 145-152. http://dx.doi.org/10.1038/Nphoton.2013.343. – DOI 10.1038/Nphoton.2013.343. – ISSN 1749–4885. – Aa5tl Times Cited:1043 Cited References Count:50

[26] Benson, T. M. ; Boriskina, S. V. ; Sewell, P. ; Vukovic, A. ; Greedy, S. C. ; Nosich, A. I.: Micro-optical resonators for microlasers and integrated optoelectronics - Recent advances and future challenges. In: *Frontiers in Planar Lightwave Circuit Technology Design, Simulation, and Fabrication* 216 (2006), 39-+. <GotoISI>://WOS:000235996200002. – ISSN 1568–2609. – Bdx67 Times Cited:43 Cited References Count:178 NATO Science Series II-Mathematics Physics and Chemistry

[27] Vahala, K. J.: Optical microcavities. In: *Nature* 424 (2003), Nr. 6950, 839-846. http://dx.doi.org/10.1038/nature01939. – DOI 10.1038/nature01939. – ISSN 0028–0836. – 711hq Times Cited:4108 Cited References Count:120

[28] Debye, P.: Der Lichtdruck auf Kugeln von beliebigem Material. In: *Annalen der Physik* 335 (1909), Nr. 11, 57-136. http://dx.doi.org/https://doi.org/10.1002/andp.19093351103. – DOI https://doi.org/10.1002/andp.19093351103

[29] Rayleigh: The problem of the whispering gallery. In: *Philosophical Magazine* 20 (1910), Nr. 115-20, 1001-1004. http://dx.doi.org/Doi10.1080/14786441008636993. – DOI Doi 10.1080/14786441008636993. – ISSN 1478–6435. – V42er Times Cited:228 Cited References Count:3

[30] Rayleigh: Further applications of Bessel's functions of high order to the whispering gallery and allied problems. In: *Philosophical Magazine* 27 (1914), Nr. 157-62, 100-109. http://dx.doi.org/Doi10.1080/14786440108635067. – DOI Doi 10.1080/14786440108635067. – ISSN 1478–6435. – V42el Times Cited:63 Cited References Count:9

[31] Lefèvre-Seguin, V.: Whispering-gallery mode lasers with doped silica microspheres. In: *Optical Materials* 11 (1999), Nr. 2-3, 153-165. http://

dx.doi.org/Doi10.1016/S0925-3467(98)00041-X. – DOI Doi 10.1016/S0925–3467(98)00041–X. – ISSN 0925–3467. – 150md Times Cited:40 Cited References Count:39

[32] Armani, D. K. ; Kippenberg, T. J. ; Spillane, S. M. ; Vahala, K. J.: Ultra-high-Q toroid microcavity on a chip. In: *Nature* 421 (2003), Nr. 6926, 925-928. http://dx.doi.org/DOI10.1038/nature01371. – DOI DOI 10.1038/nature01371. – ISSN 0028–0836. – 649bk Times Cited:1678 Cited References Count:23

[33] Baba, T.: Photonic crystals and microdisk cavities based on GaInAsP-InP system. In: *Ieee Journal of Selected Topics in Quantum Electronics* 3 (1997), Nr. 3, 808-830. http://dx.doi.org/Doi10.1109/2944.640635. – DOI Doi 10.1109/2944.640635. – ISSN 1077–260x. – Ye078 Times Cited:201 Cited References Count:95

[34] Gmachl, C. ; Capasso, F. ; Narimanov, E. E. ; Nöckel, J. U. ; Stone, A. D. ; Faist, J. ; Sivco, D. L. ; Cho, A. Y.: High-power directional emission from microlasers with chaotic resonators. In: *Science* 280 (1998), Nr. 5369, 1556-1564. http://dx.doi.org/DOI10.1126/science.280.5369.1556. – DOI DOI 10.1126/science.280.5369.1556. – ISSN 0036–8075. – Zt213 Times Cited:641 Cited References Count:42

[35] Marcatili, E. A.: Bends in Optical Dielectric Guides. In: *Bell System Technical Journal* 48 (1969), Nr. 7, 2103-+. http://dx.doi.org/DOI10.1002/j.1538-7305.1969.tb01167.x. – DOI DOI 10.1002/j.1538–7305.1969.tb01167.x. – ISSN 0005–8580. – E2508 Times Cited:525 Cited References Count:17

[36] *Kapitel* 3. In: John Heebner, Tarek I. Rohit Grover G. Rohit Grover: *Optical Microresonator Theory*. New York, NY : Springer New York, 2008. – ISBN 978–0–387–73068–4, 71–103

[37] Rosenberger, A. T.: Nonlinear optical effects in the whispering-gallery modes of microspheres. In: *Operational Characteristics and Crystal Growth of Nonlinear Optical Materials* 3793 (1999), 179-186. http://dx.doi.org/Doi10.1117/12.351413. – DOI Doi 10.1117/12.351413. – ISSN 0277–786x. – Bn65z Times Cited:7 Cited References Count:47 Proceedings of SPIE

[38] Braginsky, V. B. ; Gorodetsky, M. L. ; Ilchenko, V. S.: Quality-Factor and Nonlinear Properties of Optical Whispering-Gallery Modes. In: *Physics Letters A* 137 (1989), Nr. 7-8, 393-397. http://dx.doi.org/Doi10.1016/0375-9601(89)

90912-2. – DOI Doi 10.1016/0375–9601(89)90912–2. – ISSN 0375–9601. – Aa319 Times Cited:650 Cited References Count:26

[39] Chiasera, A. ; Dumeige, Y. ; Féron, P. ; Ferrari, M. ; Jestin, Y. ; Conti, G. N. ; Pelli, S. ; Soria, S. ; Righini, G. C.: Spherical whispering-gallery-mode microresonators. In: *Laser & Photonics Reviews* 4 (2010), Nr. 3, 457-482. http://dx.doi.org/10.1002/lpor.200910016. – DOI 10.1002/lpor.200910016. – ISSN 1863–8880. – 596pr Times Cited:394 Cited References Count:153

[40] Gorodetsky, M. L. ; Savchenkov, A. A. ; Ilchenko, V. S.: Ultimate Q of optical microsphere resonators. In: *Optics Letters* 21 (1996), Nr. 7, 453-455. http://dx.doi.org/Doi10.1364/Ol.21.000453. – DOI Doi 10.1364/Ol.21.000453. – ISSN 0146–9592. – Uc298 Times Cited:828 Cited References Count:12

[41] Bogaerts, W. ; De Heyn, P. ; Van Vaerenbergh, T. ; De Vos, K. ; Selvaraja, S. K. ; Claes, T. ; Dumon, P. ; Bienstman, P. ; Van Thourhout, D. ; Baets, R.: Silicon microring resonators. In: *Laser & Photonics Reviews* 6 (2012), Nr. 1, 47-73. http://dx.doi.org/10.1002/lpor.201100017. – DOI 10.1002/lpor.201100017. – ISSN 1863–8880. – 869fl Times Cited:1637 Cited References Count:188

[42] Haus, H. A. ; Huang, W. P.: Coupled-Mode Theory. In: *Proceedings of the Ieee* 79 (1991), Nr. 10, 1505-1518. http://dx.doi.org/Doi10.1109/5.104225. – DOI Doi 10.1109/5.104225. – ISSN 0018–9219. – Gu211 Times Cited:652 Cited References Count:153

[43] Haus, Hermann A.: *Waves and fields in optoelectronics*. Englewood Cliffs, NJ : Prentice-Hall, [1984] ©1984, [1984] https://search.library.wisc.edu/catalog/999550742402121. – "The introductory graduate course 'Optics and optical electronics,' the notes of which developed into this book, was taught jointly by Professor S. Ezekiel and the author"– P. xii.;Includes bibliographical references and indexes.

[44] Spillane, S. M. ; Kippenberg, T. J. ; Painter, O. J. ; Vahala, K. J.: Ideality in a fiber-taper-coupled microresonator system for application to cavity quantum electrodynamics. In: *Physical Review Letters* 91 (2003), Nr. 4. http://dx.doi.org/ARTN04390210.1103/PhysRevLett.91.043902. – DOI ARTN 043902 10.1103/PhysRevLett.91.043902. – ISSN 0031–9007. – 704zr Times Cited:535 Cited References Count:23

[45] Yariv, A.: Universal relations for coupling of optical power between microresonators and dielectric waveguides. In: *Electronics Letters Volume 36, Issue 4, 17 February 2000*, 2004, 1-1

[46] Pfeiffer, M. H. P. ; Kordts, A. ; Brasch, V. ; Zervas, M. ; Geiselmann, M. ; Jost, J. D. ; Kippenberg, T. J.: Photonic Damascene process for integrated high-Q microresonator based nonlinear photonics. In: *Optica* 3 (2016), Nr. 1, 20-25. http://dx.doi.org/10.1364/Optica.3.000020. – DOI 10.1364/Optica.3.000020. – ISSN 2334–2536. – De7ko Times Cited:220 Cited References Count:31

[47] Pasquazi, Alessia ; Peccianti, Marco ; Razzari, Luca ; Moss, David J. ; Coen, Stéphane ; Erkintalo, Miro ; Chembo, Yanne K. ; Hansson, Tobias ; Wabnitz, Stefan ; Del'Haye, Pascal ; Xue, Xiaoxiao ; Weiner, Andrew M. ; Morandotti, Roberto: Micro-combs: A novel generation of optical sources. In: *Physics Reports* 729 (2018), 1-81. http://dx.doi.org/https://doi.org/10.1016/j.physrep.2017.08.004. – DOI https://doi.org/10.1016/j.physrep.2017.08.004. – ISSN 0370–1573. – Micro-combs: A novel generation of optical sources

[48] Agrawal, Govind P.: *Nonlinear Fiber Optics (Sixth Edition)*. Sixth Edition. Academic Press, 2019. http://dx.doi.org/https://doi.org/10.1016/B978-0-12-817042-7.00008-7. http://dx.doi.org/https://doi.org/10.1016/B978-0-12-817042-7.00008-7. – ISBN 978–0–12–817042–7

[49] Boyd, Robert W.: *Nonlinear Optics, Third Edition*. 3rd. USA : Academic Press, Inc., 2008. – ISBN 0123694701

[50] Il'chenko, V. S. ; Gorodetskii, M. L.: Thermal Nonlinear Effects in Optical Whispering Gallery Microresonators. In: *Laser Physics* 2 (1992), Nr. 6, 1004-1009. <GotoISI>://WOS:000207073800022. – ISSN 1054–660x. – V04qv Times Cited:179 Cited References Count:6

[51] Carmon, T. ; Yang, L. ; Vahala, K. J.: Dynamical thermal behavior and thermal self-stability of microcavities. In: *Optics Express* 12 (2004), Nr. 20, 4742-4750. http://dx.doi.org/Doi10.1364/Opex.12.004742. – DOI Doi 10.1364/Opex.12.004742. – ISSN 1094–4087. – 859hl Times Cited:655 Cited References Count:25

[52] Kippenberg, T. J. ; Spillane, S. M. ; Vahala, K. J.: Kerr-nonlinearity optical parametric oscillation in an ultrahigh- toroid microcavity -: art.

no. 083904. In: *Physical Review Letters* 93 (2004), Nr. 8. http://dx.doi.org/ARTN08390410.1103/PhysRevLett.93.083904. – DOI ARTN 083904 10.1103/PhysRevLett.93.083904. – ISSN 0031–9007. – 848ms Times Cited:535 Cited References Count:32

[53] Savchenkov, A. A. ; Matsko, A. B. ; Strekalov, D. ; Mohageg, M. ; Ilchenko, V. S. ; Maleki, L.: Low threshold optical oscillations in a whispering gallery mode CaF resonator -: art. no. 243905. In: *Physical Review Letters* 93 (2004), Nr. 24. http://dx.doi.org/ARTN24390510.1103/PhysRevLett.93.243905. – DOI ARTN 243905 10.1103/PhysRevLett.93.243905. – ISSN 0031–9007. – 878qh Times Cited:204 Cited References Count:12

[54] Chen, R. X. ; Shu, H. W. ; Shen, B. T. ; Chang, L. ; Xie, W. Q. ; Liao, W. C. ; Tao, Z. H. ; Bowers, J. E. ; Wang, X. J.: Breaking the temporal and frequency congestion of LiDAR by parallel chaos. In: *Nature Photonics* 17 (2023), Nr. 4, 306-+. http://dx.doi.org/10.1038/s41566-023-01158-4. – DOI 10.1038/s41566–023–01158–4. – ISSN 1749–4885. – C8ov0 Times Cited:8 Cited References Count:63

[55] Lukashchuk, A. ; Riemensberger, J. ; Tusnin, A. ; Liu, J. Q. ; Kippenberg, T. J.: Chaotic microcomb-based parallel ranging. In: *Nature Photonics* (2023). http://dx.doi.org/10.1038/s41566-023-01246-5. – DOI 10.1038/s41566–023–01246–5. – ISSN 1749–4885. – M8sf3 Times Cited:0 Cited References Count:68

[56] Shen, B. T. ; Shu, H. W. ; Xie, W. Q. ; Chen, R. X. ; Liu, Z. ; Ge, Z. F. ; Zhang, X. G. ; Wang, Y. M. ; Zhang, Y. H. ; Cheng, B. W. ; Yu, S. H. ; Chang, L. ; Wang, X. J.: Harnessing microcomb-based parallel chaos for random number generation and optical decision making. In: *Nature Communications* 14 (2023), Nr. 1. http://dx.doi.org/ARTN459010.1038/s41467-023-40152-w. – DOI ARTN 4590 10.1038/s41467–023–40152–w. – O0rz2 Times Cited:0 Cited References Count:72

[57] Hu, Y. Q. ; Bai, Q. S. ; Tang, X. ; Xiong, W. ; Wu, Y. L. ; Zhang, X. ; Xiao, Y. L. ; Du, R. C. ; Liu, L. J. ; Xia, G. Q. ; Wu, Z. M. ; Yang, J. B. ; Zhou, H. ; Wu, J. G.: Massive and parallel 10 Tbit/s physical random bit generation with chaotic microcomb. In: *Frontiers of Optoelectronics* 16 (2023), Nr. 1. http://dx.doi.org/ARTN2410.1007/s12200-023-00081-4. – DOI ARTN 24 10.1007/s12200–023–00081–4. – ISSN 2095–2759. – S8my0 Times Cited:0 Cited References Count:39

[58] N., Lorenz E.: Predictability: Does the Flap of a Butterfly's Wings in Brazil Set off a Tornado in Texas. In: *American Association for the Advancement of Science* (1972)

[59] Strogatz, Steven H.: *Nonlinear Dynamics and Chaos: With Applications to Physics, Biology, Chemistry and Engineering*. Westview Press, 2000

[60] Gleick, James: *Chaos: Making a new science*. New York : Viking, 1987. – xi, 352 p., [10] p. of plates S.

[61] Lorenz, Edward N.: Deterministic Nonperiodic Flow. In: *Journal of Atmospheric Sciences* 20 (1963), Nr. 2, 130 - 141. http://dx.doi.org/https://doi.org/10.1175/1520-0469(1963)020<0130:DNF>2.0.CO;2. – DOI https://doi.org/10.1175/1520–0469(1963)020<0130:DNF>2.0.CO;2

[62] Rössler, O.E.: An equation for continuous chaos. In: *Physics Letters A* 57 (1976), Nr. 5, 397-398. http://dx.doi.org/https://doi.org/10.1016/0375-9601(76)90101-8. – DOI https://doi.org/10.1016/0375–9601(76)90101–8. – ISSN 0375–9601

[63] Hart, Allen ; Hook, James ; Dawes, Jonathan: Embedding and Approximation Theorems for Echo State Networks. In: *Neural Networks* (2020), 05. http://dx.doi.org/10.1016/j.neunet.2020.05.013. – DOI 10.1016/j.neunet.2020.05.013

[64] Lozi, René: Can we trust in numerical computations of chaotic solutions of dynamical systems? 84 (2012), 02. http://dx.doi.org/10.1142/9789814434867_0004. – DOI 10.1142/9789814434867_0004. ISBN 978–981–4434–85–0

[65] May, Robert M.: Simple mathematical models with very complicated dynamics. In: *Nature* 261 (1976), Jun, Nr. 5560, 459-467. http://dx.doi.org/10.1038/261459a0. – DOI 10.1038/261459a0. – ISSN 1476–4687

[66] Feigenbaum, Mitchell J.: Quantitative universality for a class of nonlinear transformations. In: *Journal of Statistical Physics* 19 (1978), Jul, Nr. 1, 25-52. http://dx.doi.org/10.1007/BF01020332. – DOI 10.1007/BF01020332. – ISSN 1572–9613

[67] Pecora, L. M. ; Carroll, T. L.: Synchronization of chaotic systems. In: *Chaos* 25 (2015), Nr. 9. http://dx.doi.org/Artn09761110.1063/1.4917383. – DOI Artn 097611 10.1063/1.4917383. – ISSN 1054–1500. – Ct1nn Times Cited:187 Cited References Count:61

[68] *Kapitel* 12. In: Ohtsubo: *Chaos Synchronization in Semiconductor Lasers*. Berlin, Heidelberg : Springer Berlin Heidelberg, 2008. – ISBN 978–3–540–72650–0, 341–378

[69] Annovazzi-Lodi, Valerio ; Donati, Silvano ; Scirè, Alessandro: Synchronization of chaotic injected-laser systems and its application to optical cryptography. In: *Quantum Electronics, IEEE Journal of* 32 (1996), 07, S. 953 – 959. http://dx.doi.org/10.1109/3.502371. – DOI 10.1109/3.502371

[70] Fischer, I. ; Liu, Y. ; Davis, P.: Synchronization of chaotic semiconductor laser dynamics on subnanosecond time scales and its potential for chaos communication. In: *Physical Review A* 62 (2000), Nr. 1. http://dx.doi.org/ARTN011801DOI10.1103/PhysRevA.62.011801. – DOI ARTN 011801 DOI 10.1103/PhysRevA.62.011801. – ISSN 1050–2947. – 333qb Times Cited:297 Cited References Count:18

[71] Wang, L. S. ; Wang, J. L. ; Wu, Y. S. ; Sun, Y. H. ; Li, S. S. ; Yan, L. S. ; Wang, Y. C. ; Wang, A. B.: Chaos synchronization of semiconductor lasers over 1040-km fiber relay transmission with hybrid amplification. In: *Photonics Research* 11 (2023), Nr. 6, 953-960. http://dx.doi.org/10.1364/Prj.478487. – DOI 10.1364/Prj.478487. – ISSN 2327–9125. – K6ba0 Times Cited:5 Cited References Count:29

[72] Uchida, A. ; Matsuura, T. ; Kinugawa, S. ; Yoshimori, S.: Synchronization of chaos in microchip lasers by using incoherent feedback. In: *Physical Review E* 65 (2002), Nr. 6. http://dx.doi.org/ARTN06621210.1103/PhysRevE.65.066212. – DOI ARTN 066212 10.1103/PhysRevE.65.066212. – ISSN 1539–3755. – 2 572fm Times Cited:10 Cited References Count:54

[73] Sasaki, T. ; Kakesu, I. ; Mitsui, Y. ; Rontani, D. ; Uchida, A. ; Sunada, S. ; Yoshimura, K. ; Inubushi, M.: Common-signal-induced synchronization in photonic integrated circuits and its application to secure key distribution. In: *Optics Express* 25 (2017), Nr. 21, 26029-26044. http://dx.doi.org/10.1364/Oe.25.026029. – DOI 10.1364/Oe.25.026029. – ISSN 1094–4087. – Fj9nc Times Cited:39 Cited References Count:42

[74] Gao, H. ; Wang, A. B. ; Wang, L. S. ; Jia, Z. W. ; Guo, Y. Y. ; Gao, Z. S. ; Yan, L. S. ; Qin, Y. W. ; Wang, Y. C.: 0.75 Gbit/s high-speed classical key distribution with mode-shift keying chaos synchronization of Fabry-Perot lasers. In: *Light-Science & Applications* 10 (2021), Nr. 1. http://dx.doi.org/ARTN17210.

1038/s41377-021-00610-w. – DOI ARTN 172 10.1038/s41377–021–00610–w. – ISSN 2095–5545. – Uj0un Times Cited:38 Cited References Count:32

[75] Uchida, A. ; Liu, Y. ; Davis, P.: Characteristics of chaotic masking in synchronized semiconductor lasers. In: *Ieee Journal of Quantum Electronics* 39 (2003), Nr. 8, 963-970. http://dx.doi.org/10.1109/Jqe.2003.814366. – DOI 10.1109/Jqe.2003.814366. – ISSN 0018–9197. – 702wk Times Cited:53 Cited References Count:25

[76] Argyris, A. ; Syvridis, D. ; Larger, L. ; Annovazzi-Lodi, V. ; Colet, P. ; Fischer, I. ; Garcia-Ojalvo, J. ; Mirasso, C. R. ; Pesquera, L. ; Shore, K. A.: Chaos-based communications at high bit rates using commercial fibre-optic links. In: *Nature* 438 (2005), Nr. 7066, 343-346. http://dx.doi.org/10.1038/nature04275. – DOI 10.1038/nature04275. – ISSN 0028–0836. – 984jr Times Cited:1286 Cited References Count:24

[77] VanWiggeren, G. D. ; Roy, R.: Optical communication with chaotic waveforms. In: *Physical Review Letters* 81 (1998), Nr. 16, 3547-3550. http://dx.doi.org/DOI10.1103/PhysRevLett.81.3547. – DOI DOI 10.1103/PhysRevLett.81.3547. – ISSN 0031–9007. – 129jx Times Cited:204 Cited References Count:14

[78] Uchida, A. ; Yoshimori, S. ; Shinozuka, M. ; Ogawa, T. ; Kannari, F.: Chaotic on-off keying for secure communications. In: *Optics Letters* 26 (2001), Nr. 12, 866-868. http://dx.doi.org/Doi10.1364/Ol.26.000866. – DOI Doi 10.1364/Ol.26.000866. – ISSN 0146–9592. – 440qn Times Cited:38 Cited References Count:10

[79] Lavrov, R. ; Jacquot, M. ; Larger, L.: Nonlocal Nonlinear Electro-Optic Phase Dynamics Demonstrating 10 Gb/s Chaos Communications. In: *Ieee Journal of Quantum Electronics* 46 (2010), Nr. 10, 1430-1435. http://dx.doi.org/10.1109/Jqe.2010.2049987. – DOI 10.1109/Jqe.2010.2049987. – ISSN 0018–9197. – 668cm Times Cited:141 Cited References Count:22

[80] Ke, J. X. ; Yi, L. L. ; Xia, G. Q. ; Hu, W. S.: Chaotic optical communications over 100-km fiber transmission at 30-Gb/s bit rate. In: *Optics Letters* 43 (2018), Nr. 6, 1323-1326. http://dx.doi.org/10.1364/Ol.43.001323. – DOI 10.1364/Ol.43.001323. – ISSN 0146–9592. – Fz3kw Times Cited:121 Cited References Count:19

[81] Zhao, A. K. ; Jiang, N. ; Liu, S. Q. ; Zhang, Y. Q. ; Qiu, K.: Physical Layer Encryption for WDM Optical Communication Systems Using Private

Chaotic Phase Scrambling. In: *Journal of Lightwave Technology* 39 (2021), Nr. 8, 2288-2295. http://dx.doi.org/10.1109/Jlt.2021.3051407. – DOI 10.1109/Jlt.2021.3051407. – ISSN 0733–8724. – Rd4hw Times Cited:54 Cited References Count:29

[82] Zhang, Y. Q. ; Xu, M. F. ; Pu, M. B. ; Chen, Q. ; Zhou, M. J. ; Chen, S. C. ; Qiu, K. ; Jiang, N. ; Luo, X. G.: Experimental demonstration of an 8-Gbit/s free-space secure optical communication link using all-optical chaos modulation. In: *Optics Letters* 48 (2023), Nr. 6, 1470-1473. http://dx.doi.org/10.1364/Ol.483353. – DOI 10.1364/Ol.483353. – ISSN 0146–9592. – C2qf9 Times Cited:5 Cited References Count:24

[83] Moreno, David ; Fujii, Shun ; Nakashima, Ayata ; Uchida, Atsushi ; Sanchis, Pablo ; Tanabe, Takasumi: Synchronization of microresonator frequency combs in chaotic regime. In: Ilchenko, Vladimir S. (Hrsg.) ; Armani, Andrea M. (Hrsg.) ; Sheldakova, Julia V. (Hrsg.): *Laser Resonators, Microresonators, and Beam Control XXV* Bd. 12407 International Society for Optics and Photonics, SPIE, 2023, 1240708

[84] Moreno, David ; Fujii, Shun ; Nakashima, Ayata ; Lemcke, Deniz ; Uchida, Atsushi ; Sanchis, Pablo ; Tanabe, Takasumi: Synchronization of two chaotic microresonator frequency combs. In: *Opt. Express* 32 (2024), Jan, Nr. 2, 2460–2472. http://dx.doi.org/10.1364/OE.511097. – DOI 10.1364/OE.511097

[85] Lemcke, Deniz ; Moreno, David ; Fujii, Shun ; Nakashima, Ayata ; Uchida, Atsushi ; Tanabe, Takasumi: Assessment of the Feasibility of Employing Chaos Synchronization in Two Cascaded Microresonators for Secure Data Transmission. In: *2023 Conference on Lasers and Electro-Optics Europe & European Quantum Electronics Conference (CLEO/Europe-EQEC)*, 2023, S. 1–1

[86] Lugiato, L. A. ; Lefever, R.: Spatial Dissipative Structures in Passive Optical Systems. In: *Phys. Rev. Lett.* 58 (1987), May, 2209–2211. http://dx.doi.org/10.1103/PhysRevLett.58.2209. – DOI 10.1103/PhysRevLett.58.2209

[87] Haelterman, M. ; Trillo, S. ; Wabnitz, S.: Dissipative modulation instability in a nonlinear dispersive ring cavity. In: *Optics Communications* 91 (1992), Nr. 5, 401-407. http://dx.doi.org/https://doi.org/10.1016/0030-4018(92)90367-Z. – DOI https://doi.org/10.1016/0030–4018(92)90367–Z. – ISSN 0030–4018

[88] Scroggie, A.J ; Firth, W.J ; McDonald, G.S ; Tlidi, M ; Lefever, R ; Lugiato, L.A: Pattern formation in a passive Kerr cavity. In: *Chaos, Soli-*

tons & Fractals 4 (1994), Nr. 8, 1323-1354. http://dx.doi.org/https://doi.org/10.1016/0960-0779(94)90084-1. – DOI https://doi.org/10.1016/0960–0779(94)90084–1. – ISSN 0960–0779. – Special Issue: Nonlinear Optical Structures, Patterns, Chaos

[89] Coen, Stéphane ; Randle, Hamish G. ; Sylvestre, Thibaut ; Erkintalo, Miro: Modeling of octave-spanning Kerr frequency combs using a generalized mean-field Lugiato–Lefever model. In: *Opt. Lett.* 38 (2013), Jan, Nr. 1, 37–39. http://dx.doi.org/10.1364/OL.38.000037. – DOI 10.1364/OL.38.000037

[90] Fraser, A. M. ; Swinney, H. L.: Independent Coordinates for Strange Attractors from Mutual Information. In: *Physical Review A* 33 (1986), Nr. 2, 1134-1140. http://dx.doi.org/DOI10.1103/PhysRevA.33.1134. – DOI DOI 10.1103/PhysRevA.33.1134. – ISSN 1050–2947. – Aym18 Times Cited:3310 Cited References Count:15

[91] Kogure, Soma: *Master's thesis*. 2023

[92] Kogure, Soma ; Ohtsuka, Tamiki ; Fujii, Shun ; Kumazaki, Hajime ; Tanaka, Shuya ; Hashimoto, Yosuke ; Kobayashi, Yuta ; Araki, Tomohiro ; Furusawa, Kentaro ; Sekine, Norihiko ; Tanabe, Takasumi: FEC-free optical data transmission with a chip-integrated microresonator frequency comb source. In: *Conference on Lasers and Electro-Optics*, Optica Publishing Group, 2022, STh4K.2